

Hypersonic Phononic Crystals

by

Taras Gorishnyy

B.S. Physics

Precarpathian Vasyl Stepanyk National University, Ukraine, 2000

Submitted to the Department of Materials Science and Engineering in partial fulfillment
of the requirements for the degree of

DOCTOR OF PHILOSOPHY IN MATERIALS SCIENCE AND ENGINEERING


at the

MASSACHUSETTS INSTITUTE OF TECHNOLOGY

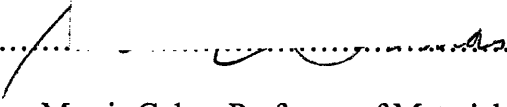
September 2007

© Massachusetts Institute of Technology 2007. All rights reserved.

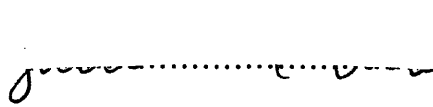
Author:

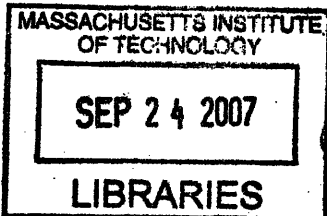

Taras Gorishnyy
Department of Materials Science and Engineering
July 5, 2007

Certified by:


Edwin L. Thomas
Morris Cohen Professor of Materials Science and Engineering
Thesis supervisor

Accepted by:


Samuel M. Allen
POSCO Professor of Physical Metallurgy
Chair of the Graduate Committee



ARCHIVES

copy 1

Hypersonic Phononic Crystals

by

Taras Gorishnyy

Submitted to the Department of Materials Science and Engineering on July 5, 2007 in partial fulfillment of the requirements for the degree of Doctor of Philosophy in Materials Science and Engineering

ABSTRACT

Manipulation of the distribution of phonons in a solid is important for both basic science and applications ranging from heat management to reduction of noise in electronic circuits and creating materials with superior acoustic and acousto-optical properties. This thesis explores hypersonic phononic crystals as means to achieve control over high frequency acoustic phonons. An integrated approach to fabrication, measurement and analysis of hypersonic phononic crystals with band gaps in the GHz range is presented. First, the phonon dispersion relation for one dimensional polymeric phononic crystals fabricated by coextrusion of a large number of poly(methylmethacrylate)/poly(carbonate) and poly(methylmethacrylate)/poly(ethylene terephthalate) bilayer pairs is investigated as a function of a lattice constant and composition using Brillouin light scattering and numerical simulations. This set of relatively simple multilayer structures represents an excellent platform to gain a basic understanding of phononic band gap phenomena. In addition, their in-plane phonon dispersion is used to extract information about the elastic constants and glass transition temperatures of individual nanolayers in a periodic multilayer arrangement. Next, two dimensional epoxy/air phononic crystals fabricated in a photoresist using interference lithography are studied. These structures are 2D single crystalline, enabling direction-resolved measurements of their phonon dispersion relation. As a result, the complete experimental phononic band diagram is obtained and correlated with numerical simulations. Finally, phononic properties of three dimensional elastomeric poly(dimethylsiloxane) crystals are investigated and the mechanical

tunability of their dispersion relation is demonstrated. This set of structures forms the basis for understanding how to design and fabricate acoustic and acousto-optical devices with performance characteristics that can be adjusted dynamically during operation. The investigations described in this thesis demonstrate both theoretically and experimentally that 1D, 2D and 3D periodic submicron structures have complex phonon dispersion relations at GHz frequencies. As a result, these crystals can be used to manipulate the flow of random thermal phonons as well as externally generated acoustic waves resulting in novel acoustic and thermal properties.

Thesis supervisor: Edwin L. Thomas

Title: Morris Cohen Professor of Materials Science and Engineering

TABLE OF CONTENTS

List of figures	7
List of tables	14
Acknowledgements	15
Chapter 1. The promise of phononic crystals	17
1.1. Introduction.....	17
1.2. What are phononic crystals?.....	18
1.3. The origin of phononic band gaps.....	19
1.4. Symmetry and phononic band gaps.....	22
1.5. Phononic crystals and sound.....	25
1.6. Ultrasonic crystals and negative diffraction.....	28
1.7. Hypersonic crystals: acousto-optics and heat management.....	30
1.8. Thesis outline.....	32
Chapter 2. Methods	34
2.1. Introduction.....	34
2.2. Elastic wave propagation in periodic media: mathematical formulation.....	34
2.3. Brillouin light scattering.....	39
2.3.1. Physics of Brillouin light scattering.....	39
2.3.2. Design and operation of a Brillouin light scattering apparatus.....	43
2.3.3. Tandem multipass Fabry-Perot interferometer and its applications in Brillouin spectroscopy.....	48
2.4. Interference lithography for fabrication of single crystalline phononic structures.....	53

Chapter 3. Phononic properties of 1D multilayer periodic self-supporting polymer films.....	58
3.1. Introduction.....	58
3.2. Normal phonon propagation in 1D phononic crystals.....	59
3.3. In-plane phonon propagation in 1D periodic anisotropic poly(methyl methacrylate)/poly(ethylene terephthalate) films.....	63
3.3.1. Phononics of giant birefringence optical polymer mirrors.....	63
3.3.2. Sample morphology.....	65
3.3.3. Experimental dispersion relation.....	66
3.3.4. FEA modeling of the phonon dispersion relation.....	70
3.3.5. Temperature dependence of sound velocities.....	76
3.3.6. Summary.....	78
3.4. Evolution of phonon dispersion of 1D periodic isotropic PC/PMMA self-supporting films with a lattice constant and composition.....	79
3.4.1. Advantages of PC/PMMA systems.....	79
3.4.2. Sample architecture and morphology.....	81
3.4.3. Experimental phonon dispersion relation of PC/PMMA films.....	83
3.4.4. Theoretical phonon dispersion relation of PC/PMMA films.....	84
3.4.5. Temperature dependence of sound velocities in PC/PMMA films.....	88
3.4.6. Summary.....	91
3.5. Conclusions.....	91
Chapter 4. Phonon dispersion relation of 2D crystals fabricated using interference lithography.....	93
4.1. Introduction.....	93
4.2. Phonon dispersion relation of 2D hexagonal crystals.....	95
4.3. Direct observation of a phononic band gap in 2D square hypersonic crystals.....	105
4.4. Conclusions.....	112

Chapter 5. Tunability of phonon dispersion relation in 3D elastomeric structures.....	114
5.1. Introduction.....	114
5.2. Fabrication process.....	114
5.3. Tunability of the phonon dispersion relation in 3D periodic PDMS elastomeric structures.....	120
5.4. Conclusions.....	124
Chapter 6. Thesis summary.....	125
Chapter 7. Directions for future investigations.....	129
Bibliography.....	133

LIST OF FIGURES

Figure 1.1. Propagation of elastic waves in a 1D phononic crystal; t_i – the thickness of i -th layer; a – the lattice constant; ρ_i , c_i and Z_i – the density, sound velocity and acoustic impedance of the i -th layer.....	20
Figure 1.2. Diamond crystal lattice – champion photonic structure, its phononic properties are currently under investigation.....	23
Figure 1.3. Kinematic sculpture by Eusebio Sempere consisting of a periodic array of hollow stainless steel cylinders, each 2.9 cm in diameter, arranged on a 10x10 cm square lattice. This sculpture has been shown to have a partial phononic band gap at 1.67 kHz along the [100] direction [1,22].....	26
Figure 1.4. Localization of sound waves on a defect in a two dimensional array of air holes in Si matrix. Color map is used to describe the variation of the normal component of the displacement field u_z for the first six eigenmodes of the crystal. This crystal can also trap light due to the presence of complete dual photonic and phononic band gaps [1,31,32].....	31
Figure 2.1. Brillouin light scattering: (a) schematic diagram of a photon-phonon scattering event, (b) momentum conservation during Brillouin light scattering.....	41
Figure 2.2. Schematic of the BLS apparatus.....	43
Figure 2.3. Symmetric scattering geometry in the transmission BLS experiments. The angle between the incident light and the normal to the sample plane is equal to the angle between the scattered light and the normal to sample plane. In this geometry the phonon	

wave vector that is probed by BLS does not depend on the refraction index of the sample.....45

Figure 2.4. The path of light inside a tandem six-pass Fabry-Perot interferometer manufactured by JRS Scientific Instruments. The figure is adapted from reference [44].....49

Figure 2.5. Transmissivity of a single set of Fabry-Perot mirrors with finesse $F = 50$, adapted from reference [44].....51

Figure 2.6. (a) Schematic diagram of the 4 beam interference lithography process, the beams have directions \vec{k}_i and polarizations \vec{E}_i given by the green and black arrows, respectively; (b) general photochemistry schemes for exposure of two different types of common photoresists; (c) SU-8 negative resist and DNQ-novolac positive resist [45]....57

Figure 3.1. Band diagrams of PC-PMMA (a) and SiO₂-PMMA (b) 1D phononic crystals with symmetric compositions; solid and dashed lines represent the longitudinal and transverse modes, respectively; red and green is used to highlight the positions of the longitudinal and transverse band gaps, respectively; their intersection displayed in dark red shows the positions of polarization independent phononic band gaps for phonons propagating normal to the layers.....61

Figure 3.2. (a) Low and (b) high magnification TEM micrographs of PMMA/PET multilayer film; the PMMA layer thickness is $t_{PMMA} = 78 \text{ nm}$ and the PET layer thickness $t_{PET} = 118 \text{ nm}$ [57]. To enhance contrast the PMMA layers were preferentially stained with ruthenium tetroxide (RuO₄).....66

Figure 3.3. Typical BLS spectra of the PMMA/PET multilayer film at two different values of the phonon wave vector k at room temperature. The numbers denote the distinct modes discussed in the text. For clarity, the central Rayleigh line is not shown. The inset

plot emphasizes the weak mode (6) by choosing a logarithmic intensity scale. The small feature G is the interferometer ghost of the strong mode (4).....67

Figure 3.4. The experimental phonon dispersion relation of the multilayer birefringent polymer film. The dashed lines are the linear fits of the five observed propagation modes (1-5) with the linear dependence between the frequency and the wave vector; the frequency of mode (6) is insensitive to k variations. The upper abscissas show the corresponding kt values for the two constituent layer thicknesses t_i69

Figure 3.5. (a): The theoretical phonon dispersion relation and the experimental data for the in-plane elastic wave propagation in the multilayer polymer film: dashed line – transverse mode (1), solid line – longitudinal mode (2), dotted lines – mixed modes (3,4), black rectangles – experimental data; (b): elastic displacement fields for modes (1-4) computed at $k = 0.01257 \text{ nm}^{-1}$ 72

Figure 3.6. The phonon dispersion relation of the PMMA/PET multilayer film for $k = 0.50 - 0.68 \text{ nm}^{-1}$: solid lines – theoretical QL modes, dashed lines – theoretical QT modes, dotted lines with circles and triangles – extrapolation of experimental data for QT modes (2,3) and QL (4-5), respectively.....75

Figure 3.7. The variation of the phase velocities of the four main modes in the PMMA/PET multilayer film as a function of temperature. The numbers correspond to the mode numbers in fig. 3.4. The vertical shaded regions denote the region of the respective glass transition temperatures of the two polymers. Solid lines represent the least square fit to the experimental data before and after the glass transition, data points in the vicinity of T_g were excluded from the fitting.....76

Figure 3.8. TEM images of the PC/PMMA films: (a), (b) and (c) – samples with $a = 782 \text{ nm}$ and 80%, 50% and 20% PC volume fraction, respectively; (d), (e) and (f) – samples with 50% PC volume fraction and 98 nm, 50 nm and 25 nm lattice constants, respectfully.....82

Figure 3.9. BLS spectra taken with the VV transmission scattering geometry at $k = 0.0181 \text{ nm}^{-1}$ for five periodic multilayer films with 50% PC volume fraction and lattice constants ranging from 25 nm to 782 nm.....83

Figure 3.10. The theoretical and experimental phonon dispersion relations of the PC/PMMA multilayer films with $a = 782 \text{ nm}$ and 20% (a), 50% (b) and 80% (c) PC volume fractions. Open and solid symbols refer to the experimental modes measured in the VH and VV BLS geometries, respectively. The theoretical dispersion relations for the QL, QT and mixed modes are plotted using solid, dashed and dotted lines, respectively.....85

Figure 3.11. Details of the displacement fields for the QT and QL modes computed for the film with $a = 782 \text{ nm}$ and 50% PC fraction at $k = 0.025 \text{ nm}^{-1}$ 87

Figure 3.12. Temperature variation of the phonon phase velocities in the PMMA/PC films with $\phi = 50\%$ and lattice constants of 782 nm (a) and 25 nm (b). The vertical shaded regions denote the regions of the respective glass transition temperatures of the two polymers. Solid lines represent the least-square the experimental data before and after the glass transition; data points in the vicinity of T_g were excluded from fitting.....90

Figure 4.1. SEM images of interference lithography patterned samples with hexagonal symmetry for (a) 4% and (b) 39% air volume fraction; (c) 90° laser light diffraction pattern confirming single crystallinity of the samples.....95

Figure 4.2. BLS spectrum of the samples at $k = 0.0051 \text{ nm}^{-1}$: (a) unpatterned epoxy film; (b) s1 pattern.....97

Figure 4.3. Experimental and selected theoretical phononic modes for s1 (top) and s2 (bottom) samples, respectively, for the phonon wave vector parallel to the [100]

direction. Solid triangles – glass mode; open triangles – Bragg mode; solid circles – phononic crystal modes; solid lines – theoretical quasilongitudinal modes; dotted lines – theoretical mixed modes.....99

Figure 4.4. The theoretical band diagrams for s1 (a) and s2 (b) samples for the phonon wave vector parallel to the $[100]$ direction. Solid lines represent quasilongitudinal modes; dashed lines – quasitransverse modes; dotted lines – mixed modes. The Brillouin zone boundary along this direction is at $\frac{2\pi}{\sqrt{3}a} = 0.00267 \text{ nm}^{-1}$ 101

Figure 4.5. Displacement fields for quasitransverse (a), quasilongitudinal (b) and mixed (c) modes computed at $k = 0.0027 \text{ nm}^{-1}$ in s1 sample. The insert shows the measurement direction.....103

Figure 4.6. SEM images of the top view (a) and the cross section (b) of the 2D crystals demonstrating their single crystallinity, very good uniformity and low defect concentration. The lattice constant is 750 nm, the hole radius is 188 nm and the film thickness is 6 nm.....106

Figure 4.7. (a) The BLS spectrum taken at $k = 0.0041 \text{ nm}^{-1}$ that corresponds to the edge of the first Brillouin zone along the $[100]$ direction ($\pi/a = 3.14/750 = 0.0041 \text{ nm}^{-1}$). Peaks (1) and (2) represent phonon modes from the first and the second propagation bands of the periodic pattern and the high intensity peak (g) comes from the longitudinal phonons of the glass substrate. To obtain frequencies of the phonon modes the experimental data were fitted with the multiple Lorentz oscillator model. The resultant fit is plotted in a solid red line, while the oscillators representing phononic crystal modes are plotted in dashed red lines. The oscillators representing elastic scattering and scattering from glass phonons are not shown. (b) The phononic dispersion relation along the $[100]$ direction showing a partial band gap between 1.21 and 1.57 GHz (in grey). Black circles

represent the phononic modes of the pattern, black diamonds – the buffer layer, black triangles – glass substrate.....109

Figure 4.8. The theoretical band diagram for a 2D square epoxy/air phononic crystal with 30% porosity for the phonon wave vector along the $[100]$ direction. QL modes are plotted with solid lines, QT modes – with dashed lines and mixed modes – with dotted lines. The partial band gap for QL phonons is highlighted in grey.....110

Figure 5.1. Schematic illustration showing the fabrication process for the 3D continuous elastomeric network/air structure. (a) Exposure by interference lithography (IL). Large arrows show the direction of the beam while small arrows show the direction of polarization of each beam. (b) 3D interference lithography template (ILT) fabricated in a positive resist. (c) 3D elastomeric network/ILT structure from the replication of the PDMS into the ILT. (d) 3D elastomeric network/air structure after flood exposure under UV lamp and subsequent removal of template in a water-based developing solution....117

Figure 5.2. Comparison of theoretical and experimental structures. (a) Isosurface of theoretical light intensity model. The inset is view normal to the $(11\bar{2}0)$ planes of the structure. (b) Calculated 3D light intensity profile interference in the (0001) plane. (c) Reconstructed confocal image showing a perspective view of the PDMS elastomeric structure. The inset is the view of y-z cross-sectional plane of the structure corresponding to the schematic views in the inset of (a). (d) SEM image of ILT pattern fabricated in a positive photoresist (AZ5214-E)) with a lattice spacing of 980 nm. (e) SEM image of 3D templated PDMS network/air structure having the complementary structure to (d).....119

Figure 5.3. BLS spectra of PDMS elastomeric structures at $k = 0.00139 \text{ nm}^{-1}$ with 0% (a) and 30% tensile strain (b) along the $[10\bar{1}0]$ direction. Peaks (1) and (3) derive from the phonons propagating in the phononic crystal and are shifted by the deformation. Peak (2) arises from the longitudinal phonons of the unpatterned PDMS substrate and remains

unchanged. Peak (4) is a result of backscattered light. The phonon wave vector is oriented along the $[10\bar{1}0]$ direction. AFM images with 0% (c) and 30% tensile strain (d) along the same direction clearly show the change in the lattice parameter and symmetry upon deformation. Insets are FFT of the AFM images.....121

Figure 5.4. The phonon dispersion relation of the 3D PMDS/air structures measured along the $[10\bar{1}0]$ direction. Red dots – phonon modes of the undeformed pattern, blue dots – phonon modes of the strained pattern (30% along the $[10\bar{1}0]$ direction), black dots – substrate contribution.....123

LIST OF TABLES

Table 3.1. Mechanical properties and glass transition temperatures of PC, PMMA and SiO ₂	60
Table 3.2. Sound velocities and their temperature coefficients α_T of the various phonon modes of the PET/PMMA multilayer film.....	78
Table 3.3. Structural parameters of PC/PMMA multilayer films.....	81

ACKNOWLEDGEMENTS

Getting a Ph.D. was a long journey of discovery, excitement, sometimes frustration, and most importantly learning to understand myself and the world around me. I met many great people along the way, and they helped me and changed me tremendously. I am very grateful to my advisor, Prof. Edwin L. (Ned) Thomas, for endowing me with his support, inspiration and freedom to pursue my research interests. For me, Ned has become the example of an exceptional scientist with deep passion for learning and discovery, and a great mentor, who is able to transfer his passion and his knowledge to his students. I thank Profs. John Joannopoulos, Keith Nelson, Yoel Fink and Silvija Gradecak for serving on my Ph.D. committee and providing me with valuable feedback and suggestions. It was a pleasure to work with Prof. George Fytas from the Max Planck Institute for Polymers Research in Mainz, Germany, who introduced me to the field of Brillouin light scattering and performed some of the BLS measurements described in this thesis. Dr. John R. Sandercock, the owner of the JRS Scientific Instruments in Zwillikon, Switzerland taught me everything I know about tandem Fabry-Perot interferometers. I thank my colleagues, Dr. Ji-Hyun Jang and Dr. Chaitanya K. Ullal, Dr. Steve Kooi and Henry Koh for their help with fabrication of hypersonic phononic structures using interference and phase mask lithography, and to Dr. Martin Maldovan for developing the FEA code that was used to compute the band structure of 2D periodic hexagonal phononic crystals.

I was fortunate to have many great friends, who made my life at MIT so much more enjoyable. I will always remember dinner parties with Hong Linh Ho Duc and Nu Bui,

fishing trips with Simon Bellemare, Julie Vigneault, Bruce Wu and Jorge Vieyra, lab conversations with Joe Walish, Rafal A. Mickiewicz, Nich Tsui, Rachel Pitel, Taeyi Choi, Ozge Akbulut and Aise Asatekin, dinner-time chats with my roommates Fabien Sorin, Yall Le Tallec, Tilke Judd, Laetitia Fournier, Matthieu and Marina Vandamme, Beth Whitwell and Ben Ginsberg and taekwondo tournaments with Rene Chen.

Prof. Samir Aouadi from the Southern Illinois University at Carbondale has been a great friend and mentor, who convinced me to come for a graduate school to the USA. I am grateful to Profs. Suzanne Rohde and Eveline Baesu from the University of Nebraska-Lincoln for their advice and support during my time in Nebraska and Profs. Bogdan Ostafiychuk, Dmytro Freik, Mark Ruvinskiy, Ivan Klymyshyn, Yaroslav Saliy and Volodymyr Klanichka from the Precarpathian National University in Ukraine for teaching me the foundations of modern physics.

I am greatly indebted to Allan and Sandy Fedoruk, who were always there to help. I had some of my best Christmas holidays in their house in Texas.

I was very fortunate to meet Amy Chi. She made my life brighter and I thank her for that.

Most of all, I am grateful to my family. They made me who I am with their unconditional love and constant support and I dedicate this thesis to them.

CHAPTER 1. THE PROMISE OF PHONONIC CRYSTALS [1]

1.1 Introduction

Phononic crystals are periodic materials that have potential to control the propagation of elastic and acoustic waves. Interest in this class of materials has been generated by the recent investigations of very similar *photonic* crystals, which resulted in the discovery of a wide range of novel and exciting optical phenomena, such as slowing and localization of light, negative refraction, etc., and may lead to many applications in telecommunications, imaging and optical computing. The field of *phononic* crystals is just emerging, and at this stage it is important to identify the most fundamental concepts and rules that govern the behavior of these materials, as well as to hypothesize about their potential applications.

This chapter focuses on the basic physics and applications of phononic crystals. The concept of a phononic band gap is defined and its relation to the crystal symmetry and its mechanical properties is investigated. The technological promise and the requirements for fabrication and characterization of phononic crystals are reviewed for sonic, ultrasonic and hypersonic frequencies, and the similarities and differences between phononic crystals operating in different frequency regimes are highlighted. Finally, in the last section of this chapter a brief overview of the thesis content is provided.

1.2 What are phononic crystals?

My interest in phononic crystals was sparked by the realization that they can notably influence the random, thermally induced motions of atoms – something I had never thought possible. Thermal atomic vibrations appear random and chaotic, they are perhaps the most powerful illustration of the concept of entropy, and the idea to extend any kind of influence over them seemed very strange and foreign to me. Yet, atoms in solids are connected by chemical bonds and cannot move independently. When an atom is displaced from its equilibrium position, it exerts force on its neighbors, which causes them to move. These atoms, in turn, cause their neighbors to move and the end result is the creation of a phonon – a wave of lattice distortion that propagates through the solid. But if thermal atomic motions can be treated as waves, then in addition to the laws of thermodynamics they must obey the laws of wave mechanics, in particular the laws of interference and diffraction. It is precisely this wave-like nature of atomic motions that phononic crystals utilize to forbid propagation of certain phonons and redistribute their energy. As a result, hypersonic phononic crystals can modify thermal conductivity of materials, which is very important for a whole range of applications, particularly for improving efficiency of thermo-electric energy conversion [2,3].

This example illustrates how phononic crystals combine novel and interesting science with a promise for technological innovations. From the scientific point of view, physics of phononic band gap materials is very rich. Mechanical waves can be both longitudinal and transverse, in contrast to electromagnetic waves, which are always transverse, and electron waves, which are scalar. Furthermore, there is a significant difference between

elastic displacement waves propagating in solids, which can have both longitudinal and transverse components of displacement, and acoustic pressure waves propagating in fluids, which are always longitudinal. Finally, phonons strongly interact with each other, especially at high frequencies. Thus, to gain a correct understanding of phonon-mediated phenomena it is important to consider their mean free path, in addition to their wavelength and the structural length scale. As a result, *phononic* band gap phenomena depend on a larger number of parameters and are significantly more complex than more widely studied *photonic* band gap phenomena.

A technological perspective is also important. It is useful to divide phononic crystals into three classes – sonic, ultrasonic and hypersonic crystals – based on their frequency of operation. Each of these classes leads to entirely different applications and requires completely different technical approaches. Sonic crystals (1 Hz – 20 kHz) are important for sound manipulation and communications; ultrasonic crystals (20 kHz – 1 GHz) play a role in imaging and non-destructive testing; while hypersonic crystals (>1 GHz) may lead to new applications in acousto-optics, signal processing and thermo-electricity. Each of these classes of phononic crystals is treated in more detail later in this chapter.

1.3 The origin of phononic band gaps

To better understand the origin of phononic band gaps, consider an elastic wave propagating in a 1D crystal composed of alternating layers of two different materials. At every interface the incoming wave transfers part of its energy into secondary, reflected waves, which then interfere with each other. If this interference is constructive and there

is a sufficient number of these interfaces, eventually all energy of the original wave is reflected back and the wave cannot propagate through the crystal. On the other hand, if the interference is destructive, then all energy of the original wave is transmitted through the crystal. Therefore, constructive interference of the secondary waves results in the creation of band gaps, while destructive interference leads to the formation of propagation bands.

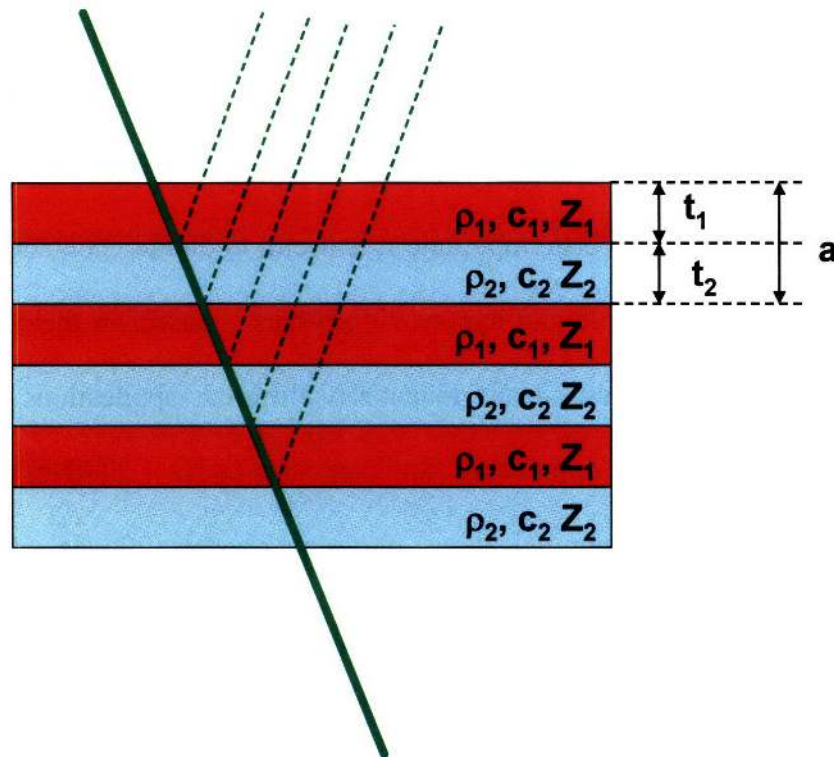


Figure 1.1. Propagation of elastic waves in a 1D phononic crystal; t_i – the thickness of i -th layer; a – the lattice constant; ρ_i, c_i and Z_i – the density, sound velocity and acoustic impedance of the i -th layer.

The condition for constructive interference is simply that the path differences between the interfering waves must be equal to an integer multiple of their wavelength, λ . Since the path difference is determined by the lattice parameter of the crystal a , it is easy to see that the interference occurs when the lattice parameter is comparable to the wavelength $a \sim \lambda$. Since frequency is inversely proportional to wavelength, the frequency at the

center of the band gap ω_g , is also inversely proportional to the lattice parameter,

$\omega_g \sim \frac{1}{\lambda} \sim \frac{1}{a}$. As a result, one can create a band gap at any frequency or wavelength by

changing the size of a unit cell. The reflectivity of each interface is given by the equation:

$$R = \left(\frac{Z_2 - Z_1}{Z_2 + Z_1} \right)^2 \quad (1.1)$$

Here Z_i is the acoustic impedance of the i -th material, which is equal to the product of its density and sound velocity (longitudinal or transverse, depending on the polarization of the incident wave), $Z_i = c_i \cdot \rho_i$. The width of the band gap is generally proportional to the interface reflectivity. Therefore, to increase the band gap one needs to use materials with a large acoustic impedance mismatch.

Moreover, the position and width of the band gap depends on the propagation direction because the path difference depends on the angle of incidence. Some phononic crystals form band gaps for waves propagating in any direction – these are known as *absolute* or *complete* band gaps. Other materials possess *partial* band gaps that only stop waves of certain frequencies traveling in certain directions. It is easy to see that a 1D crystal does not have an absolute band gap because its mechanical properties only vary in one direction: waves traveling at right angles to this direction will not be reflected (instead they can be effectively guided in each layer), so there will not be a band gap in this direction.

1.4 Symmetry and phononic band gaps

How does one design a phononic crystal to have a complete band gap? It is clear from the previous 1D example that the density and sound velocities need to vary in all three directions of space. However, not all 3D periodic structures will form a complete phononic band gap. In fact, it is still quite difficult to determine the structures that possess large absolute phononic band gaps.

For electromagnetic waves, which only have two transverse components of the dielectric displacement vector, it is known that sinusoidal modulations of the dielectric contrast along certain directions create photonic crystals with absolute gaps for three different highly symmetric lattices: simple cubic, body-centered-cubic and face-centered-cubic [4]. The face-centered-cubic lattice having a diamond network possesses the current champion photonic band gap, i.e. the largest band gap for a given dielectric contrast.

In solids mechanical waves can have both longitudinal (tension/compression) and transverse (shear) components, although only longitudinal waves are allowed in fluids. As a result, if we want to create a complete phononic band gap, we must design structures with band gaps for both longitudinal and transverse waves in the same frequency region and in general this is harder to do in phononic crystals with three modes than in photonic crystals with only two transverse modes.

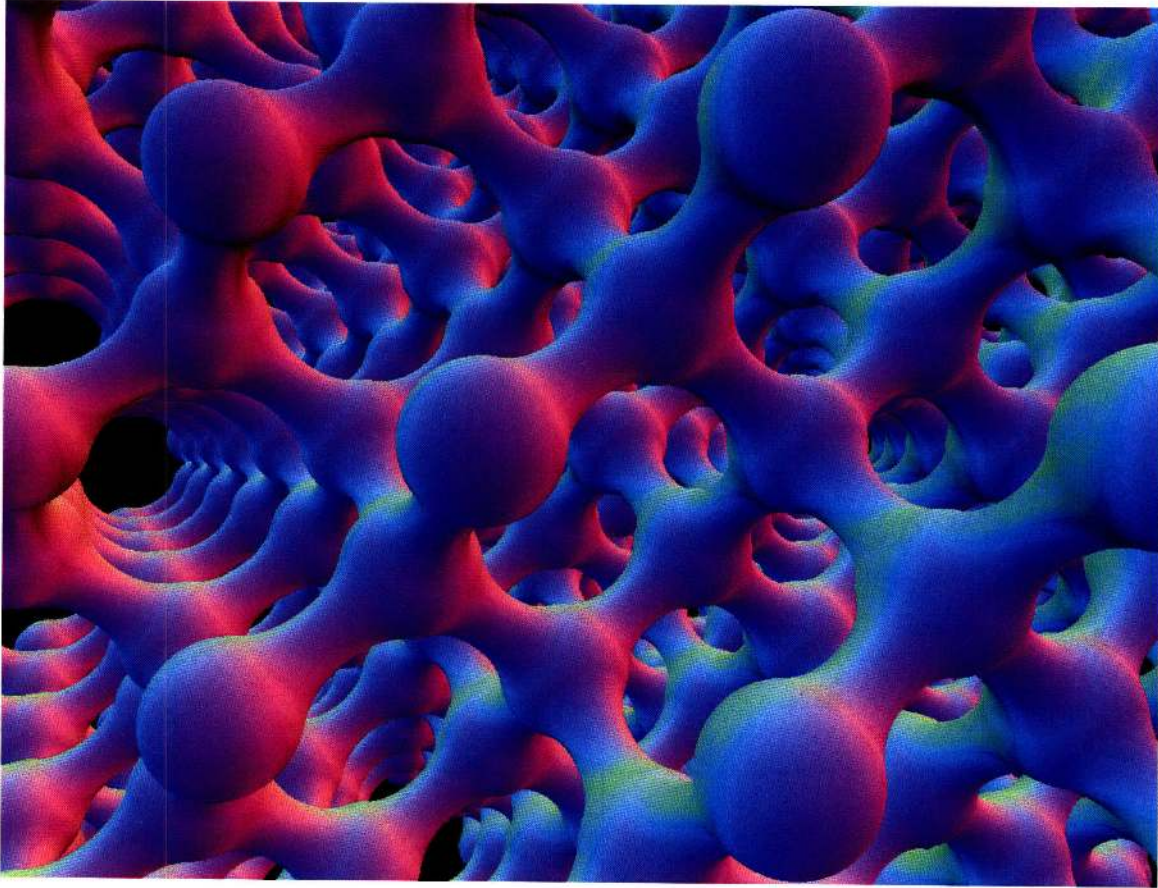


Figure 1.2. Diamond crystal lattice – champion photonic structure; its phononic properties are currently under investigation [1].

The problem of elastic wave propagation in 1D periodic layered composites was first treated by Brillouin in 1946 [5], and then further developed by several other authors [6-8]. Yet, it was the recent advances in the field of photonic crystals that drew renewed interest to phononic band gap materials. The search for structures with complete phononic band gaps was started by theoretical work by M. M. Sigalas and E. N. Economou in 1992. They showed that solid-solid and fluid-fluid structures that consisted of a periodic 3D lattice of identical high-density spheres placed within a low density host material gave rise to complete phononic band gaps [9].

Despite the fact that elastic waves propagate at two different speeds within solids, while acoustic waves travel at a single speed in fluids, Sigalas and Economou predicted that complete phononic band gaps should exist in both cases. A few months later they showed that an infinite 2D square array of high-density parallel cylinders embedded in a low-density host material should also possess a complete band gap for both solid/solid and fluid/fluid systems in 2D [10]. Unaware of this work, M. Kushwaha *et al.* reported the existence of partial phononic band gaps for transverse elastic waves propagating in 2D solid/solid crystals with the displacement fields polarized in the crystal plane in 1993 [11].

Despite a relatively large number of theoretical investigations that followed these early pioneering studies [12-21], it is difficult to yet clearly identify the “champion” phononic structure, i.e. the structure with the largest phononic band gap for a given contrast in materials properties. Unlike the photonic case, where for a given structure the size of the band gap depends only on the refractive index contrast n_1/n_2 ; in the phononic case one must consider the density ratio ρ_1/ρ_2 , the velocity contrast between components c_{L1}/c_{L2} and c_{T1}/c_{T2} , and the longitudinal vs. transverse velocity ratio for each material component c_{L1}/c_{T1} and c_{L2}/c_{T2} . Moreover, as was mentioned before, the behavior of solid-solid periodic media is considerably different from that of solid-fluid media, which is in turn different from that of fluid-fluid media. For this reason, it is challenging not only to identify the champion phononic structure, but even to perform comparison of the results for different material systems. It is not surprising then, that no general approach to phonon dispersion engineering has yet been proposed. Currently, the largest complete

band gaps in 3D were reported for arrays of spherical inclusions of a low density fluid ($\rho=1.07 \text{ g/cm}^3$) in a high density fluid host ($\rho=13.6 \text{ g/m}^3$) arranged on fcc, bcc and sc lattices (which would be impossible to realize experimentally) [15] ($\xi = \frac{\Delta\omega}{\omega_{midgap}} = 0.83, 0.77$ and 0.62 for fcc, bcc and sc lattices, respectively). In 2D, the largest band gaps with $\xi = 1.8$ were found for rectangular and hexagonal arrays of air cylinders in water [16].

1.5 Phononic crystals and sound

Sound manipulation is perhaps the most obvious application of phononic crystals. Sound is immensely valuable in our daily lives for communications, information transfer or simply for its aesthetic value as exhibited in music and rhythms. For human hearing sound is made up of mechanical waves with frequencies roughly between 20 Hz and 20 kHz, or wavelengths ranging from meters to several tens of centimeters. Therefore, if we assemble periodic structures with lattice constants in this range, we can expect them to interact with sound and act as sonic mirrors.

A great illustration of sonic properties of a periodic structure was provided by Francisco Meseguer and co-workers at the Materials Science Institute of Madrid in 1995 when they studied the acoustic characteristics of a kinematic sculpture made earlier by Eusebio Sempere, see fig 1.3 [1,22]. This minimalist sculpture consists of periodic square array of hollow steel cylinders of 2.9 cm in diameter with a lattice constant of 10 cm.



Figure 1.3. Kinematic sculpture by Eusebio Sempere consisting of a periodic array of hollow stainless steel cylinders, each 2.9 cm in diameter, arranged on a 10x10 cm square lattice. This sculpture has been shown to have a partial phononic band gap at 1.67 kHz along the [100] direction [1,22].

In addition to being visually appealing, Meseguer and co-workers recognized that the sculpture should also possess a sonic band gap, so they measured the acoustic transmission of the sculpture as a function of frequency and direction. They found that sound traveling normal to the cylinders axes along the [100] direction was strongly attenuated at a frequency of 1670 Hz – a result that provided the first experimental evidence for the existence of phononic band gaps in periodic structures.

It is easy to estimate the relation between the lattice constant and the band gap frequency. The gap usually opens between the first and the second propagation bands at the edge of the first Brillouin zone. Assuming that the sound velocity remains independent on the wave vector (this assumption ignores the bending of the propagation bands, but nevertheless is accurate enough for an order of magnitude estimation of the midgap frequency) the midgap frequency is roughly equal to

$$f = \frac{c}{\lambda} = \frac{c \cdot k}{2\pi} = \frac{c}{2a} \quad (1.2)$$

for the propagation along the [100] direction in a square lattice, where the edge of the first Brillouin zone is located at $k = \frac{\pi}{a}$. Substituting in the lattice constant of the kinematic sculpture and sound velocity of air we obtain $f = 1720$ Hz, which is very close to the observed experimental value.

The previous example shows that a structure needs to be several meters wide to create a phononic band gap in the sonic regime. While this might not be a problem for architectural acoustics, it is impractical for many other devices such as headphones and speakers. One way to deal with this problem was proposed by Z. Liu *et al.* [23], who used an array of locally resonant composite materials (lead balls coated with silicone rubber) to achieve strong attenuation for the wavelengths two orders of magnitude larger than the crystal lattice constant. Unlike regular phononic crystals, locally resonant materials attenuate acoustic waves traveling at or near resonant frequencies by transferring their energy into localized eigenvibrations of the objects that make up the lattice, which allows tuning the band gap frequency by modifying eigenfrequencies of the objects as opposed

to changing the lattice constant. This approach is not limited to sonic crystals and can be used to create structures with phononic band gaps at ultrasonic and hypersonic frequencies, as long as locally resonant structures with the resonances at these frequencies are available.

1.6 Ultrasonic crystals and negative refraction

Ultrasonic crystals have much smaller lattice constants ($10^{-2} - 10^{-5}$ m) and operate at significantly higher frequencies (20 kHz – 100 MHz). The technological potential of ultrasonic crystals lies in their ability to improve performance and resolution of current ultrasonic imaging and medical diagnostics systems by providing superior acoustic mirrors and, especially, negative refraction based acoustic superlenses. Ultrasonic technology is well established already; it offers a wide variety of acoustic sources, detectors and good understanding of the scientific foundations behind ultrasound propagation and the associated imaging process. Its main shortcoming lies in its limited ability to focus, reflect or otherwise influence propagation of acoustic beams. Ultrasonic phononic crystals directly address this issue and can be readily integrated into current imaging systems. Moreover, ultrasonic crystals are macroscopic objects (lattice constant in *mm* or sub *mm* range) and they can be easily fabricated at large scale with modern manufacturing methods. In particular, 3D printing can be used to manufacture any 3D periodic single crystalline structures with lattice constants down to 0.1 mm.

The possibility of making superlenses with sub wavelength resolution has been one of the hottest topics in optics for last several years. Photonic crystals with negative refraction

have been suggested theoretically and demonstrated experimentally as means to create optical superlenses for the visible range [24-26]. Similarly phononic crystals can be used to achieve negative refraction of acoustic waves and create acoustic superlenses [27-30].

To get an intuitive understanding of negative refraction consider a sound wave moving from a homogeneous medium into a phononic crystal at an angle different from 90 degrees. We can think of the sound wave as consisting of two components: one that travels parallel to the surface, and one that moves at right angles to it. Negative refraction will occur if the direction of the parallel component upon entering the crystal is reversed, while that of the normal wave does not change. This is actually possible if the parallel component is reflected by the phononic crystal, while the normal wave component is allowed to propagate. More precise mathematical requirements for negative refraction in phononic crystals have been formulated and discussed by X. Zhang *et al.* [27]. Finally, negative refraction and ultrasound focusing by flat superlenses has been experimentally observed in arrays of 0.8 mm in diameter tungsten carbide beads manually arranged on an fcc lattice in water [28].

1.7 Hypersonic crystals: acousto-optics and heat management

Hypersonic phononic crystals operate at frequencies of 100 MHz or higher and have lattice constants in submicron range. They can also be used for a high resolution acoustic imaging. In fact, acoustic microscopes operating at up to 5 GHz have recently become commercially available (these microscopes currently do not use phononic crystals in their imaging optics). However, significant difficulties in generating very high frequency acoustic waves as well as relatively short mean free path for hypersonic phonons in many materials limit performance of such imaging systems. On the other hand, hypersonic crystals may find very interesting applications in acousto-optics and heat management.

Since hypersonic crystals have lattice constants in the range of wavelengths of visible or infrared light, it is interesting to explore the possibility of creating materials with simultaneous photonic and phononic band gaps. Recently the existence of such materials has been demonstrated theoretically for the case of 2D crystals consisting of rectangular and hexagonal arrays of air holes in silicon with the filling ratio of 0.45 [31]. The unique advantage of photonic-phononic dual band gap materials comes from their ability to localize both sound and light in the same special regions (defects) [32], see fig. 1.4. This leads to dramatic increase in the intensity of acousto-optical interactions. In fact, in 2002 M. Trigo and co-workers measured photon-phonon scattering in 1D periodic structures that contained both partial photonic and phononic band gaps. They observed that such double localization of photons and phonons increases the efficiency of photon-phonon scattering by five orders of magnitude compared with the values for similar 1D structures with photonic cavities only [33]. Materials with enhanced acousto-optical interactions are

being currently explored for many novel applications. For example, P. A. Fokker *et al.* suggested that it might be possible to use these structures to generate intense sources of coherent monochromatic phonons, i.e. *phonon* lasers [34]. Other applications may include optical cooling [35], THz energy conversion via acoustoluminescence mechanism [36] and increasing efficiency of light emission in silicon [37].

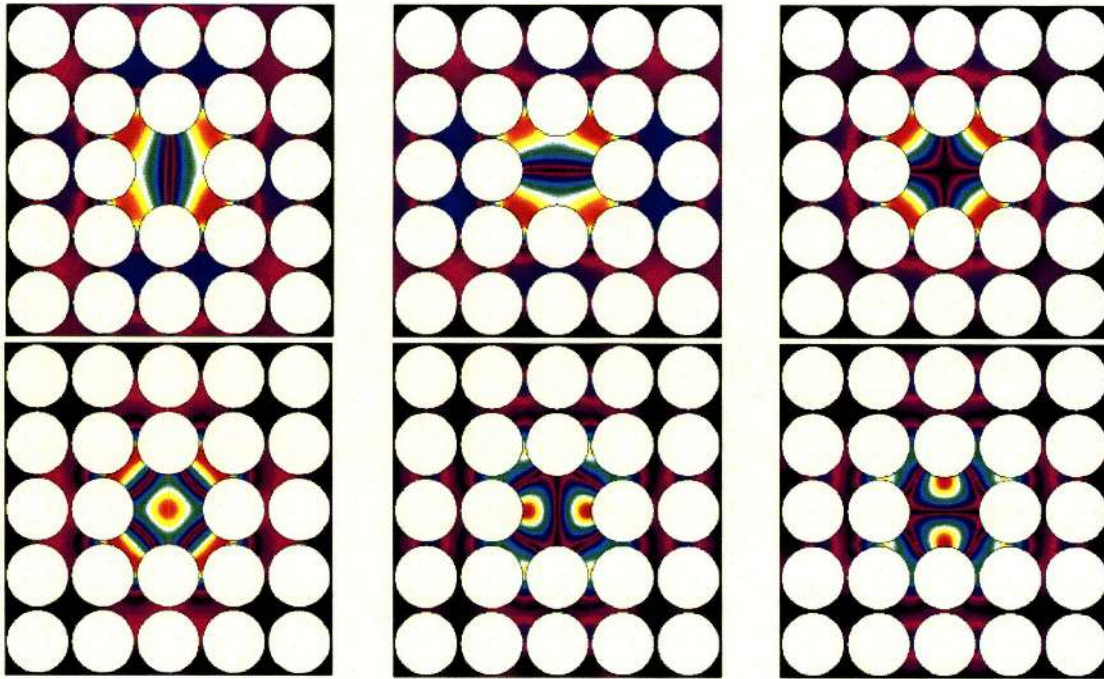


Figure 1.4. Localization of sound waves on a defect in a two dimensional array of air holes in Si matrix. Color map is used to describe the variation of the normal component of the displacement field u_z for the first six eigenmodes of the crystal. This crystal can also trap light due to the presence of complete dual photonic and phononic band gaps [1,31,32].

Hypersonic phononic crystals could also have a large impact in thermal management. Thermal energy in solids is transported primarily by electrons and phonons. The electronic contribution is important for materials with a large number of free carriers, such as metals. On the other hand, the thermal conductivity of dielectric materials and many semiconductors is determined mainly by the phonons. The presence of a phononic band gap at frequencies that corresponds to the dominant frequencies of thermal

vibrations can greatly reduce the flow of phonons and therefore the thermal conductivity of a solid.

This could prove very useful for thermoelectric devices that convert thermal energy directly into electricity. The figure of merit for a thermoelectric device, ZT , scales as

$$ZT \sim \frac{\sigma}{k_e + k_{ph}}, \quad (1.3)$$

where σ is the electrical conductivity, and k_e and k_{ph} are the electronic and phononic heat conductivities. If we reduce the electronic heat conductivity, k_e , we will also reduce the electrical conductivity, σ , which means that ZT will not increase. However, by using a phononic band gap to reduce the phononic heat conductivity, k_{ph} , it could be possible to greatly improve the performance of devices such as Peltier thermoelectric coolers, thermocouples and thermoelectric energy generators [2,3].

1.8 Thesis outline

This thesis presents an integral approach to fabrication, characterization and analysis of submicron periodic structures with phononic band gaps at hypersonic frequencies. The description of the experimental and numerical methods, which were employed to study properties of hypersonic phononic crystals, is provided in chapter 2. In particular, the main principles behind the design and operation of a Brillouin light scattering apparatus are discussed in great detail, since Brillouin light scattering is the central tool used to extract experimental information about the phonon dispersion relation of periodic submicron materials. Chapter 3 reports on the phononic properties of 1D periodic multilayer polymer films fabricated by multilayer coextrusion. Knowledge of the phonon

dispersion relations of these relatively simple periodic structures is important to understand the basic physics of phononic band gaps materials. In addition, it provides valuable information about mechanical and thermodynamic properties of polymer nanolayers in a sandwiched multilayer assembly.

Phononic properties of 2D periodic crystals with square and hexagonal lattice symmetry are treated in chapter 4. These structures possess complex multimode dispersion relations, which consist of the multiple propagation bands separated by the band gaps. The partial phononic band gap between the first and the second propagation band of quasi longitudinal phonons is observed experimentally in the 2D square crystals. Finite element analysis was used to compute the theoretical dispersion relations and the details of the displacement fields of various modes in these structures. The modeling results are in very good agreement with the experimental data using no adjustable parameters.

3D periodic elastomeric crystals with the phonon dispersion relation that can be tuned by the application of mechanical strain are described in chapter 5. These structures can be used to create various acoustic and acousto-optical devices with the performance characteristics that can be dynamically adjusted during the operation. In addition, they form a very interesting platform to study experimentally the influence of lattice symmetry of the phononic band diagram. Finally, the main conclusions of this study are summarized in chapter 6 and many promising directions for the future investigations are listed in chapter 7.

CHAPTER 2. METHODS

2.1 Introduction

This chapter provides a brief overview of various techniques and methods used in this investigation. It contains three main sections: section 2.2 that describes the mathematics of elastic wave propagation in periodic structures; section 2.3 that treats the physics of Brillouin light scattering and develops a practical design of a Brillouin light scattering apparatus, which is used as the main characterization tool to measure phonon dispersion relation of periodic materials; and section 2.4 that outlines fundamentals of interference lithography and its applications towards fabrication of single crystalline periodic solid/air submicron structures. A sufficient amount of detail is provided to achieve a solid understanding of these techniques and their use in phononics, while additional information is available in the references mentioned in the text and listed at the end of this thesis.

2.2 Elastic wave propagation in periodic media: mathematical formulation

The equations of motion for an elastic medium are [38,39]

$$\rho \frac{\partial^2 u_i}{\partial t^2} = \frac{\partial \sigma_{ij}}{\partial x_j}. \quad (2.1)$$

Here, ρ is the density of the material, $u_i = u_i(x, t)$ is the i -th component of the displacement vector at point x and time t , and $\sigma_{ij} = \sigma_{ij}(x, t)$ are the components of the stress tensor. Summation over the repeatable indices is assumed. The material-dependent stress-displacement constitutive relations $\sigma_{ij} = f(u_i)$ allow eliminating stress in the

motion equations and describing the wave propagation in terms of displacement only. For a general anisotropic medium the constitutive relations are

$$\sigma_{ij} = C_{ijmn} u_{mn}, \quad (2.2)$$

where C_{ijmn} is the stiffness tensor of the medium and $u_{ij} = \frac{1}{2} \left(\frac{\partial u_i}{\partial x_j} + \frac{\partial u_j}{\partial x_i} \right)$ is the strain tensor of the medium. The number of independent components in the stiffness tensor is determined by the material symmetry. There are 21 independent elastic constants for general anisotropic materials, 9 for orthotropic materials, 5 for transverse isotropic materials and 2 for isotropic materials. Elastic stiffness matrixes for orthotropic, transverse orthotropic and isotropic materials are listed below.

$$C_{orthotropic} = \begin{pmatrix} C_{11} & C_{12} & C_{13} & 0 & 0 & 0 \\ C_{12} & C_{22} & C_{23} & 0 & 0 & 0 \\ C_{13} & C_{23} & C_{33} & 0 & 0 & 0 \\ 0 & 0 & 0 & C_{44} & 0 & 0 \\ 0 & 0 & 0 & 0 & C_{55} & 0 \\ 0 & 0 & 0 & 0 & 0 & C_{66} \end{pmatrix} \quad (2.3)$$

$$C_{trans_isotropic} = \begin{pmatrix} C_{11} & C_{12} & C_{13} & 0 & 0 & 0 \\ C_{12} & C_{11} & C_{13} & 0 & 0 & 0 \\ C_{13} & C_{13} & C_{33} & 0 & 0 & 0 \\ 0 & 0 & 0 & C_{44} & 0 & 0 \\ 0 & 0 & 0 & 0 & C_{44} & 0 \\ 0 & 0 & 0 & 0 & 0 & (C_{11} - C_{12})/2 \end{pmatrix} \quad (2.4)$$

$$C_{isotropic} = \begin{pmatrix} C_{11} & C_{12} & C_{12} & 0 & 0 & 0 \\ C_{12} & C_{11} & C_{12} & 0 & 0 & 0 \\ C_{12} & C_{12} & C_{11} & 0 & 0 & 0 \\ 0 & 0 & 0 & (C_{11} - C_{12})/2 & 0 & 0 \\ 0 & 0 & 0 & 0 & (C_{11} - C_{12})/2 & 0 \\ 0 & 0 & 0 & 0 & 0 & (C_{11} - C_{12})/2 \end{pmatrix} \quad (2.5)$$

The wave equations for an infinite anisotropic elastic medium can be further simplified by looking for a plane wave solution

$$\vec{u} = \vec{u}_0 \exp(i(\vec{k} \cdot \vec{r} - \omega \cdot t)), \quad (2.6)$$

substituting it into the system of the original partial differential equations (2.2) and performing differentiation. We then obtain an eigenvalue matrix equation

$$DCD^T \cdot \vec{u} = \rho \left(\frac{\omega}{|\vec{k}|} \right) \cdot \vec{u}, \quad (2.7)$$

known as Christoffel equation, where

$$D = \frac{1}{|\vec{k}|} \begin{pmatrix} k_x & 0 & 0 & 0 & k_z & k_y \\ 0 & k_y & 0 & k_z & 0 & k_x \\ 0 & 0 & k_z & k_y & k_x & 0 \end{pmatrix}. \quad (2.8)$$

This equation has a nontrivial solution if

$$\det \left(DCD^T - \rho \left(\frac{\omega}{|\vec{k}|} \right) E \right) = 0. \quad (2.9)$$

This expression allows calculation of the phonon dispersion relation for a plane wave propagating in an anisotropic homogeneous medium along any direction defined by the direction of its wave vector \vec{k} .

For isotropic materials, the constitutive relations become simpler,

$$\sigma_{ij} = \lambda u_{kk} \delta_{ij} + 2\mu u_{ij}. \quad (2.10)$$

Here λ and μ are the Lamé coefficients of the material [12,38]. Then, the motion equations can be written as

$$\frac{\partial^2 u_i}{\partial t^2} = \frac{1}{\rho} \left\{ \frac{\partial}{\partial x_i} \left(\lambda \frac{\partial u_l}{\partial x_l} \right) + \frac{\partial}{\partial x_i} \left[\mu \left(\frac{\partial u_i}{\partial x_i} + \frac{\partial u_l}{\partial x_l} \right) \right] \right\}. \quad (2.11)$$

These equations are further simplified by introducing two fields, scalar $\phi = \phi(x, t)$ and vector $\vec{H} = \vec{H}(x, t)$, called the displacement potentials, through the relations

$$\vec{u} = \nabla \phi + \nabla \times \vec{H}, \quad \nabla \cdot \vec{H} = 0. \quad (2.12)$$

Then, in case of a homogeneous medium, the motion equations become

$$\frac{\partial^2 \phi}{\partial t^2} = \frac{\lambda + 2\mu}{\rho} \nabla^2 \phi, \quad \text{and} \quad \frac{\partial^2 \vec{H}}{\partial t^2} = \frac{\mu}{\rho} \nabla^2 \vec{H}. \quad (2.13)$$

The first equation describes longitudinal compression waves propagating in the medium with a velocity

$$c_L = \sqrt{\frac{\lambda + 2\mu}{\rho}}, \quad (2.14)$$

while the second one describes transverse shear waves propagating with a velocity

$$c_T = \sqrt{\frac{\mu}{\rho}}. \quad (2.15)$$

Since these two equations are uncoupled, transverse and longitudinal waves in the infinite homogeneous, isotropic medium propagate independently of each other. The velocities ratio

$$\frac{c_L}{c_T} = \sqrt{\frac{\lambda + 2\mu}{\mu}} = \sqrt{\frac{2 - 2\nu}{1 - 2\nu}} \quad (2.16)$$

depends only on the Poisson ratio of the medium. The Poisson ratio generally varies from 0. to 0.5, while for most materials it is around 0.33. This corresponds to the sound velocity ratio of 1.41 for $\nu = 0$ and 1.99 for $\nu = 0.33$, respectively. The sound velocity

ratio goes to infinity as ν approaches 0.5, which is the Poisson ratio typical for incompressible materials, such as fluids, that do not support shear waves.

If the medium is not homogeneous and consists of several distinct regions, the boundary conditions at the interfaces may cause coupling between longitudinal and transverse waves. Depending on the physical problem and the properties of the boundary, several types of boundary conditions are possible: (1) dynamic – conditions on stress components only; (2) kinematic – conditions on displacement components only; (3) combination of displacement and stress conditions; and (4) mixed, where stresses are given over one part of the boundary and displacements over the other part [39].

For a periodic medium, ρ , λ and μ are the periodic functions of the position vector and

$$f(\vec{r} + \vec{R}_0) = f(\vec{r}), \quad (2.17)$$

where $f \equiv \rho, \lambda, \mu$ and \vec{R}_0 is the lattice vector. Therefore, these functions can be expanded in the Fourier series

$$f(\vec{r}) = \sum_{\vec{G}} f_G e^{i\vec{G}\cdot\vec{r}}, \quad (2.18)$$

where \vec{G} is an inverse lattice vector. The displacement field must satisfy the Bloch theorem

$$\vec{u}(\vec{r}, t) = e^{i(\vec{k}\cdot\vec{r} - \omega t)} \sum_{\vec{G}} \vec{u}_{\vec{k}}(\vec{G}) e^{i\vec{G}\cdot\vec{r}}, \quad (2.19)$$

where \vec{k} is the wave vector and $\omega = \omega(\vec{k})$ is the angular frequency. Substituting the expressions for ρ , λ , μ , and \vec{u} into the original wave equation and keeping only a finite

number (typically 10-200) of lower order terms in the Fourier expansion, one obtains an eigenvalue matrix equation, from which the phonon dispersion relation $\omega = \omega(\vec{k})$ of the periodic medium and the unknown coefficients $\vec{u}_{\vec{k}}(\vec{G})$ in the Bloch expansion can be derived.

2.3 Brillouin light scattering

2.3.1 *Physics of a Brillouin light scattering process*

Brillouin light scattering arises as a result of acousto-optical interactions in a scattering medium. When an acoustic wave propagates through the medium, it creates modulations in the medium dielectric constant ϵ , which, in turn, scatter light. The dielectric constant of the medium is then

$$\epsilon = \epsilon_0 + \delta\epsilon_{ij}, \quad (2.20)$$

where ϵ_0 is the dielectric constant of the unmodulated medium and

$$\delta\epsilon_{ij} = \sum_{k,l} p_{ijkl} u_{kl}. \quad (2.21)$$

Here u_{kl} is the strain tensor and p_{ijkl} is the fourth rank tensor known as a photo-elastic tensor. This tensor describes the response of the medium to the propagating acoustic wave. The number of its independent coefficients depends of the symmetry of the medium. In particular, for cubic crystals the matrix of photo-elastic tensor is written in the form

$$p_{IK} = \begin{pmatrix} p_{11} & p_{12} & p_{12} & 0 & 0 & 0 \\ p_{12} & p_{11} & p_{12} & 0 & 0 & 0 \\ p_{12} & p_{12} & p_{11} & 0 & 0 & 0 \\ 0 & 0 & 0 & p_{44} & 0 & 0 \\ 0 & 0 & 0 & 0 & p_{44} & 0 \\ 0 & 0 & 0 & 0 & 0 & p_{44} \end{pmatrix}. \quad (2.22)$$

For isotropic materials the form of this matrix is unchanged, but the number of independent components is further reduced through the relation

$$p_{44} = \frac{1}{2}(p_{11} + p_{12}). \quad (2.23)$$

The kinematics of the scattering process is described by the laws of conservation of energy and wave vector for a photon-phonon scattering event, see fig 2.1 (a):

$$\vec{q}_s - \vec{q}_i = \pm \vec{k}, \quad (2.24)$$

$$\Omega_s - \Omega_i = \pm \omega.$$

Here \vec{q} and \vec{k} , Ω and ω are the photon and phonon wave vectors and frequencies respectively, indices i and s refer to the incident and scattered light respectively. The sign \pm is used to describe the possibility of both phonon emission (Stokes process) and absorption (anti Stokes process) during the scattering event. Both Stokes and anti Stokes processes are equally likely, which leads to equal intensity of up-shifted and down-shifted peaks in Brillouin spectra. In a periodic medium the momentum conservation equation is modified to include the reciprocal lattice vector \vec{G} :

$$\vec{q}_s - \vec{q}_i = \pm \vec{k} + \vec{G}. \quad (2.25)$$

Since \vec{G} depends on the lattice constants, Brillouin light scattering can be used to determine lattice constants of periodic materials. The sound velocity is much smaller than the speed of light; thus

$$|\vec{q}_s| \approx |\vec{q}_i|, \quad (2.26)$$

which allows deriving a simple relation between the phonon wave vector and the scattering angle

$$|\vec{k}| = 2|\vec{q}| \sin\left(\frac{\theta}{2}\right) \quad (2.27)$$

from the vector diagram shown in fig. 2.1 (b).

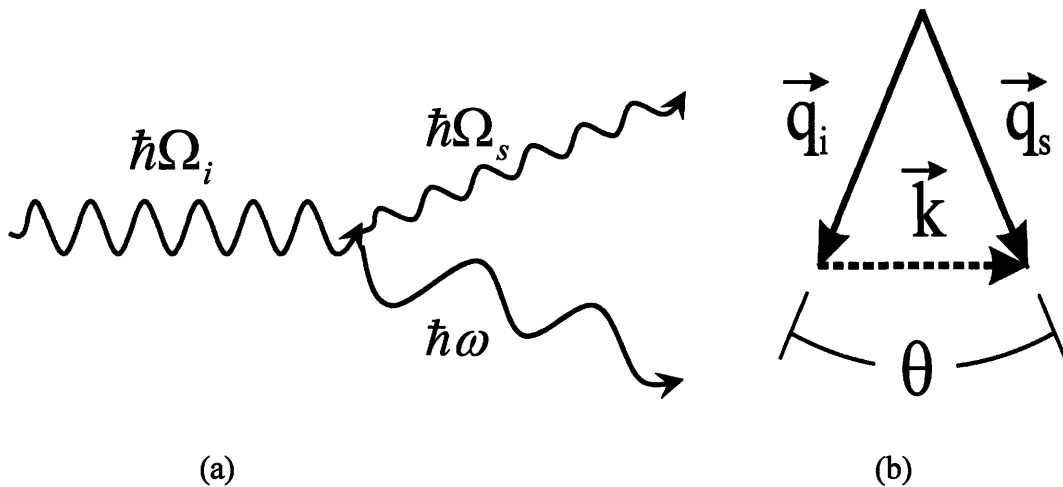


Figure 2.1. Brillouin light scattering: (a) schematic diagram of a photon-phonon scattering event, (b) momentum conservation during Brillouin light scattering.

The angle θ in the equation is the angle between the propagation directions of photons and a phonon that participate in the scattering event. Generally it is not equal to the scattering angle, i.e. the angle between incident and scattered laser beams due to refraction of the incident and/or scattered light. Thus, in practice the dependence between phonon wave vector and the scattering angle is more complicated and depends on the

refractive index of the sample as well as the scattering geometry used in each particular experiment.

The intensity of the photon-phonon scattering depends strongly on the elastic displacement field distribution in a given phonon mode. To identify which phonon modes scatter light strongly enough to be detected experimentally one must compute intensities and polarizations of light scattered by each mode. Following the treatment by Landau for an isotropic medium [40], the electric field in the scattered wave \vec{E}_s is proportional to the vector product $(\vec{n} \times (\vec{n} \times \vec{G}))$, where \vec{n} is a unit vector in the scattering direction, and the components of the vector \vec{G} are given by the integral

$$G_i = \int \delta\epsilon_{ik} \exp(-i\vec{q}_s \cdot \vec{r}) dV \cdot e_k. \quad (2.28)$$

Here \vec{e} is a unit vector parallel to the incident electric field vector $\vec{E}_i = \vec{e} E_0 \exp(i\vec{q}_i \cdot \vec{r})$;

$\delta\epsilon_{ik}$ is the change in the electrical permittivity due to elastic deformation –

$$\delta\epsilon_{ik} = p_{12}u_{ik} + p_{11}u_{ll}\delta_{ik}, \text{ where } u_{ik} = \frac{1}{2} \left(\frac{\partial u_i}{\partial x_k} + \frac{\partial u_k}{\partial x_i} \right) \text{ is a strain tensor and } p_{11} \text{ and } p_{12}$$

are the photo-elastic constants of the medium. The integration is done over the scattering volume. In case of a plane wave propagating in a homogeneous medium, the integral for \vec{G} can be evaluated analytically. If the incident light is s-polarized, then: (1) in-plane transverse modes do not scatter light; (2) light scattered by out-of-plane transverse modes is p-polarized; (3) light scattered by longitudinal modes is s-polarized. In the case of phononic crystals the displacement fields cannot be represented by plane waves and the integral for \vec{G} must be evaluated numerically. To estimate scattering intensities in this

case, one must first compute details of the displacement fields of various propagation modes in phononic crystals.

2.3.2 *Design and operation of a Brillouin light scattering apparatus*

Brillouin light scattering is ideally suited for investigations of hypersonic crystals because it allows direct measurement of their complete phonon dispersion relation $\omega = \omega(\vec{k})$. As a part of this study a Brillouin light scattering apparatus has been designed and built at MIT. This section briefly discusses principles behind the design and operation of the Brillouin light scattering apparatus. It serves as a practical reference in Brillouin spectroscopy and its applications towards characterization of periodic materials.

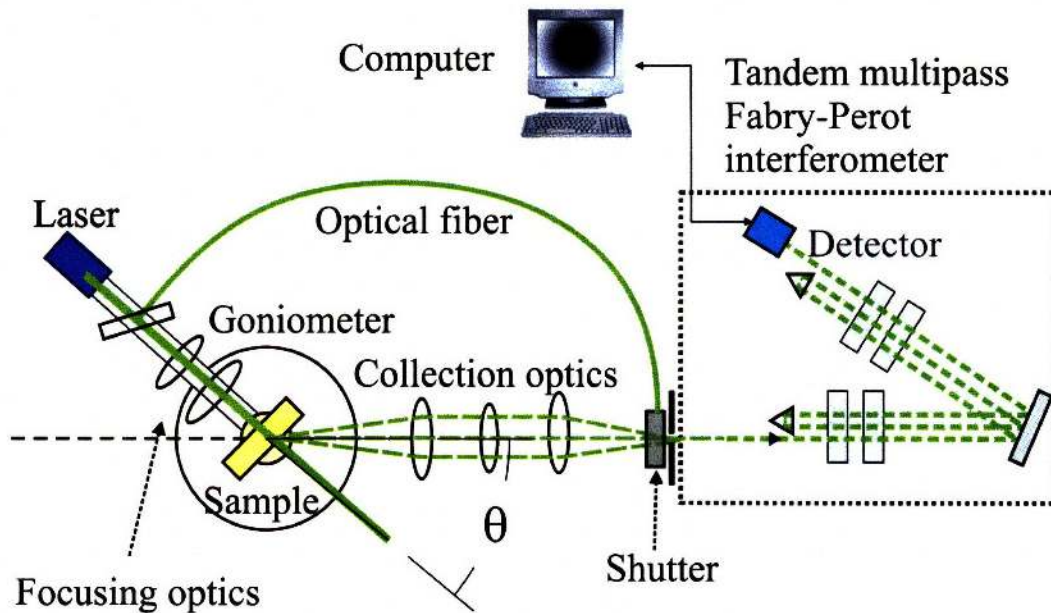


Figure 2.2. Schematic of the BLS apparatus.

A schematic of the BLS apparatus is shown in figure 2.2. The main components are a light source, focusing and collection optics, mounting mechanics and a tandem Fabry-Perot interferometer used for the spectral analysis of the scattered light. The light source

is a continuous wave green (532 nm) laser mounted on an arm of a goniometer. Usually several hundred mW of cw power is sufficient for most BLS experiments. More powerful lasers heat samples too much, which may cause material degradation. The laser frequency cannot be chosen arbitrarily; it must match the target operation frequency of the Fabry-Perot interferometer. Another important consideration for the laser selection is its spectral width. Since in Brillouin spectroscopy very small shifts in the light frequency (on the order of several GHz) are measured, it is critical to use lasers with very narrow spectral lines (preferably with FWHM < 10 MHz).

Most scattering geometries traditionally used in BLS experiments assume a fixed scattering angle, usually 90° or 180° [41]. This approach is simple because all optical components are stationary and do not need to change their position during operation. However, it only allows accessing one or very few phonon wave vectors, which is not sufficient for dispersion relation measurements. Therefore, we use an angle-resolved Brillouin setup with a sample mounted in the center of the goniometer. In this setup measurements at any scattering angle from nearly 0 to 180 degrees are possible both in transmission and reflection, see figure 5. As a result, a wide range of the phonon wave vectors (roughly 1 – 35 μm^{-1}) can be accessed. The sample holder uses a separate rotation stage to adjust the orientation of the sample in the plane is normal to the scattering plane. For single crystalline samples this adjustment allows measuring phonon dispersion along any desired direction in the Brillouin zone. Finally, most experiments described in this thesis are done in transmission geometry, where the angle ϕ between the incident light and the normal to the sample surface is equal to the half of the scattering angle θ , see

figure 2.3. The unique experimental advantage of this geometry is that the phonon wave vector does not depend on the refractive index of the sample due to mutual cancellation of the refraction effects at the front and back faces of the sample. It can be shown that the phonon wave vector in this case is given by a simple formula

$$k = \frac{4\pi}{\lambda_0} \sin\left(\frac{\theta}{2}\right), \quad (2.29)$$

where $\theta = 2\phi$ is the scattering angle and λ_0 is the wavelength of the laser light in vacuum.

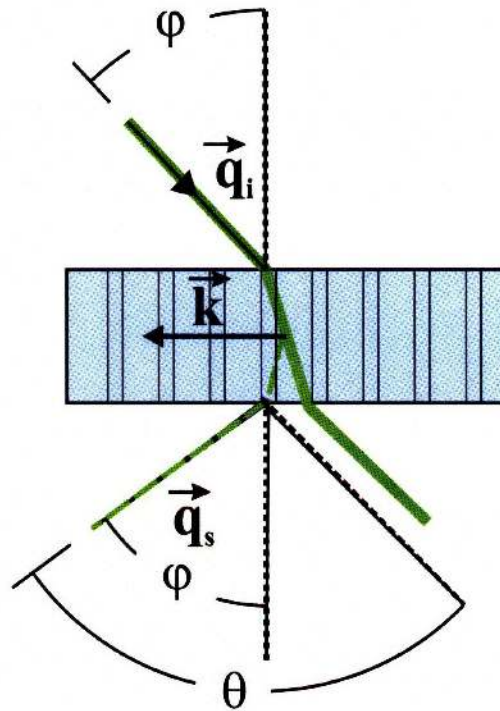


Figure 2.3. Symmetric scattering geometry in the transmission BLS experiments. The angle between the incident light and the normal to the sample plane is equal to the angle between the scattered light and the normal to sample plane. In this geometry the phonon wave vector that is probed by BLS does not depend on the refractive index of the sample.

The focusing and collection optics are very important parts of the BLS apparatus. The focusing optics consists of a polarizer, which is used to maintain polarization of the incident light normal to the scattering plane (s polarized) and a focusing lens (figure 2.2),

which focuses light into a spot of about 200 μm in diameter inside a sample, where scattering takes place. The spot size is small compared to the sample size (generally several mm to several cm), which insures uniformity during data acquisition. The scattered light is collected by a collection lens; passes through a second polarizer, where the desired polarization is selected; and then it is focused onto an input pinhole of the Fabry-Perot interferometer with an additional lens. A scattering geometry in which both polarizers are oriented vertically (normal to the scattering plane) is called the VV geometry and it is used to measure light scattered by longitudinal phonons. In contrast, the scattering geometry in which the focusing polarizer is oriented vertically and the collection polarizer is oriented horizontally is called the VH geometry and it is used to measure light scattered by transverse phonons (see the previous section for the derivation of polarizations and intensities of light scattered in Brillouin experiments).

Proper selection and precise alignment of the focusing and collection optics is critical to receive meaningful data in angle-resolved Brillouin spectroscopy. The following issues are particularly important: (1) numerical apertures of the collection and focusing lenses; (2) mounting the sample holder *precisely* in the center of the goniometer; and (3) correct alignment of apertures that define the paths of the incident and scattered light.

The amount of light collected in scattering experiments is determined by the numerical aperture of the collection lens according to the equation $NA = n \sin(\alpha)$, where n is the refractive index of the medium (most measurements described in this thesis are done in air with $n = 1$) and α is the half-angle of the maximum cone of light that enters the lens.

Selecting lenses with large numerical apertures allows more light to be collected and increases the signal. Unfortunately, it also leads to larger uncertainties in the values of the scattering angle, since all photons with scattering angles from $\theta - \alpha$ to $\theta + \alpha$ are collected, and thus it increases uncertainties in the phonon wave vectors. While this may not be a problem for studying processes with frequencies independent of the wave vector, such as eigen vibrations of individual microparticles; it poses significant difficulties for measuring the dispersion relation of phononic crystals. Therefore, the numerical aperture of the collection lens must be optimized for each particular set of samples and experimental conditions. The same considerations apply to some extent to the focusing lens as well. The size of the numerical aperture must be chosen such that the spectral line width due to the collection of light from $\theta - \alpha$ to $\theta + \alpha$ scattered by phonons with a range of wave vectors from $\vec{k} = \vec{k}(\theta - \alpha)$ to $\vec{k} = \vec{k}(\theta + \alpha)$ is smaller than the instrumental line width of the Fabry-Perot interferometer, which is determined by the spacing between the Fabry-Perot mirrors, as described in the Fabry-Perot manual [44].

Precise matching of the sample holder and the goniometer centers is necessary to insure that light is collected from the same spatial region of the sample during scans at different scattering angles. This is important, since some samples may not be uniform on the mm length scale. In addition, incorrect alignment of the sample holder with respect to the goniometer causes systematic errors in determination of the scattering angle, which severely undermines the accuracy of BLS measurements. Finally, precise positioning of apertures in the focusing and collection optics is necessary to insure that the paths of the

incident and scattered light are properly defined and correct values of the scattering angle are used in further calculations and data analysis.

2.3.3 Tandem multipass Fabry-Perot interferometer and its applications in Brillouin spectroscopy

Light scattered in Brillouin experiments has several spectral components. The strongest one is at the incident light frequency corresponding to elastic scattering from static inhomogeneities of the sample. The Brillouin components with frequency shifts $\Delta f / f_0 \sim 10^{-5}$ are scattered by various dynamic processes, such as phonons, plasmons, spin waves, etc. The intensity of the elastically scattered light is usually many orders of magnitude larger than that of the Brillouin light. Therefore, it is necessary to separate a very weak signal shifted in frequency only by a small amount from a much stronger elastic background. This imposes extremely demanding requirements on the performance of the interferometer. Usually, highly stable scanning with long acquisition times (typical acquisition time varies from 10 minutes to several days), contrast ratio of 10^{10} , free spectral range of 5-100 GHz and resolution of <100 MHz is necessary. These requirements can only be met in a tandem multipass operation of the interferometer [42,43].

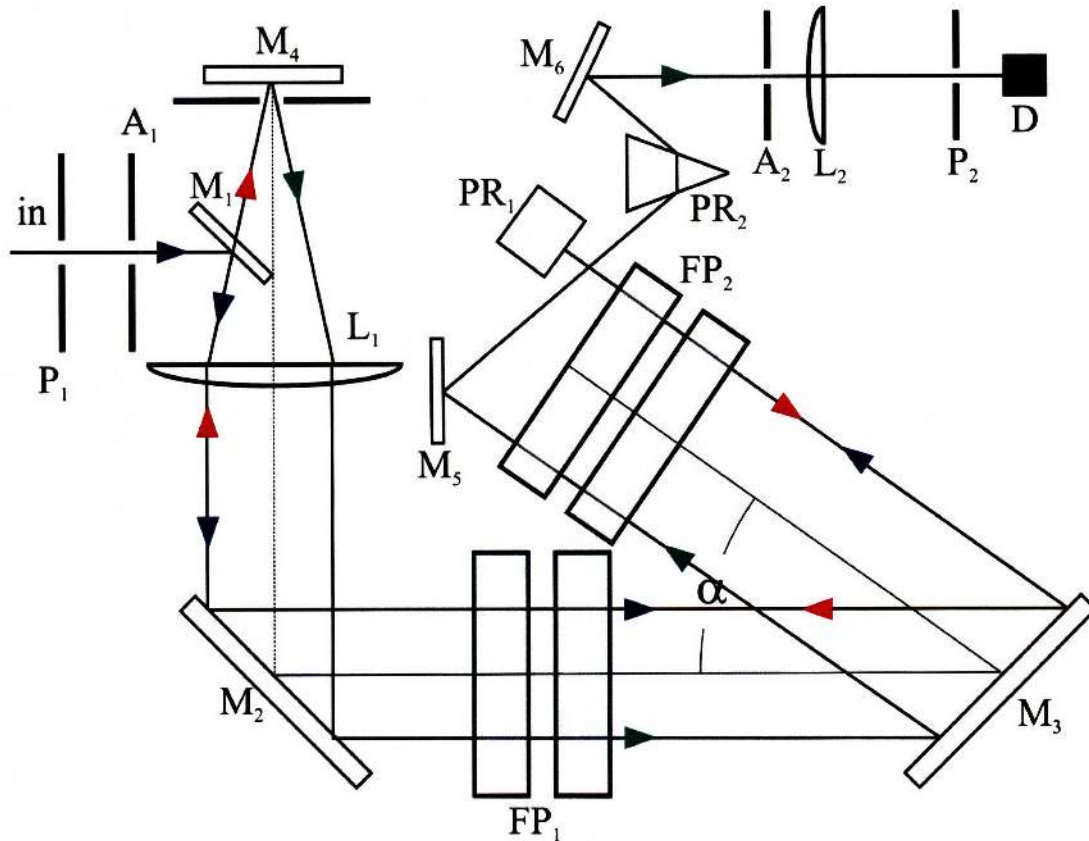


Figure 2.4. The path of light inside a tandem six-pass Fabry-Perot interferometer manufactured by JRS Scientific Instruments. The figure is adapted from reference [44].

The path of light inside a tandem six-pass Fabry-Perot interferometer made by JRS Scientific Instruments is schematically shown in figure 2.4 [44]. Light enters through an input pinhole P_1 and an aperture A_1 , gets collimated by a lens L_1 and then it is redirected to pass through both sets of Fabry-Perot mirrors FP_1 and FP_2 with the help of mirrors M_1 , M_2 and M_3 , as marked with blue arrows in figure 2.4. Then a prism PR_1 is used to reflect it back parallel to its original trajectory to pass through FP_1 and FP_2 second time and reach a mirror M_4 , as shown with red arrows in the figure. Upon reflection from M_4 light passes one more time through FP_1 and FP_2 and then it is redirected by a prism PR_2 and mirrors M_5 and M_6 to reach an avalanche photon counter D , as shown with green arrows in figure 2.4.

Transmissivity of each set of Fabry-Perot mirrors is given by the expression

$$T = \frac{\tau_0}{1 + \left(4F^2/\pi^2\right)\sin^2(2\pi L/\lambda)} \quad (2.30)$$

where τ_0 (< 1) is the maximum possible transmissivity determined by the losses in the system, L is the optical spacing between mirrors and F , the finesse, is a quality factor limited by the mirror reflectivity and flatness [44]. Generally it is difficult to achieve values of the finesse higher than 100. It is easy to see that only wavelengths satisfying the relation

$$L = \frac{1}{2} p\lambda \quad (2.31)$$

for an integer p will be transmitted. The transmissivity function for $\tau_0 = 0.9$ and $F = 50$ is plotted in figure 2.5.

There are three main parameters that describe the performance of a Fabry-Perot interferometer: (1) resolution, (2) contrast, defined as the ratio of the highest to the lowest transmissivity, and (3) free spectral range (FSR), which determines the maximum scan range for a given mirror spacing. The resolution is determined by the width of the transmissivity peak $\delta\lambda$, FSR – by the distance between two consecutive peaks $\Delta\lambda$, see figure 2.5. The resolution and FSR are related to each other through the expression

$$\frac{\Delta\lambda}{\delta\lambda} = F. \quad (2.32)$$

Since $\Delta\lambda = \frac{\lambda^2}{2L}$, the FSR can be made arbitrary large by decreasing the mirror spacing L .

However, this will also increase $\delta\lambda$ and reduce the resolution. Therefore it is necessary to optimize L for each experiment according to the expectations for the lowest and the highest frequencies to be recorded. Sometimes one must use two different mirror spacings for each sample: large – to capture the low frequency phenomena with high resolution, and small – to record the high frequency part of dispersion relation with large FSR.

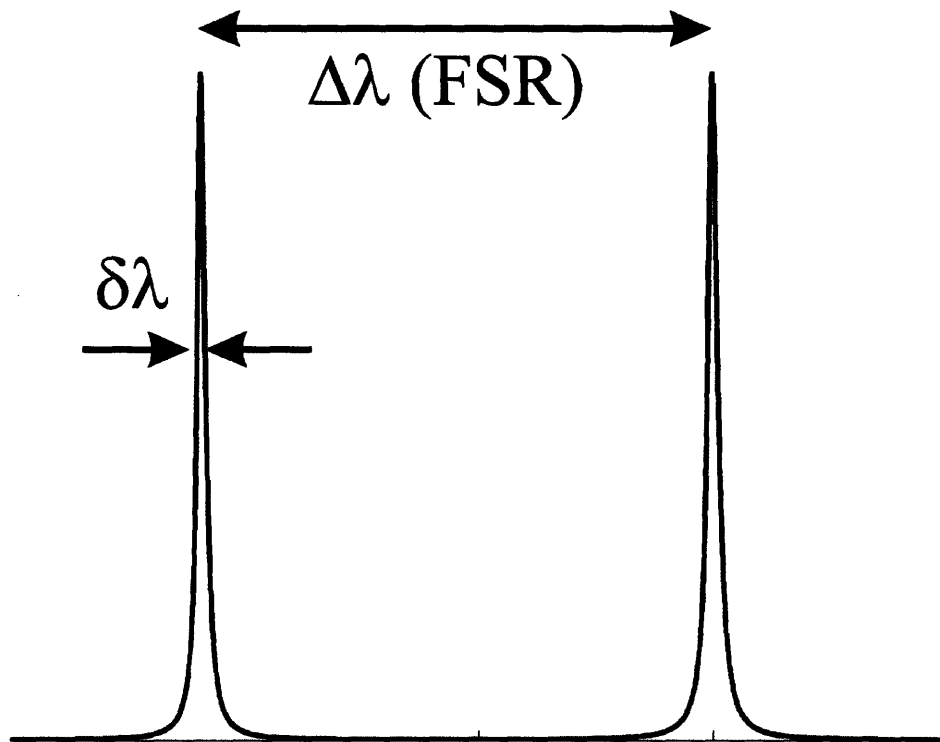


Figure 2.5. Transmissivity of a single set of Fabry-Perot mirrors with finesse $F = 50$, adapted from reference [44].

Contrast is the ratio of the highest to the lowest transmissivity,

$$C = \frac{T_{\max}}{T_{\min}} \approx \frac{4F^2}{\pi^2}. \quad (2.33)$$

With the finesse of about 100, contrast of roughly 10^3 can be achieved in a single pass operation. However, if light is made to pass n times through Fabry-Perot mirrors, the resultant contrast becomes $C_n = (C_0)^n$, which for our system is about 10^{12} . Dramatic increase in contrast is a great advantage of the multipass operation, which enables the use of tandem Fabry-Perot interferometers in very sensitive Brillouin measurements.

Acquisition time for a single Brillouin spectrum is usually large, from tens of minutes to several days. Perfect alignment and parallelism of Fabry-Perot mirrors with nm precision is required during this time. Real-time feedback loops and piezoelectric controllers are used to compensate for random drifts of Fabry-Perot mirrors and keep the operation of the interferometer stable. In practice it is realized by optimizing mirrors spacing and orientations for the maximum transmissivity at the incident light frequency during each scan cycle. It is not convenient to use the scattered light for stabilization because it has several spectral components and its intensity can vary depending on experimental conditions. A good practical solution is to take away a small portion of light from the incident beam before it hits the sample and use it to keep operation of the interferometer stable. In our design this is done with help of an optical fiber that delivers a reference beam into the interferometer, as shown in figure 5. An electronically-controlled shutter closes for a fraction of a measurement cycle to block the scattered light and allow only the reference beam into the interferometer. Once the stabilization is complete, the shutter switches its position to block the reference beam and allow only the scattered light for remaining of the scan cycle. As a result, measurements can be run with high accuracy and stability for extended periods of time.

As a part of this investigation, a Brillouin light scattering apparatus has been designed and constructed in our optics laboratory at MIT (room 13-5140). It is mounted on a dedicated anti-vibration table that uses real-time feedback loops and piezoelectric actuators to reduce vibrations and allow highly stable measurements over long acquisition times. Most BLS spectra described in this thesis have been acquired using this apparatus.

2.4 Interference lithography for fabrication of single crystalline phononic structures

Interference lithography (IL) is a very valuable technique for the fabrication of hypersonic phononic crystals. It allows creating a variety of 1D, 2D and 3D single crystalline patterns and even 2D and 3D quasicrystalline patterns with the feature size on the submicron scale. Its advantages include access to a wide range of lattice symmetries, very low defect concentration, fast and efficient processing and the potential for making large area samples [45-48]. IL involves the formation of a stationary spatial variation of light intensity created by the interference of two or more beams of light. This intensity pattern is then transferred to a light sensitive medium, such as a photoresist, to yield structures.

The electric field associated with a monochromatic plane wave can be described mathematically as:

$$\vec{E}_m(\vec{r}, t) = \vec{E}_{0,m} e^{i(\vec{k} \cdot \vec{r} - \omega t + \phi_m)}, \quad (2.34)$$

where m is an index identifying the particular beam, \vec{E}_0 is the wave amplitude and direction of polarization, \vec{k} is the wave vector, ω is the angular frequency, and ϕ is the phase. Note, \vec{k} is not referring to the *phonon* wave vectors in this section, but to the wave vectors of laser beams. The intensity distribution created by a set of beams is proportional to the square of the magnitude of the resultant vector sum,

$$I(\vec{r}) = \sum_{m=1}^n \sum_{l=1}^n \vec{E}_l \vec{E}_m^* e^{i((\vec{k}_l - \vec{k}_m) \cdot \vec{r} + \phi_l - \phi_m)}. \quad (2.35)$$

This intensity distribution has its translational periodicity determined by the difference between the wave vectors $\vec{k}_l - \vec{k}_m$ of the interfering beams, while the polarizations, represented by a set of complex electric field vectors, determine the pattern or motif placed within the unit cell. The combination of the motif and the translational periodicity determines the full set of symmetries associated with the resultant structure and hence its space group [49-51].

To fabricate a crystal with symmetry that belongs to a particular space group, one needs to be able to determine the proper values of \vec{k} and \vec{E} . Since the intensity equation is essentially the Fourier transform of the crystal, these values can be computed by equating the intensity equation to the structure factor of the space group. (The structure factor describes the amplitudes and phases of the three-dimensional diffraction pattern due to the scattering of incident radiation from the planes (hkl) of the crystal). The resultant set of equations is then solved to yield the beam parameters that are required to obtain the structure belonging to the desired space group [50].

Once the desirable light intensity distribution is achieved, it must be transferred into a photoresist to form the structure. There are two types of resists: positive and negative. A negative photoresist is a resist in which the regions exposed to light become insoluble to the developer. This insolubility can be achieved by (1) an increase in molecular weight and the formation of a crosslinked polymer network, or (2) photochemical rearrangement to form new insoluble products. One common negative photoresist for interference lithography is SU-8, an epoxy based monomer that undergoes cationic photopolymerization. It has many advantages, such as chemical amplification, which increases the sensitivity; mechanical robustness, which allows access to high aspect ratio structures; and wide processing latitude with respect to radiation wavelengths [52,53]. For many applications it is desirable to infiltrate IL patterned polymeric structures with other materials (for example high refractive index materials for photonic crystals) and then to remove the original polymer structure. However, removal of highly cross-linked polymers templates (which are usually obtained if negative resists are used) is difficult and may require rather extreme processing such as resist burning or plasma etching [54,55]. This can result in damage to the material that was back filled into the template and hence negative resist removal has been a bottle neck for the fabrication of 3D templates.

A positive resist is a photoresist in which regions exposed to light become soluble to the developer, while unexposed regions remain insoluble. A commonly used positive resist is composed of diazonaphthoquinone (DNQ) and novolac resin (a phenol formaldehyde resin). The phenolic resin is highly soluble in basic solution and has excellent film

forming properties. DNQ acts as both photosensitizer and dissolution inhibitor. Upon exposure, DNQ undergoes molecular rearrangement generating a carboxylic acid, and the exposed area becomes soluble in basic developers, resulting in a positive image in regions of high light intensity. Positive resists have the advantage over negative resists in that they do not undergo shrinkage from cross-linking and can be easily removed after an infiltration step by flood exposure followed by dissolution in a second developer treatment [56]. A comparison of the fabrication process with positive and negative resists that were used to fabricate structures described later in this thesis (Chapters 4, 5) is shown in figure 2.6 (a) and schematic diagrams of the basic chemical mechanisms responsible for the function of two different types of photoresists are shown in figs. 2.6 (b) and 2.6 (c).

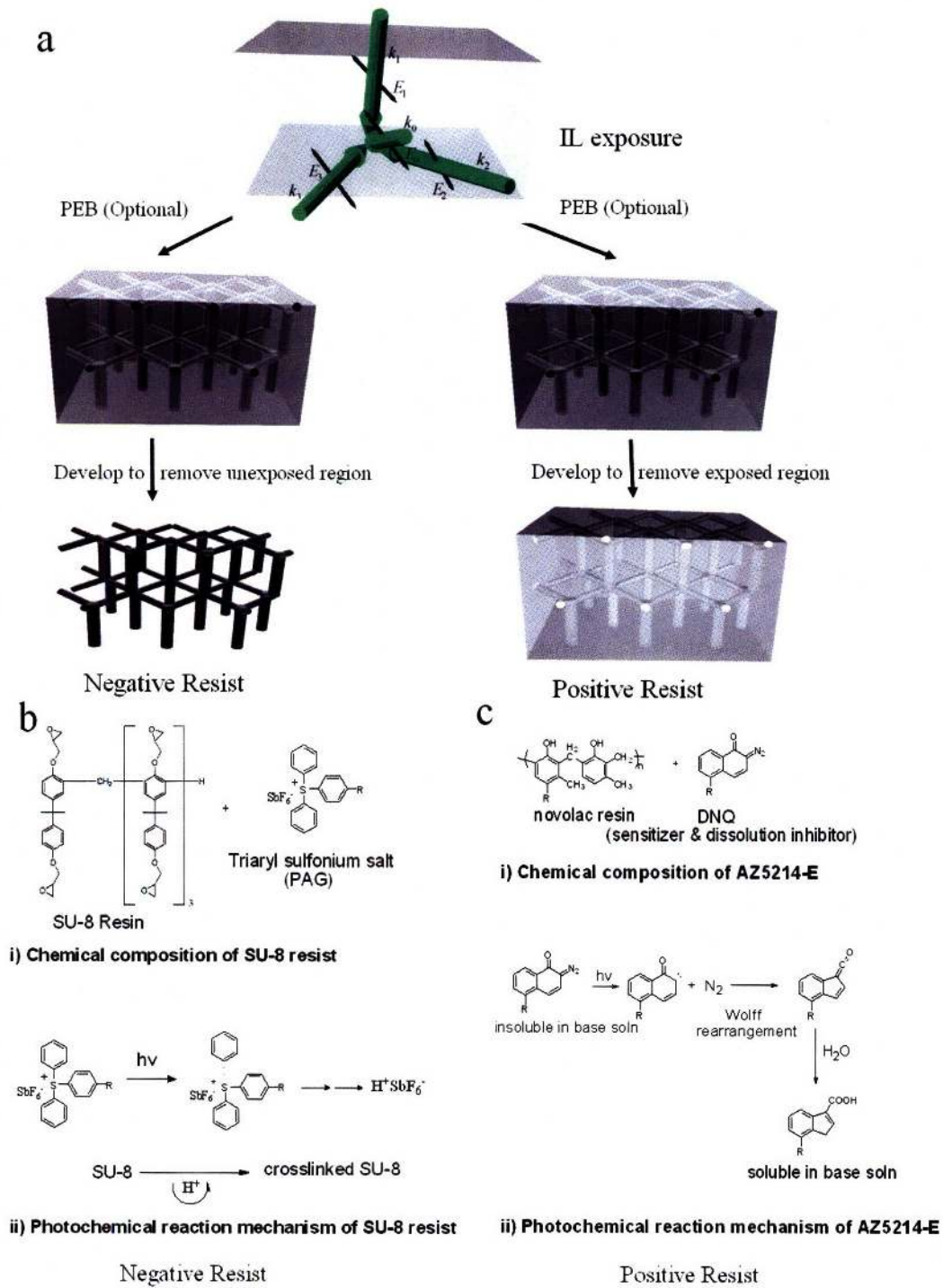


Figure 2.6. (a) Schematic diagram of the 4 beam interference lithography process, the beams have directions \vec{k}_i and polarizations \vec{E}_i given by the green and black arrows, respectively; (b) general photochemistry schemes for exposure of two different types of common photoresists; (c) SU-8 negative resist and DNQ-novolac positive resist [45].

CHAPTER 3. PHONONIC PROPERTIES OF 1D MULTILAYER PERIODIC SELF-SUPPORTING POLYMER FILMS

3.1 Introduction

One dimensional (1D) phononic crystal are the simplest, yet very important class of phononic materials. From a theoretical viewpoint, properties of 1D systems can be studied with a number of relatively simple analytical and semi-analytical techniques, such as Bloch expansion or the transfer matrix method, without need for extensive numerical computations. At the same time, many phenomena in 1D crystals are analogous to those in more complex 2D and 3D crystals. Thus, 1D crystals represent an excellent learning platform to gain a basic understanding of phononic crystals.

For an experimentalist, 1D crystals also offer a number of important advantages. The main one is the ease of fabrication. 1D systems can be made using multilayer deposition, self-assembly or coextrusion with precise control over the dimensions and properties of each layer. Fabrication of defect cavities can be easily integrated into existing manufacturing routines. Furthermore, 1D crystals have found numerous applications in optics, acoustics and other fields of science and engineering. Understanding the phononic properties of 1D crystals (with and without purposeful defect layers) can improve the efficiency of existing devices as well as lead to the development of new ones.

This chapter describes phononic properties of 1D hypersonic crystals. First, general features of their phononic band diagrams are discussed for elastic waves propagating

along the periodicity direction of a crystal. Then, the phonon dispersion for the in-plane propagation in free standing, periodic multilayer anisotropic poly(methylmethacrylate)/poly(ethylene terephthalate) (PMMA/PET) and isotropic poly(carbonate)/poly(methylmethacrylate) (PC/PMMA) films is studied as a function of a lattice constant and composition. As the lattice constant increases, additional propagation modes appear in the phonon dispersion relations of these structures. These modes represent layer-guided phonons propagating within individual layers and not throughout the multiple layers, where the film's properties would correspond to an effective homogeneous medium. As a result, their dispersion relation provides valuable information about the elastic constants of polymer nanolayers. Furthermore, the glass transition temperatures of the nanolayers can be estimated from the temperature dependence of sound velocities of these phonon modes. Thus, BLS can be used as a nondestructive technique to obtain quantitative information about mechanical and thermodynamic properties of polymer nanolayers.

3.2 Normal phonon propagation in 1D phononic crystals

This section describes general features of the phononic dispersion relation in 1D crystals for waves propagating normal to the periodicity direction. Two material systems are investigated – PC/PMMA and SiO₂/PMMA periodic multilayer films with symmetric 50/50 compositions. Figure 3.1 shows phononic band diagrams for 1D PC/PMMA (a) and SiO₂/PMMA (b) crystals computed using finite element analysis (FEA). The densities, sound velocities, elastic constants and glass transition temperatures of these materials are listed in table 3.1.

Table 3.1. Mechanical properties and glass transition temperatures of PC, PMMA and SiO₂.

Material	Density (g/cm³)	c_L (m/s)	c_t (m/s)	E (GPa)	ν	T_g (°C)
PC	1.3	2433	1070	4.1	0.38	140
PMMA	1.2	2851	1401	6.3	0.34	105
SiO ₂	2.2	5972	3766	73	0.17	1175

The longitudinal and transverse modes are plotted with solid and dashed lines, respectively. Since the contrast in densities and sound velocities is low for PC/PMMA crystals, but high for SiO₂/PMMA crystals, the behavior of these systems is very different. The phonon dispersion relation of the PC/PMMA crystal resembles that of a homogeneous medium with linear dependence between ω and k for the entire range of k values except near the Brillouin zone edges. No complete phononic band gaps are present, but several partial gaps for both longitudinal (highlighted in red) and transverse (highlighted in green) modes are clearly visible at the edges of the Brillouin zone.

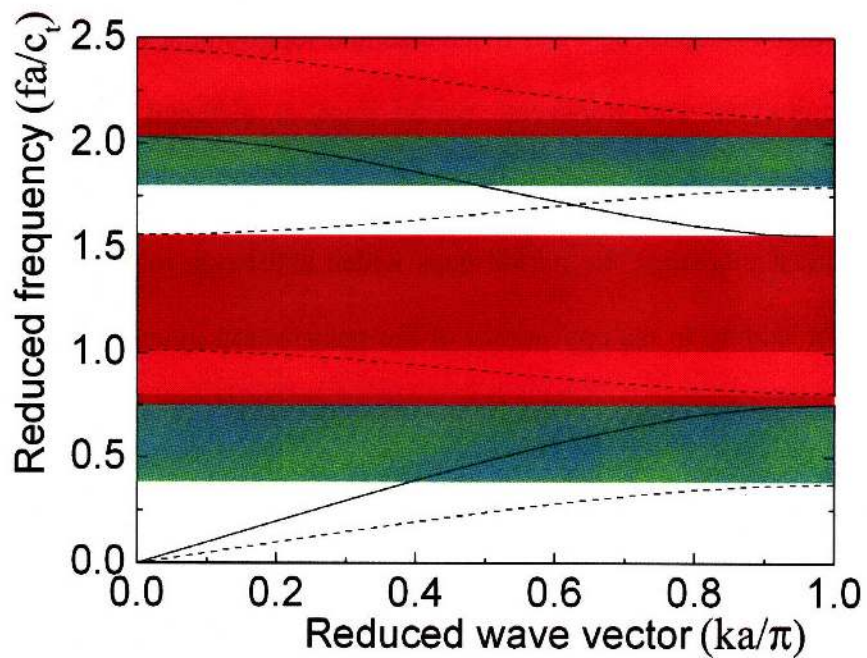
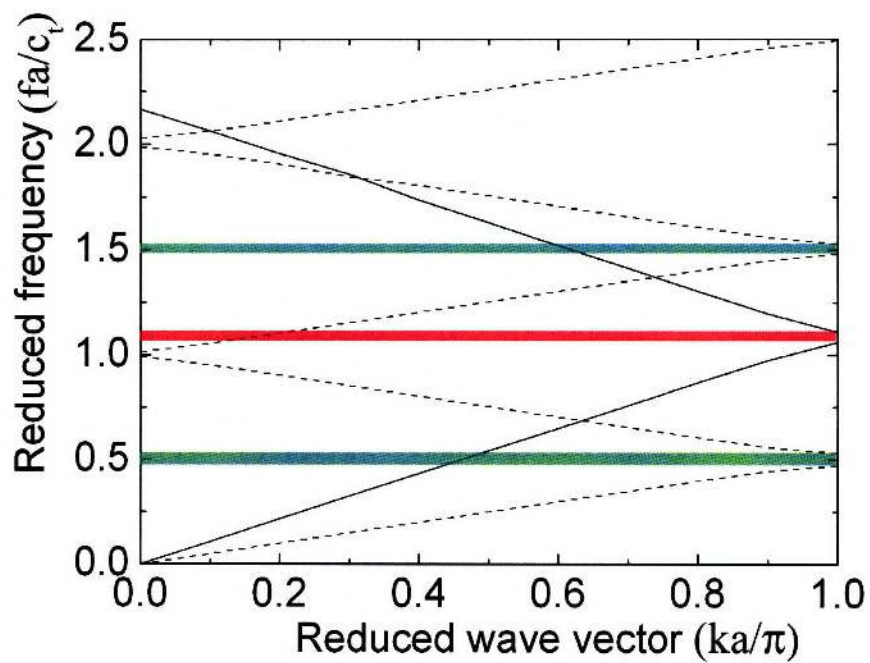


Figure 3.1. Band diagrams of PC-PMMA (a) and SiO₂-PMMA (b) 1D phononic crystals with symmetric compositions; solid and dashed lines represent the longitudinal and transverse modes, respectively; red and green is used to highlight the positions of the longitudinal and transverse band gaps, respectively; their intersection displayed in dark red shows the positions of complete phononic band gaps for phonons propagating normal to the layers.

In contrast, in the SiO₂/PMMA film, the dependence between ω and k is nonlinear for the entire range of k and there is a substantial amount of band bending. Large mechanical contrast between ceramic SiO₂ and polymeric PMMA layers leads to the overlap between transverse and longitudinal band gaps and the formation of several polarization independent phononic band gaps, which are highlighted in dark red in fig. 3.1 (b). Note that, unlike the electromagnetic case where for any $\Delta n \neq 0$ TE and TM partial gaps for normal propagation coincide, considerable mechanical contrast ($\frac{\rho_{SiO_2}}{\rho_{PMMA}} = 1.8$,

$$\frac{c_{L_SiO_2}}{c_{L_PMMA}} = 2.1, \frac{c_{t_SiO_2}}{c_{t_PMMA}} = 2.7$$

) is required to open a polarization independent band gap for normal propagation in 1D solid-solid phononic crystals. This is due to the substantial difference in sound velocities between transverse and longitudinal modes, which causes opening of longitudinal and transverse partial gaps at different frequencies. If the mechanical contrast is small, these partial gaps are narrow and do not overlap. As mechanical contrast increases, the partial gaps widen and begin to overlap in the same frequency region leading to the appearance of the polarization independent band gap. In addition to mechanical contrast, the ratio of longitudinal to transverse velocities

$$\frac{c_L}{c_t} = \sqrt{\frac{2-2\nu}{1-2\nu}}$$

is important, since it determines the separation between the mid-gap frequencies of the longitudinal and transverse partial gaps. This ratio is typically between 1.4 and 2 for most materials; however, some rubbers with $\nu \rightarrow 0.5$ have very high c_L/c_t ratios of ~ 100 or more.

3.3 In-plane phonon propagation in 1D periodic anisotropic poly(methyl methacrylate)/poly(ethylene terephthalate) films [57]

3.3.1 *Phononics of giant birefringence optical polymer mirrors*

The remainder of this chapter is dedicated to the in-plane propagation of phonons in 1D crystals. The in-plane propagation (\vec{k}_{\parallel}) is notably different from the normal propagation (\vec{k}_{\perp}) discussed in the previous section, mainly because no band gaps form for elastic waves propagating parallel to the film layers, since there is no periodicity in this direction. Instead, under certain conditions, layer-guided modes are observed. The dispersion relation of these modes is a strong function of layer thickness, orientation and elastic constants. Thus, BSL can be used as a nondestructive technique to obtain information about mechanical and morphological properties of individual nanolayers. In-plane measurements also have an important experimental advantage. The transmission scattering geometry, which is the primary scattering geometry for angle-resolved BLS measurements, as described in section 2.3.2, requires that the phonon wave vector be parallel to the sample surface. Since in coextruded multilayer films, the layers are oriented parallel to the film surface, the use of the transmission scattering geometry automatically assumes in-plane measurements.

This section reports on phononic properties of a multilayer giant birefringence polymer visible light mirror manufactured by the 3M company. It was recently shown that multilayer polymer films comprised of two different anisotropic polymers can be used to make superior dielectric stack mirrors [58]. The performance of traditional (nonomnidirectional) dielectric stack mirrors made of isotropic materials is limited by

Brewster's law, according to which the percent reflection of p-polarized light at a material interface decreases with increasing angle of incidence and ultimately vanishes at a critical angle (Brewster's angle). In contrast, multilayer mirrors made of highly birefringent polymers can be designed to maintain or even increase p-polarized reflectivity with increase in the incident angle [58].

In the past BLS has been applied to multilayer thin metal films with the main interest directed to their magnetic properties [59,60]. The only BLS experiment on polymer films with a multilayer structure was performed by Forrest *et al.* [61] on supported one to five alternating poly(styrene)/poly(isoprene) (PS/PI) spin-coated homopolymer thin films. They did not succeed, however, to resolve phonon propagation in the individual homopolymer layers (20-80 nm thick). Instead, their data corresponded to longitudinal modes in an effective medium behaving like a single component thin film despite the large sound velocity contrast between the glassy PS and the rubbery PI at room temperature. In addition, the phononic properties of the high molecular weight concentrated poly(styrene-b-isoprene) block copolymer solutions with lamellar morphology were studied by Urbas *et al.* [71]. Several propagation modes were observed and associated with the structural periodicity of these solutions. Unfortunately, the block-copolymer solutions were polycrystalline and did not allow choosing the direction of the phonon wave vector with respect to the grain orientation.

The work described in this section is the first BLS study of a free-standing periodic multilayer polymer film. Surprisingly, up to five acoustic-like modes are resolved. The

theoretical dispersion relations computed using a finite element analysis (FEA) suggest that these modes are associated with phonons propagating within individual layers. This conclusion is further supported by the measurements of temperature dependence of sound velocities of these modes, which reveal two distinct glass transition temperatures that correspond to phonons localized in poly(methyl methacrylate) (PMMA) and poly(ethylene terephthalate) (PET) layers, respectively.

3.3.2 *Sample morphology*

The sample is a 40 μm thick stack of over 200 identical bilayer units composed of 78 nm thick PMMA and 118 nm thick PET layers. The lattice constant $a = t_{PET} + t_{PMMA} = 196 \text{ nm}$. The PMMA layers are optically and mechanically isotropic, while the PET layers possess uniaxial anisotropy with $n_x = n_y \neq n_z$ and $E_x = E_y \neq E_z$. Here n_x , n_y , n_z and E_x , E_y , E_z are the refractive indices and Young's moduli along x, y, and z directions, respectively. The degree of birefringence in the PET layers was estimated from ellipsometry and polarized reflectometry measurements to be $\Delta n = 0.15$. The TEM images reveal excellent uniformity of the layers with essentially no structural defects, see fig. 3.2. The film appears blue in reflection and red in transmission when examined at normal incidence due to the presence of a photonic band gap at roughly 430 nm.

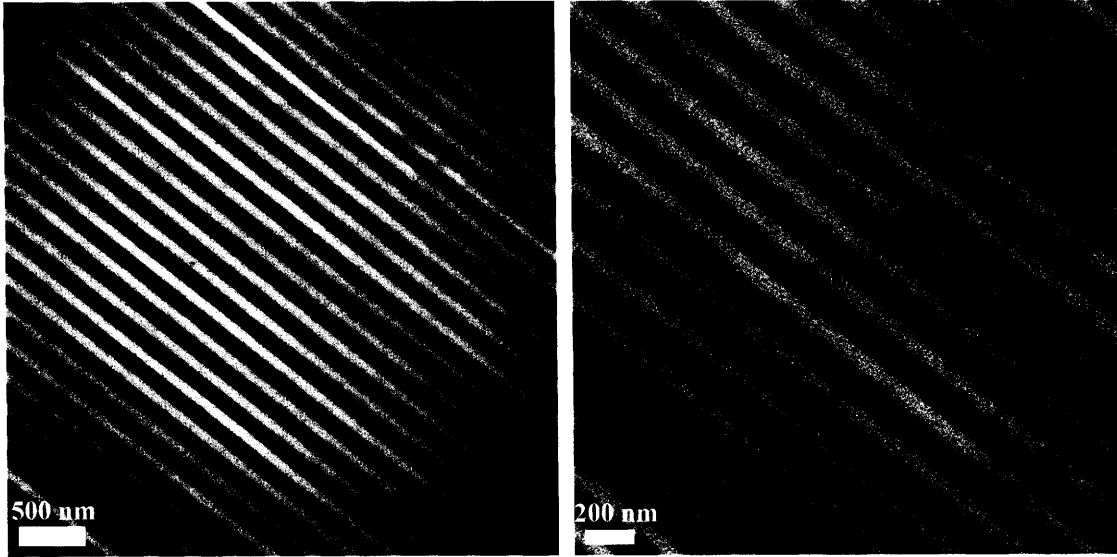


Figure 3.2. (a) Low and (b) high magnification TEM micrographs of PMMA/PET multilayer film; the PMMA layer thickness is $t_{PMMA} = 78 \text{ nm}$ and the PET layer thickness $t_{PET} = 118 \text{ nm}$ [57]. To enhance contrast the PMMA layers were preferentially stained with ruthenium tetroxide (RuO_4)

3.3.3 *Experimental dispersion relation*

Figure 3.3 shows typical ambient temperature VV Brillouin spectra measured using the transmission scattering geometry, such that \vec{k} is parallel to the layers at $k = 0.0116 \text{ nm}^{-1}$ and $k = 0.0150 \text{ nm}^{-1}$. For a better visualization, the central elastic feature due to the reference beam (adopted to stabilize the tandem Fabry-Perot interferometer) was omitted over the frequency range $\pm 1.2 \text{ GHz}$ around $f = 0$, ($f = \omega/2\pi$). The film displays up to six modes, which are well resolved in the Brillouin spectra of fig. 3.3 (a, b). These modes are successively labeled from 1 to 6 in order of increasing frequency.

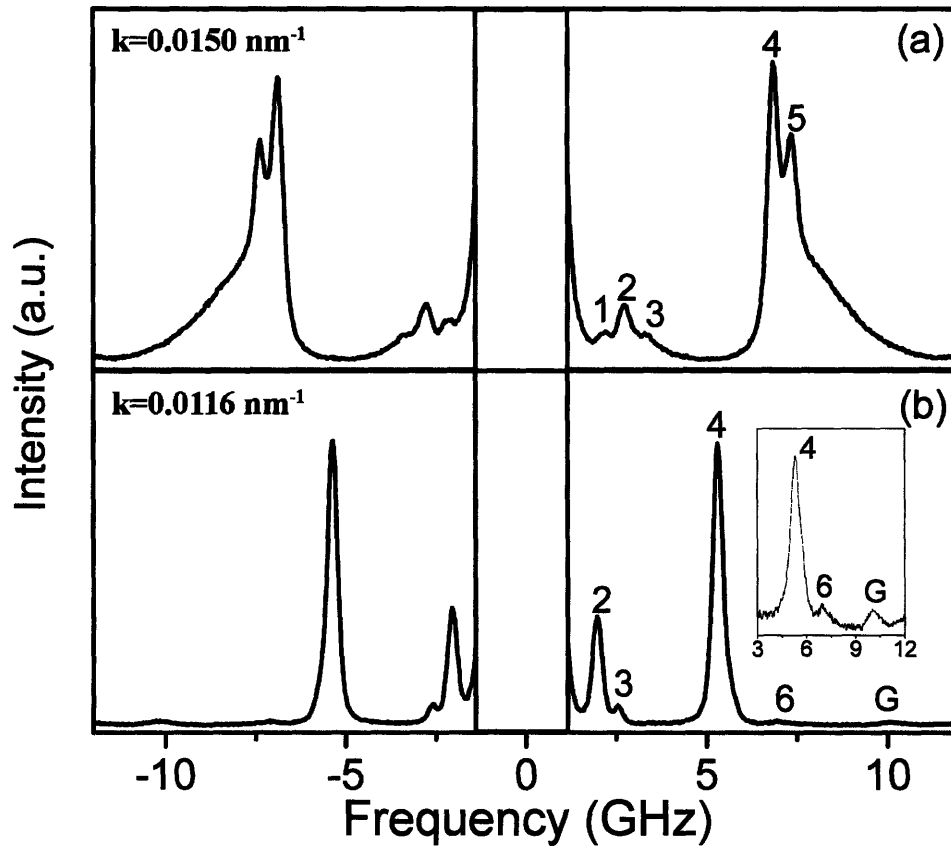


Figure 3.3. Typical BLS spectra of the PMMA/PET multilayer film at two different values of the phonon wave vector k at room temperature. The numbers denote the distinct modes discussed in the text. For clarity, the central Rayleigh line is not shown. The inset plot emphasizes the weak mode (6) by choosing a logarithmic intensity scale. The small feature G is the interferometer ghost of the strong mode (4).

At $k = 0.0116 \text{ nm}^{-1}$ (fig. 3.3 (b)), three distinct Brillouin doublets (2-4) are observed, with mode (4) being the most intense. At higher frequencies, two additional spectral features (mode (6) and G) can be identified. While barely discernible in the linear intensity scale, their existence is clearly visualized by plotting the intensity logarithmically, as shown in the inset of fig. 3.3 (b). The faint peak marked as G is identified as the ghost of the strong mode (4) due to higher order interference effects in the tandem Fabry-Perot interferometer. At higher k values (fig. 3.3 (a)) two other modes are resolved: the weak low-frequency mode (1) and the high frequency mode (5) with the

intensity comparable to that of mode (4). Moreover, an additional shoulder-like spectral feature appears on the high-frequency side of mode (5). Note that this shoulderlike spectral feature should not be confused with the ghost mode, fig. 3.3 (b).

Further insight into the physical origin of these modes can be gained by examining the dispersion relation, which contains important information about wave propagation by displaying the phonon frequency f experimentally determined as a function of k . To obtain these frequencies f_i ($i = 1-6$), the BLS spectra were fitted with a superposition of up to six Lorentzian line shapes shifted to the observed Brillouin peak positions plus one central line to account for the Rayleigh peak. Figure 3.4 illustrates the dispersion relation for the in-plane phonon propagation in our multilayer polymer system. Clearly, six modes can be identified and labeled in accordance with the six numbered peaks in fig. 3.3. At low k values, due to the proximity of their velocities not all six modes are resolved as shown in fig. 3.3 (b), where merely four modes appear (2-4 and 6). Their identification is based only on the dispersion relation (fig. 3.4). These observations are strikingly different from what would be expected if the film (with total thickness of $\sim 40 \mu\text{m}$) behaved as a mechanically homogeneous isotropic medium, where only two bulk modes (longitudinal and transverse) are anticipated.

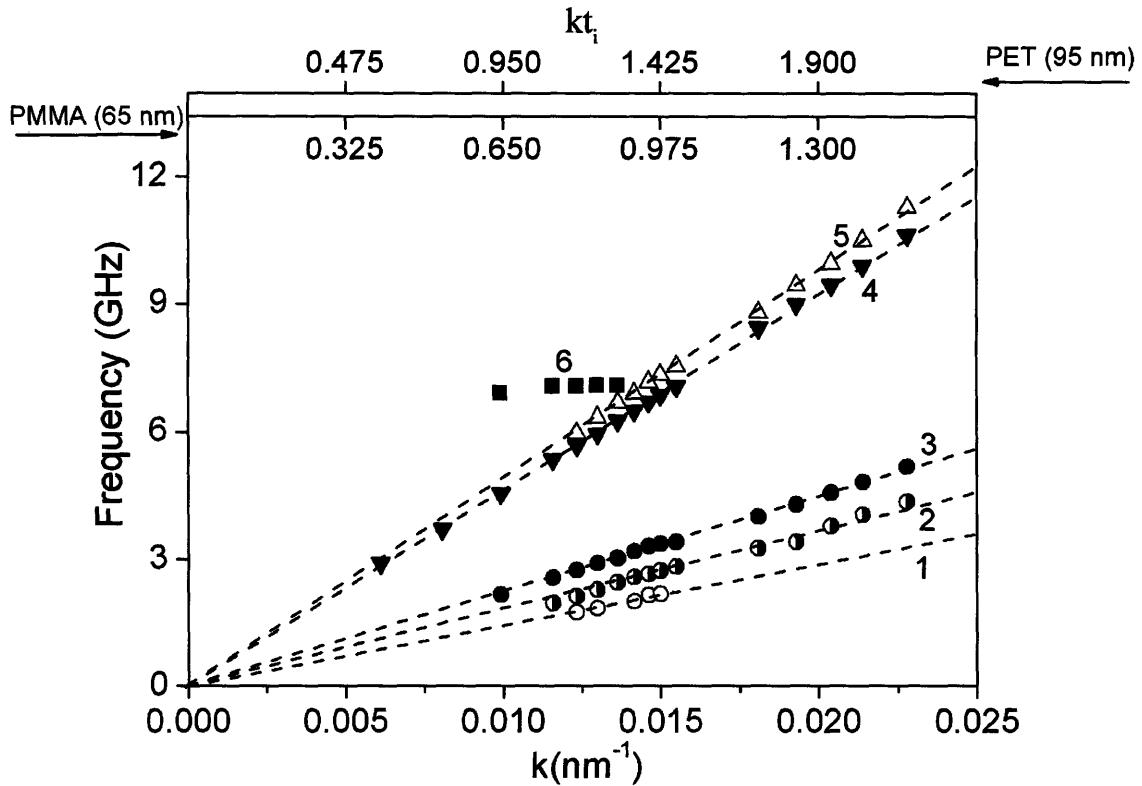


Figure 3.4. The experimental phonon dispersion relation of the multilayer birefringent polymer film. The dashed lines are the linear fits of the five observed propagation modes (1-5) with the linear dependence between the frequency and the wave vector; the frequency of mode (6) is insensitive to k variations. The upper abscissas show the corresponding kt_i values for the two constituent layer thicknesses t_i .

These experimental findings unambiguously suggest the explicit contribution of the individual constituent layers to the elastic excitations of this multilayer film. The result is in clear distinction from the earlier Brillouin study by Forrest *et al.* [61], where the dispersion relation of the PS/PI multilayer film was well described by an effective medium approach even though the mechanical contrast between the glassy PS and rubbery PI is large at room temperature.

3.3.4 FEA modeling of the phonon dispersion relation

To provide an interpretation for the observed in-plane propagation modes, we compute the theoretical phonon dispersion relation using finite element analysis (FEA). A two-dimensional (2D) eigenvalue model was created and solved using the COMSOL MULTIPHYSICS 3.3 FEA package based on the linear elastic plain-strain approximation. Since the film is periodic along the z direction, it is sufficient to model a single unit cell consisting of one PMMA and one PET layer and use Bloch boundary conditions

$$\vec{u}(x,0) = \vec{u}(x,a)\exp(ik_z a) \quad (3.1)$$

for the boundaries parallel to the x -axis. Here k_z is the z component of the phonon wave vector and a is the lattice constant. The film is considered homogeneous and infinite (the sample size is much larger than the phonon wavelength) along the x and y directions and the phonon wave vector is taken without loss of generality to be parallel to the x axis. Thus, we look for the wave equation solution in the form

$$\vec{u}(x,z) = \vec{u}(z)\exp(ik_x x), \quad (3.2)$$

which leads to the second boundary condition,

$$\vec{u}(0,z) = \vec{u}(l,z)\exp(ik_x l) \quad (3.3)$$

for the cell boundaries parallel to the z -axis. Here l is a length of the modeling domain along the x direction. This finite length of the modeling domain along the x axis l is artificially introduced into the model in order to employ FEA, since it cannot be used over an infinite domain. The solution, of course independent of the actual value of l , is used in the further data analysis. The model meshing and solver accuracy were previously validated by computing the phonon dispersion relations for a homogeneous material and

for 2D hexagonal phononic crystals and comparing the results with the analytical solutions (homogeneous material) and independent numerical computations (2D phononic crystals) [65]. In both cases an excellent match was observed.

The amorphous PMMA layer is modeled as an isotropic medium with Young's modulus $E_{PMMA}=6.26$ GPa, Poisson ratio $\nu_{PMMA}=0.341$, and density $\rho_{PMMA}=1.2$ g/m³. These values for elastic constants are based on the independent measurements of the speed of hypersound in pure PMMA films. On the other hand, the PET layer, due to the crystallization ability of PET, has to be taken as anisotropic (uniaxial). Its elastic constants depend on the degree of anisotropy, which is in turn determined by the history of the sample processing. As a result, it is very difficult to prepare pure PET films with the same elastic constants as in our sample for hypersound velocity measurements. For this reason, we were unable to determine elastic constants of anisotropic PET layers independently and instead used them as fitting parameters to ensure the best match between experimental and theoretical dispersion relation. The rich features of the experimental and theoretical dispersion relation allow identification of a unique combination of elastic constants, which provides a good agreement between the theory and the experiment. In particular, we found that the transverse sound velocity was determined almost entirely by shear modulus G_{xz} ; the longitudinal sound velocity – mainly by Young's moduli E_x and E_z and Poisson ratios ν_{xy} and ν_{xz} ; while the position of the q-independent mode was a function of shear modulus G_{xz} and Young's moduli E_x and E_z . Accordingly, the PET layer was modeled as a transverse isotropic medium with $E_{x_PET}=E_{y_PET}= 6$ GPa, $E_{z_PET}=4$ GPa, $\nu_{xy_PET}=0.40$, $\nu_{xz_PET}=0.48$, $G_{xz_PET}=2.2$ GPa,

$\rho_{PET}=1.38 \text{ g/m}^3$; G_{xz_PET} is the shear modulus in the xz plane. These values are consistent with previous studies of elastic constants of anisotropic PET [66-68].

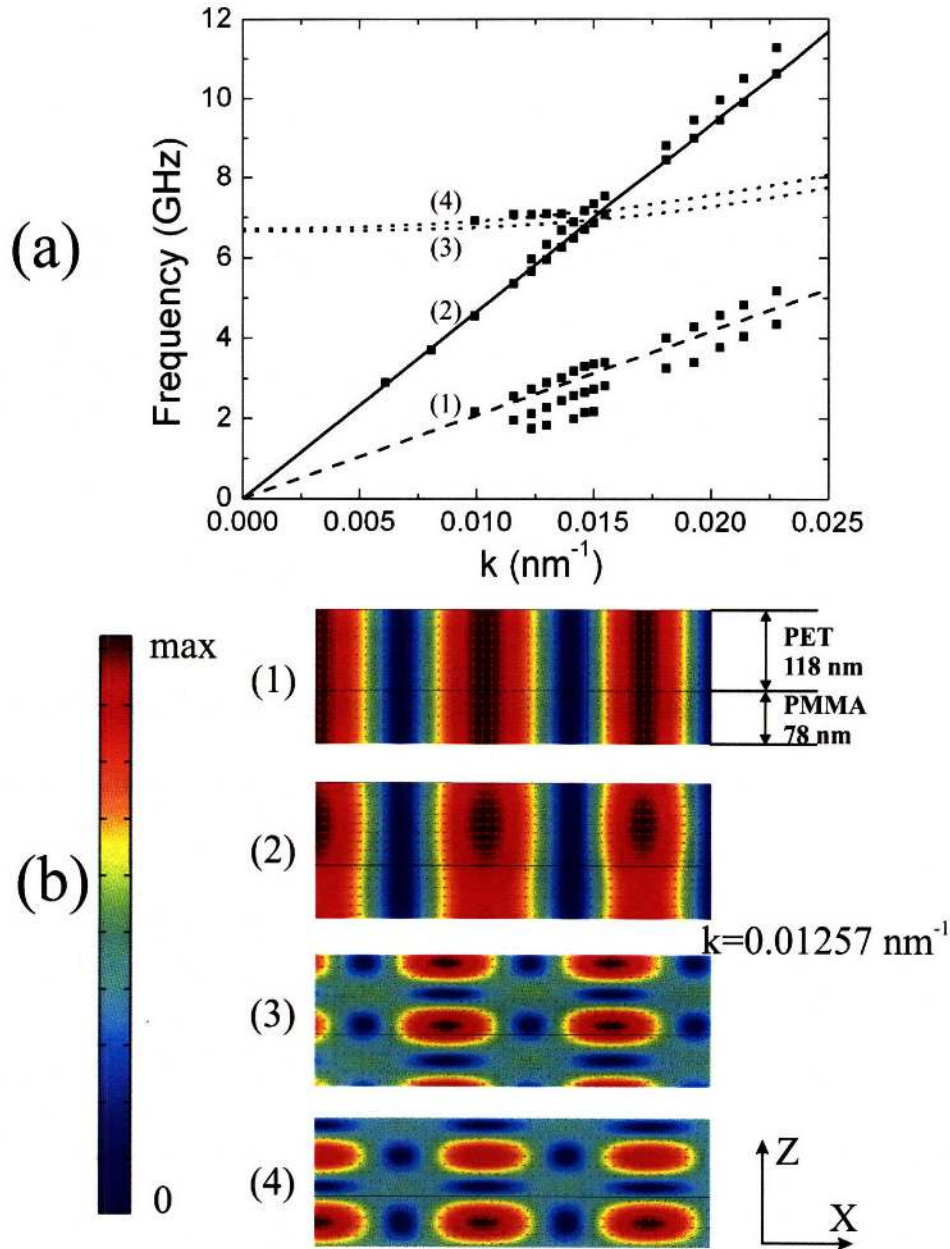


Figure 3.5. (a): The theoretical phonon dispersion relation and the experimental data for the in-plane elastic wave propagation in the multilayer polymer film: dashed line – transverse mode (1), solid line – longitudinal mode (2), dotted lines – mixed modes (3,4), black rectangles – experimental data; **(b):** elastic displacement fields for modes (1-4) computed at $k = 0.01257 \text{ nm}^{-1}$.

The theoretical phonon dispersion relation is shown in figure 3.5 (a). For the ease of comparison, experimental data are also plotted on the same graph (black rectangles). Four modes are expected according to the model prediction: a quasi transverse (QT) mode (dashed lines), a quasi longitudinal (QL) mode (solid lines), and two closely spaced high-frequency k -independent guided modes (dotted lines). The details of their displacement fields at $k = 0.01257 \text{ nm}^{-1}$ are shown in figs. 3.5 (b-e). Note that for both QL (fig. 3.5 (c)) and QT (fig. 3.5 (b)) waves the regions of high deformation are not confined to any individual layer, but rather are spread such that their displacement vectors are only weakly dependent on z , especially for the transverse wave. In contrast, for the high-frequency k -independent modes there are two regions of high deformation with the displacement vectors antiparallel to each other, as shown in fig. 3.5 (d, e). These modes appear as a result of periodicity in the film, and their frequency depends on the film lattice constant. Interestingly, the regions of high displacement are now localized within individual layers.

The positions of all modes are in good quantitative agreement with the experimental data. However, the model does not predict the splitting of the transverse and longitudinal lines into three and two components, respectively, as observed experimentally. It is well-known that optical birefringence or diffraction [69] may lead to the splitting of Brillouin lines due to the possible generation of light beams propagating in directions other than the main beam. However, for the present experiment, these possibilities can be safely ruled out. For $\Delta n = 0.15$, the birefringence induced splitting (ordinary and extraordinary rays) would be an order of magnitude smaller than what we have observed and cannot be

resolved experimentally [41]. The small periodicity (compared to the laser wavelength) excludes optical diffraction interference, as confirmed by the failure of observing any abnormal optical beams in our experiment. Therefore, one must search for the cause of the additional modes within the framework of elastic wave propagation.

There are two relevant length parameters in our problem: the lattice constant $a = t_{PMMA} + t_{PET}$ and the phonon wavelength λ . Their ratio $\zeta = \frac{a}{\lambda}$ will determine how the propagating waves interact with the layered medium, i.e., if they experience it as a homogeneous medium or if they are sensitive to the properties of the individual layers. The larger ζ , the more we can expect waves to be localized within individual layers. In the extreme case when $\zeta \gg 1$, waves propagating in each layer become completely insensitive to the presence of the other layers. Figure 3.5 (b-e) shows a weak z dependence for the QT and QL modes, but not for the higher frequency k -independent modes. This behavior corresponds to the regime where phonon propagation is just starting to be influenced by the multilayer structure of the film. It is helpful then to examine now how the features of the wave propagation change upon further increase in ζ . Figure 3.6 shows the theoretical dispersion relation for the QT (dashed lines) and QL (solid lines) modes as well as the extrapolation of the experimental data (dotted lines) based on the sound velocities of the experimental modes (2)-(5) for k in the range from 0.05 to 0.07 nm⁻¹. Interestingly, the existence of three QT and three QL modes is now predicted by the model. The phase velocities of these modes match the experimental values quite well. Unlike the case of the lower k values, the displacements fields of these modes show strong z dependence and are contained either in the PET or in the PMMA

layers. This result suggests that the five linear dispersion modes (1-5) observed experimentally may come from the localized QL and QT phonons propagating within the polymer individual layers. It is not entirely clear why the theory predicts the line splitting for somewhat higher values of k than observed experimentally. Imperfections at interfaces, such as interfacial roughness and strain fields, as well as a certain degree of uncertainty about elastic constants of the anisotropic PET layers may be responsible for this difference.

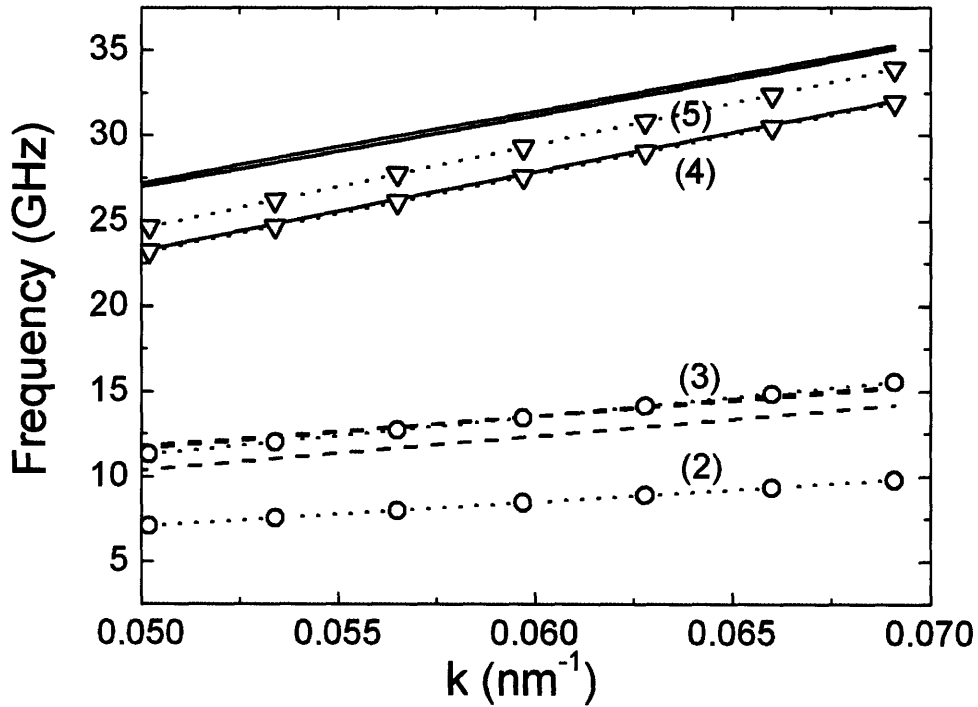


Figure 3.6. The phonon dispersion relation of the PMMA/PET multilayer film for $k = 0.50 - 0.68 \text{ nm}^{-1}$: solid lines – theoretical QL modes, dashed lines – theoretical QT modes, dotted lines with circles and triangles – extrapolation of experimental data for QT modes (2,3) and QL modes (4-5), respectively.

3.3.5 Temperature dependence of sound velocities

In the previous section, some of the observed acoustic-like phonons were associated with the individual layers. Since PET and PMMA possess different glass transition temperatures T_g (352 K for PET and 378 K for PMMA), the variation of the phase velocities of the observed phonon modes with temperature is anticipated to display the characteristic kink at T_g , which should occur at distinctly different temperatures for the two polymers. This would be a direct confirmation of the association of these modes to the individual polymer layers.

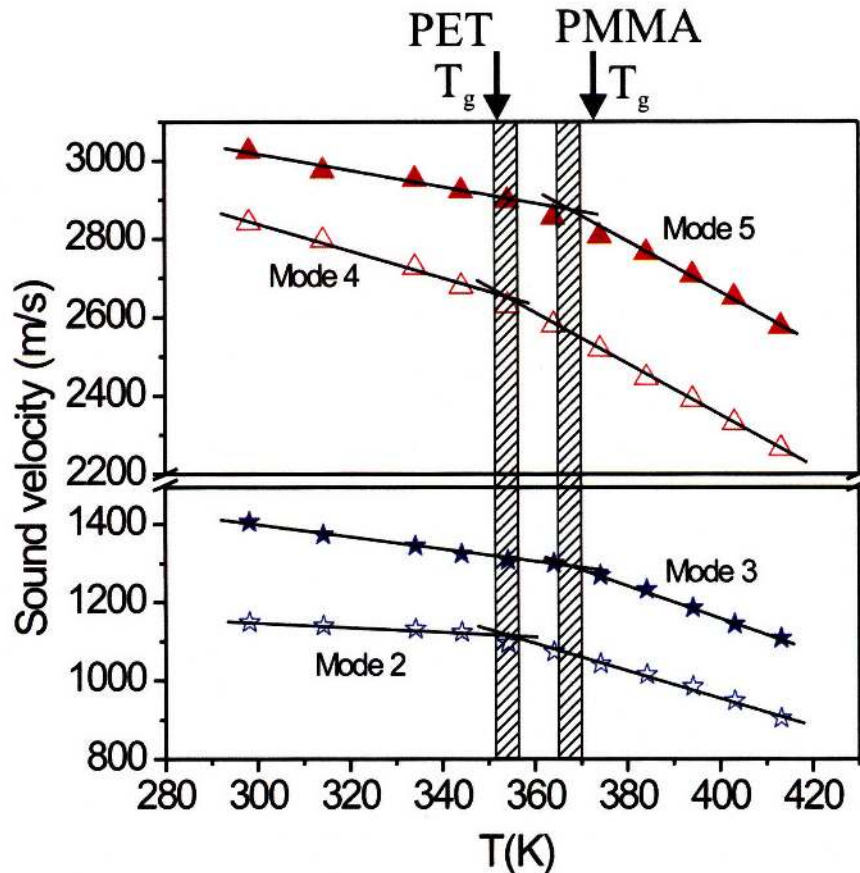


Figure 3.7. The variation of the phase velocities of the four main modes in the PMMA/PET multilayer film as a function of temperature. The numbers correspond to the mode numbers in fig. 3.4. The vertical shaded regions denote the region of the respective glass transition temperatures of the two polymers. Solid lines represent the least square fit to the experimental data before and after the glass transition, data points in the vicinity of T_g were excluded from the fitting.

The phase velocities of the four linear dispersion modes ((2)-(5)) are plotted as a function of T in figure 3.7. The harder PMMA layer exhibits a higher T_g (~100 °C) than the softer PET layer (~80 °C). It is evident from fig. 3.7 that modes (2) and (4) should be associated with PET layers and modes (3) and (5) with PMMA layers since they exhibit the same values of T_g , respectively. These results are in accordance with our attempt to associate these modes with the two types of individual layers. The sound velocity of the weak, low-frequency mode (1) shows a very small variation with T that renders the identification of the kink feature ambiguous, and it is therefore excluded from fig. 3.7.

The dependence of phase velocities of these modes at temperatures above and below T_g can be well described by the linear relation

$$c(T) = c(0)(1 - \alpha_T T) \quad (3.4)$$

with $c(0)$ being the extrapolated velocity in the particular polymer at 0 K, and α_T is the proportionality coefficient, which describes how rapidly the sound velocity of a particular mode changes with temperature. Since the longitudinal sound velocity is related to the

adiabatic compressibility $\beta_s = \frac{1}{V} \left(\frac{\partial V}{\partial P} \right)_s$ of the material through the equation

$$c_L = \sqrt{\frac{\beta_s}{\rho}} \quad (3.5)$$

α_T of the two longitudinally featured modes (4) and (5) in different layers characterizes the temperature dependence of β_s of the two component materials, while α_T of the transverse modes (2) and (3) describes the temperature dependence of the adiabatic shear modulus G_s . The values of α_T for modes (2-5) are given in table 3.2 for the glassy ($T < T_g$) and the rubbery ($T > T_g$) regimes. These values were obtained by performing a linear fit of

experimental sound velocities before and after the glass transition. Data that are in the vicinity of T_g were excluded from the fit. BLS measures the adiabatic compressibility of the system and could, in principle, be utilized to probe the T_g at different layer thicknesses in this sandwiched multilayer arrangement. For the QT mode (2) and (3) in the PET and PMMA layers, respectively, the coefficient α_T (table 1) is somewhat larger than those of the QL modes in the rubbery regime. This is expected, since the shear modulus should eventually decrease to zero in the liquid state in contrast to the tension/compression modulus. In the glassy regime, these material properties reflect different deformation of the matter and a prediction on the relative magnitude of α_T for the two moduli is not possible.

Table 3.2. Sound velocities and their temperature coefficients α_T of the various phonon modes of the PET/PMMA multilayer film.

Mode	1	2	3	4	5
Room temperature sound velocity (m/s)	890±20	1175±23	1415±25	2905±30	3085±30
$\alpha_T(T < T_g) \cdot 10^4$ (K ⁻¹)	—	3.9±0.2	8.6±0.4	9.0±0.4	5.8±0.3
$\alpha_T(T > T_g) \cdot 10^3$ (K ⁻¹)	—	1.46±0.05	1.50±0.06	1.3±0.03	1.23±0.03

3.3.6 *Summary*

In this section the in-plane phonon propagation in a 1D periodic anisotropic multilayer PET/PMMA film with the lattice constant $a = 196 \text{ nm}$ was analyzed. BLS was used to measure the experimental phonon dispersion relation at GHz frequencies. The dispersion relation is found to be sensitive to the structure and mechanical properties of individual layers. Thus, knowledge of the phonon dispersion relation provides valuable information about elastic constants of individual layers in nanoscale multilayer assemblies. We

observe five linear-dispersion propagation modes with constant phase velocities and an additional mode with frequency that is nearly independent of the wave vector. FEA is employed to provide the interpretation of the observed propagation modes. While the fit between the FEA results and the experimental phonon dispersion is generally good, the model predicts splitting of longitudinal and transverse lines into several components at substantially higher thickness-to-wavelength ratio ζ than observed experimentally. The possible reasons for this difference are discussed in the next section, where the dispersion relation of isotropic PC/PMMA systems is studied as a function of their lattice constant and composition. Temperature-dependent sound velocity measurements suggest that rich features of the phonon dispersion of the PET/PMMA multilayer mirror are related to phonons propagating within individual layers and not throughout multiple layers, where the film's properties would correspond to an effective homogeneous medium as confirmed by two distinct glass transition temperatures that correspond to T_g of the PET and PMMA layers, respectively.

3.4 Evolution of phonon dispersion of 1D periodic isotropic PC/PMMA self-supporting films with a lattice constant and composition [70]

3.4.1 Advantages of PC/PMMA systems

In the previous section the in-plane phonon propagation in the giant birefringence PET/PMMA optical mirror was analyzed using Brillouin light scattering and finite element analysis. The most exciting result is the observation of a rich and complex phonon dispersion relation, which was explained by the influence of individual layers on the propagation of GHz phonons in the film. As a result, the elastic constants of the

periodic anisotropic nanolayers were estimated from the phonon dispersion relation. Furthermore, temperature-dependent sound velocity measurements of localized propagating modes were used to measure the glass transition temperatures of individual layers in a periodic multilayer assembly.

Despite these interesting results, the PET/PMMA optical mirror is not the most suitable system for a systematic study of the in-plane phonon propagation in 1D crystals. The anisotropy in the PET layers makes data acquisition and analysis unnecessarily complicated and ambiguous. More importantly, 3M does not disclose information about the detail of its manufacturing process making independent determination of the anisotropic elastic constants of the constitutive polymers nearly impossible. Finally, only one film with a fixed lattice constant and composition was available for the investigation.

In this section we discuss phononic properties of periodic self-supporting multilayer PC/PMMA films. Several samples with lattice constants ranging from 25 nm to 800 nm and compositions from pure components to equal volume fractions have been studied. Importantly, the polymeric materials are isotropic allowing clear distinction between light scattered by longitudinal phonons (detected in the VV geometry) and transverse phonons (detected in the VH geometry), see section 2.3.1 for more information on polarization of light scattered in BLS experiments. Finally, elastic and optical properties of these polymers are well known and thus FEA computations can be performed without need for any adjustable or fitting parameters.

3.4.2 Sample architecture and morphology

The structural parameters of the PC/PMMA multilayer films are listed in table 3.3. Two sets of samples have been investigated: (1) samples with a fixed lattice constant $a = 782 \text{ nm}$, but different compositions; and (2) samples with a fixed composition of $\phi = 50\%$ PC volume fraction, but different lattice constants. The films were fabricated using coextrusion by the group of Prof. Eric Baer in the Department of Macromolecular Science at Case Western Reserve University. The micromechanical behavior of these films at large strains has been investigated by Baer with aim to improve adhesion and toughness of polymer multilayers [63,64].

Table 3.3. Structural parameters of PC/PMMA multilayer films.

Number of layers	PC composition (%)	t_{PC} (nm)	t_{PMMA} (nm)
Fixed lattice constant, different compositions			
128	80±5	626±100	156±100
128	65±5	508±100	274±100
128	50±5	391±100	391±100
128	35±5	274±100	508±100
128	20±5	156±100	626±100
Fixed composition, different lattice constants			
128	50±5	391±100	391±100
256	50±5	195±59	195±50
512	50±5	98±25	98±25
1024	50±5	49±12	49±12
2048	50±5	25±6	25±6
4098	50±5	12±3	12±3

TEM micrographs illustrating morphology of samples with $a = 782 \text{ nm}$ and 80%, 50% and 20% PC volume fraction; and samples with 50% PC volume fraction and 98 nm, 50 nm and 25 nm lattice constants are shown in figs. 3.8 (a), (b), and (c); and (d), (e) and (f), respectively. The structure of the PC/PMMA films is less perfect as that of the

PET/PMMA optical mirror. There is a substantial variation in thicknesses of individual layers in all samples. At the same time the layers are generally continuous, flat, and parallel to each other. Interfaces are smooth and sharp with no significant intermixing observed.

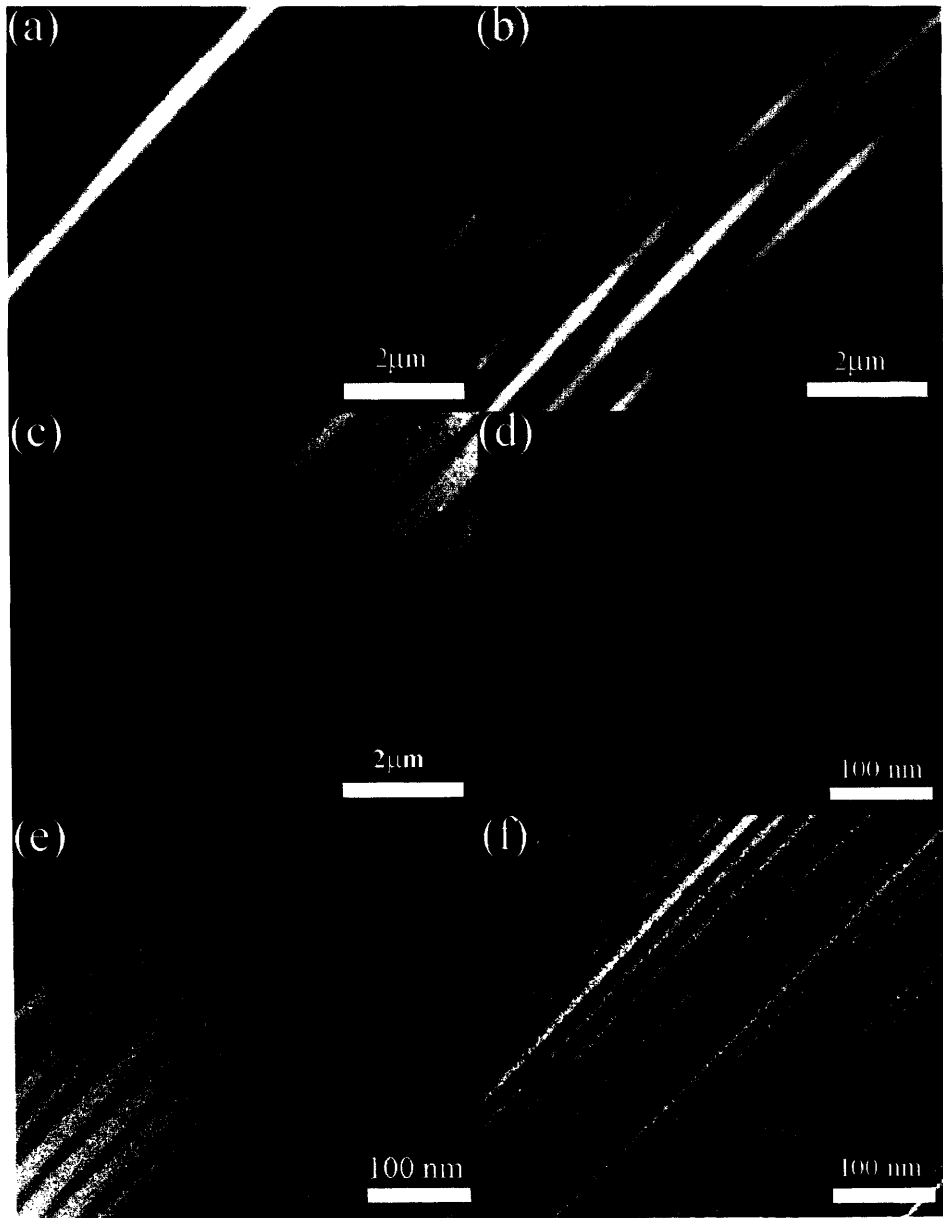


Figure 3.8. TEM images of the PC/PMMA films: (a), (b) and (c) – samples with $a = 782 \text{ nm}$ and 80%, 50% and 20% PC volume fraction, respectively; (d), (e) and (f) – samples with 50% PC volume fraction and 98 nm, 50 nm and 25 nm lattice constants, respectively.

3.4.3 Experimental phonon dispersion relation of PC/PMMA films

BLS spectra taken using the VV transmission scattering geometry at $k = 0.0181 \text{ nm}^{-1}$ for five periodic multilayer films with $\phi = 50\%$ and various lattice constants are shown in fig. 3.9. Interestingly, BLS spectra of the films with lattice constants up to 195 nm resemble that of a homogeneous medium with a single peak that corresponds to scattering from longitudinal phonons.

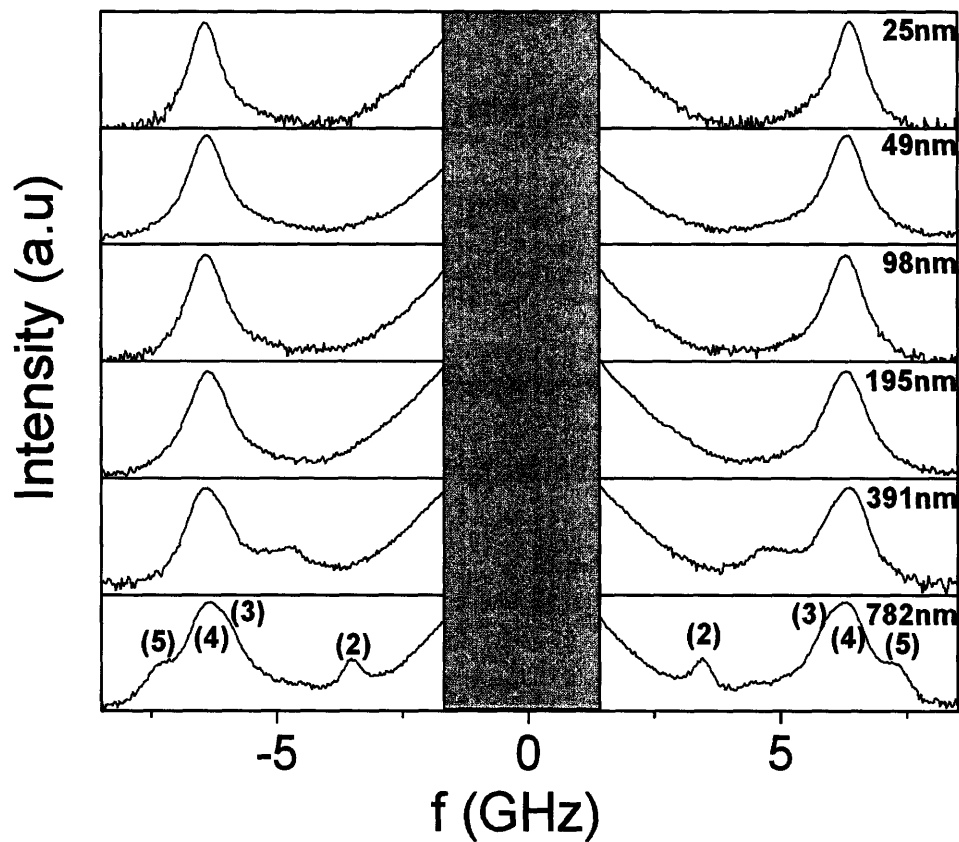


Figure 3.9. BLS spectra taken with the VV transmission scattering geometry at $k = 0.0181 \text{ nm}^{-1}$ for five periodic multilayer films with 50% PC volume fraction and lattice constants ranging from 25 nm to 782 nm.

The complexity of the BLS spectra increases gradually with the increase in the lattice constant, such that the VV spectra of films with 391 nm and 782 nm display two and four

distinct modes (labeled (2)-(4) in 782 nm spectrum of fig. 3.9), respectively. The intensities of these modes are notably different suggesting large differences in the microscopic details of their displacement fields. The two relevant length parameters, $a = t_{PC} + t_{PMMA}$ and the phonon wavelength $\lambda = 2\pi/k$, determine how the propagating elastic waves interact with the layered medium. For $a/\lambda < 1$, the medium appears homogeneous, since long wavelength material displacements propagate with a sound phase velocity c_{eff} in a two component effective medium. In fact, the experimental value $c_{eff} = \omega/k$ at low k is well captured from the elastic properties of the individual components and the film composition, ϕ using the Wood's law:

$$\left(\rho c_{eff}^2\right)_{eff}^{-1} = \phi \left(\rho_{PC} c_{PC}^2\right)^{-1} + (1 - \phi) \left(\rho_{PMMA} c_{PMMA}^2\right)^{-1}. \quad (3.6)$$

The sound velocity of the transverse phonons with displacements perpendicular to their propagation direction can be obtained from the VH BLS spectra at low a/λ values, where we can expect effective medium behavior.

3.4.4 Theoretical phonon dispersion relation of PC/PMMA films

Finite element analysis was used to compute phononic dispersion relations and provide interpretation of the observed propagation modes. The detailed description of the model parameters and boundary conditions is provided in section 3.3. The model assumes perfectly bonded, ideally flat layers with uniform thickness, no roughness and defects, no spatial variations in elastic properties and zero interface thickness. The densities and elastic constants of the PC and PMMA layers are listed in table 3.1. Figure 3.10 shows the comparison between the theoretical dispersion relation and the experimental results.

Quasilongitudinal, quasitransverse and mixed modes are shown as solid, dashed and dotted lines, respectively. (Note that QL modes scatter light in VV geometry, QT modes – in VH geometry, while scattering from mixed modes is generally very weak and difficult to detect experimentally).

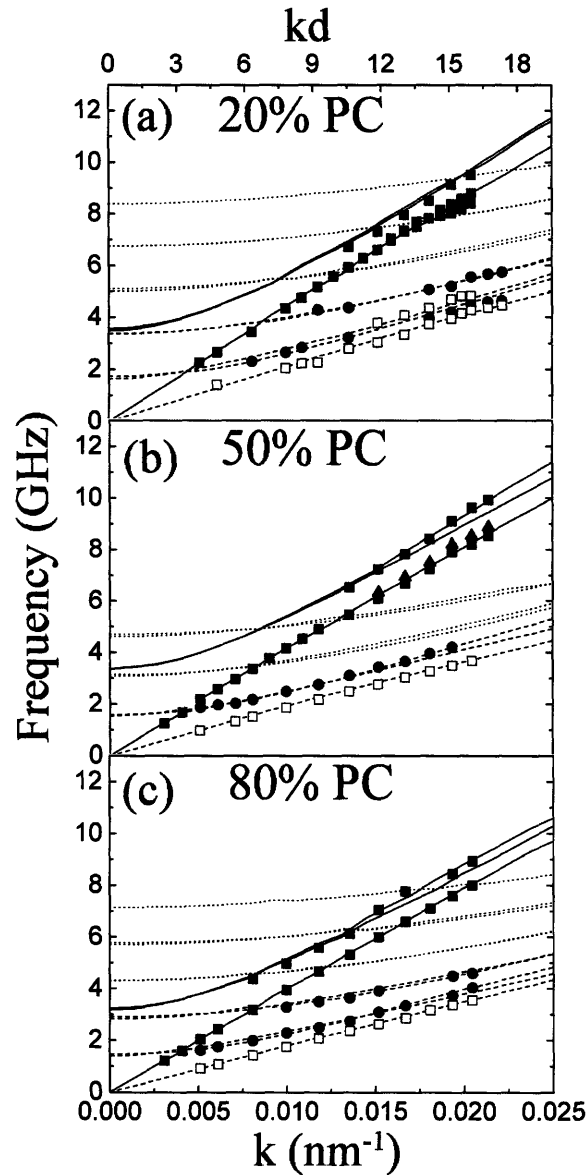


Figure 3.10. The theoretical and experimental phonon dispersion relations of the PC/PMMA multilayer films with $a = 782 \text{ nm}$ and 20% (a), 50% (b) and 80% (c) PC volume fractions. Open and solid symbols refer to the experimental modes measured in the VH and VV BLS geometries, respectively. The theoretical dispersion relations for the QL, QT and mixed modes are plotted using solid, dashed and dotted lines, respectively.

There is a very good agreement between the theoretical and the experimental results for all compositions. The sound velocities of the two acoustic modes c_{L_eff} and c_{t_eff} are independent of the layer thickness between 780 nm and 25nm at constant composition. The appearance of the additional non acoustic modes (2-3) and (5) is predicted by the theory. Importantly, computations allow us to observe the details of their displacement fields thereby providing interpretation of the nature of these modes.

Displacement fields corresponding to the QT and QL modes for $k = 0.025 \text{ nm}^{-1}$ in the 782 nm film with 50% PC fraction are shown in fig. 3.11, ordered from low to high frequency. There are three distinct QT and three QL modes predicted for this sample, although only two QT modes are resolved experimentally, possibly due to weak scattering intensity, close proximity of the QT modes and/or structural imperfections of the films. Note that, while these modes propagate with essentially the same phase velocities (fig. 3.10), their displacements are localized primarily within the individual PC or PMMA layers. When the phonon wave vector approaches zero, these modes represent localized, non propagating eigenvibrations of the periodic bilayers with zero group velocities and frequencies given by

$$f = \lim_{k \rightarrow 0} \left(\frac{c}{2\pi} (\vec{k} + \vec{G}) \right) = \frac{c}{d}, \quad (3.7)$$

where c is either the longitudinal (for (5)) or transverse (for (2,3)) effective sound velocity. Mode (3) represents the second transverse harmonic vibration mode corresponding to $|\vec{G}| = 2 \frac{2\pi}{d}$. For the larger values of k , the displacement fields of these

modes evolve into layer guided phonons (fig. 3.11) propagating with group velocities that approach the phase velocities of the medium as seen from the dispersion relation in fig. 3.10.

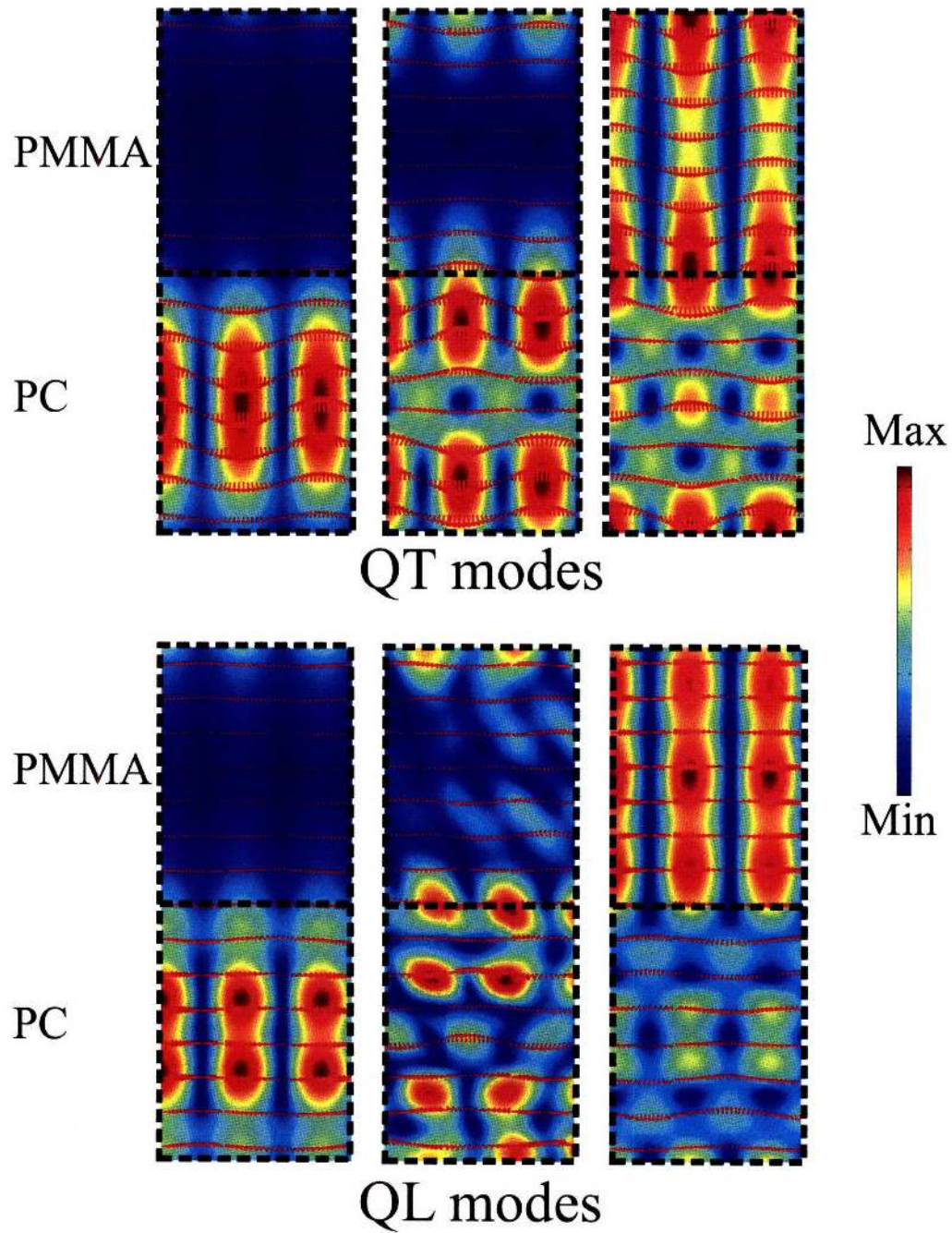


Figure 3.11. Details of the displacement fields for the QT and QL modes computed for the film with $a = 782 \text{ nm}$ and 50% PC fraction at $k = 0.025 \text{ nm}^{-1}$.

3.4.5 Temperature dependence of sound velocities in PC/PMMA films

The biased spatial distribution of the displacement fields for different modes is manifested in their T_g values. The variation of the phase velocities of these modes with temperature is anticipated to display the characteristic kink at the temperature that corresponds to the T_g of their propagation medium. Thus, the temperature behavior of sound velocities of various phonon modes can be used in combination with the theoretical modeling to provide interpretation on the nature of the observed propagation modes.

Figure 3.12 shows the temperature variations of sound velocities of various phonon modes for the samples with the volume fraction $\phi = 50\%$ and the lattice constant $a = 782 \text{ nm}$ (a) and $a = 25 \text{ nm}$ (b). The sample with $a = 25 \text{ nm}$ displays a single T_g of $122 \text{ }^\circ\text{C}$, which is intermediate between the glass transition temperatures of the PMMA ($105 \text{ }^\circ\text{C}$) and PC ($140 \text{ }^\circ\text{C}$) layers. Thus, phonons propagating in the 25 nm lattice constant film do not resolve the presence of individual polymer layers and display a homogeneous medium-like behavior. In contrast, there are three distinct glass transition temperatures for phonons propagating in the film with $a = 782 \text{ nm}$. Modes (1) and (3) have T_g of $\sim 135 \text{ }^\circ\text{C}$, which is very similar to the glass transition temperature of PC; mode (5) has T_g of $\sim 105 \text{ }^\circ\text{C}$, which is essentially the glass transition temperature of PMMA; while T_g of mode (4) is $\sim 122 \text{ }^\circ\text{C}$. Therefore, modes (1) and (3) must propagate primarily in the PC layers; mode (5) – primarily in the PMMA layers; and mode (4) – in both PC and PMMA layers. This conclusion agrees very well with the theoretical displacement fields shown in

fig. 3.11, which suggest that the lowest frequency transverse and longitudinal modes should propagate in the PC layers, the highest frequency longitudinal mode should propagate in the PMMA layers, while the mid frequency longitudinal mode is not strongly localized. Note that the temperature-dependent measurements for mode (2) would require much longer accumulation time those for the other modes due to its low scattering intensity thus rendering the comparison less meaningful. For this reason the variation of the phase velocity of mode (2) with temperature is not included in fig. 3.12.

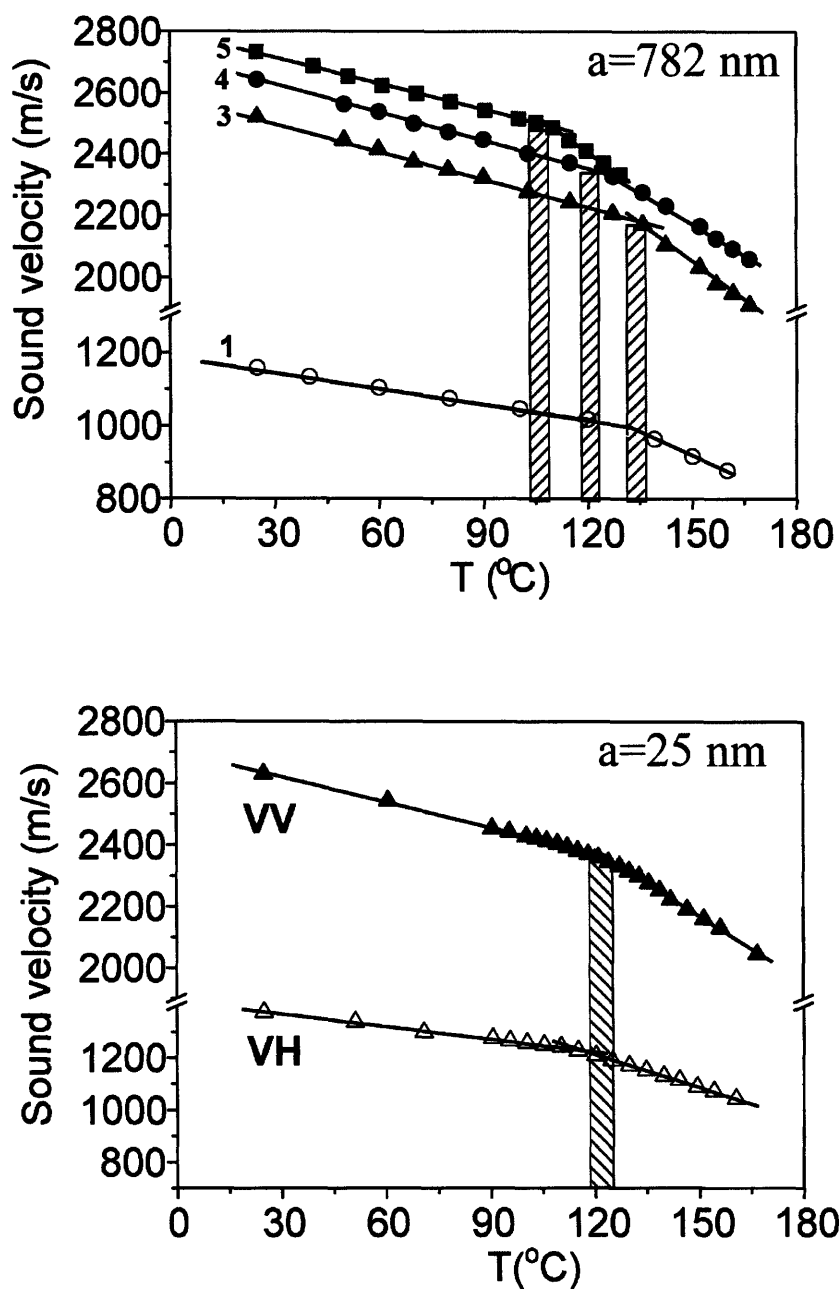


Figure 3.12. Temperature variation of the phonon phase velocities in the PMMA/PC films with $\phi = 50\%$ and lattice constants of 782 nm (a) and 25 nm (b). The vertical shaded regions denote the regions of the respective glass transition temperatures of the two polymers. Solid lines represent the least-square the experimental data before and after the glass transition; data points in the vicinity of T_g were excluded from fitting.

3.4.6 *Summary*

This section describes the evolution of the phonon dispersion relation for the in-plane propagation in periodic multilayer PC/PMMA films as a function of their lattice constants, compositions and temperature. A gradual increase in complexity from a simple two-mode dispersion characteristic of a homogeneous medium to a complex multimode dispersion of a periodic medium is observed with increase in the lattice constant. FEA is employed to compute the theoretical dispersion relations and displacement fields within respective layers. An excellent agreement with the experimental data for all compositions is achieved using no adjustable parameters. Examination of the details of the theoretical displacement fields suggest that the additional modes represent phonons propagating within individual layers. Finally, the temperature dependence of the sound velocities reveals the presence of three distinct glass transition temperatures in films with 782 nm lattice constant, but only a single effective medium glass transition temperature in films with 25 nm lattice constant $a/\lambda < 1$, in further support of the influence of the individual layers on the in-plane phonon propagation.

3.5 **Conclusions**

This chapter describes general features of elastic wave propagation in 1D phononic crystals. While relatively simple to fabricate and analyze, 1D systems exhibit a complex phonon dispersion relation with a number of unique characteristics. Thus, they constitute an excellent platform to gain a basic understanding of the phononic band gap phenomena. First, the normal propagation in 1D crystals with small and large mechanical contrast is

treated theoretically with example calculations based on the PC/PMMA and SiO₂/PMMA systems, respectively. In contrast to 1D photonic crystals, considerable mechanical contrast is required to open polarization independent band gaps in 1D solid/solid phononic crystals due to notable difference in sound velocities of the longitudinal and the transverse modes. Then, the in-plane phonon propagation in the anisotropic PET/PMMA and a set of isotropic PC/PMMA multilayer films is studied. The complex phonon dispersion relations are observed at large thickness-to-wavelength ratios. FEA computations and temperature dependence of sound velocities clearly demonstrate that the appearance of the additional modes is related to phonons propagating within the individual layers and not throughout the film as a homogeneous medium. Therefore, the phonon dispersion relation of these modes provides information about the structure and mechanical properties of the propagation medium for $a/\lambda > 1$. This conclusion has far-reaching practical implications allowing us to measure the elastic constants and glass transition temperatures of the individual polymer layers.

CHAPTER 4. PHONON DISPERSION RELATION OF 2D CRYSTALS FABRICATED USING INTERFERENCE LITHOGRAPHY [65]

4.1 Introduction

In this chapter the in-plane phononic properties of 2D hypersonic crystals fabricated with interference lithography are investigated. This study is different from the investigation of the 1D multilayer polymer films described in the previous chapter in several respects. First, in 2D crystals we expect to observe partial phononic band gaps along any direction in the crystal plane, as opposed to the multilayer films, where no band gaps exist for the in-plane propagation. The use of the transmission scattering geometry insures that the phonon wave vector k is parallel to the crystal plane allowing detailed experimental mapping of the phononic band diagram of 2D crystals. Moreover, since our samples are single crystalline, any direction within the Brillouin zone can be experimentally accessed by simply rotating the specimen.

Second, 2D crystals fabricated with interference lithography are solid/fluid structures consisting of air holes in epoxy matrix, unlike solid/solid polymer films. The huge mechanical contrast between epoxy (or any other solid) and air leads to the formation of complete 2D phononic band gaps for a window of volume fractions in both hexagonal and square phononic crystals [31]. At the same time, computations of the theoretical band diagrams for solid/fluid crystals are more complex than for solid/solid crystals. It was shown that the plane wave method fails to correctly predict phononic band diagrams of solid/fluid structures regardless of how many plane waves are used in the expansion [72-

74]. For this reason, other numerical methods, such as finite element analysis or multiple scattering theory, must be employed.

Finally, the experimental 2D crystals examined in this chapter are not self-supporting. Instead, they are fabricated as thin ($5 \mu\text{m}$) films on top of a thick (3 mm) glass substrate. It is important to consider the potential influence that the substrate may have on the wave propagating in the patterned film when designing experiments and interpreting their results. In particular the thickness-to-wavelength ratio of the film must be sufficiently large ($t/\lambda > 3$) to minimize leaking of the elastic waves into the substrate.

Two sets of samples have been investigated: (1) hexagonal crystals with the lattice constant $a = 1360 \text{ nm}$ and porosity $\phi = 4\%$ and $\phi = 39\%$; and (2) square crystals with the lattice constant $a = 750 \text{ nm}$ and porosity $\phi = 30\%$. Rich dispersion relation consisting of several higher order propagation bands was observed in the hexagonal crystals for phonons propagating along the $[110]$ direction. The theoretical band diagrams computed using finite element analysis are in excellent agreement with the experimental data. However, these crystals possess the lowest order phononic band gaps at roughly 700 MHz , which is below the detection limit of the Brillouin light scattering apparatus. For this reason no band gaps were observed experimentally. In contrast, the smaller lattice constant of the square crystals leads to the midgap frequencies of roughly 1.4 GHz , which is sufficient for the direct experimental observation of the gaps between the first and the second propagation bands.

4.2 Phononic dispersion relation of 2D hexagonal crystals

SEM images and a laser diffraction pattern of 2D hexagonal crystals fabricated using interference lithography are shown in figure 4.1.

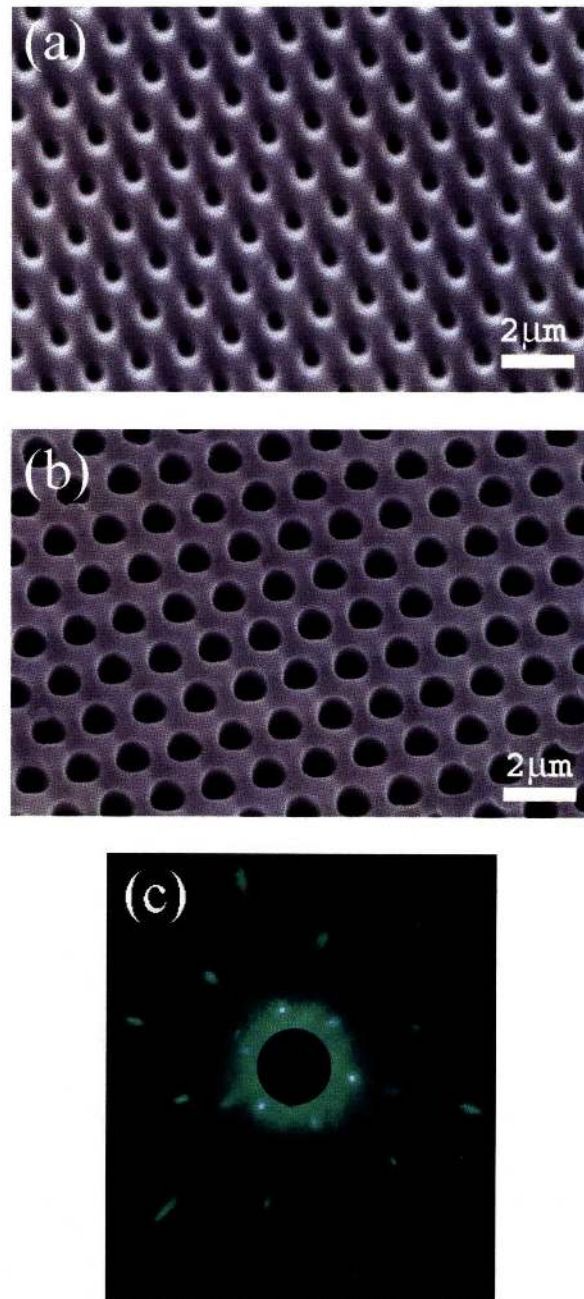


Figure 4.1. SEM images of interference lithography patterned samples with hexagonal symmetry for (a) 4% and (b) 39% air volume fraction; (c) 90° laser light diffraction pattern confirming single crystallinity of the samples.

The samples consist of hexagonal arrays of cylindrical holes in epoxy matrix. The epoxy layer is a 6 μm thick film on a glass substrate. The average sample radius is 2 mm. Two samples have been analyzed: s1 with a cylinder radius to lattice constant ratio of $r/a = 0.1$ (4% porosity), and s2 with $r/a = 0.33$ (39% porosity). The lattice constant for both samples is $a = 1360 \text{ nm}$. The normal incidence transmission light diffraction pattern (fig. 4.1 (c)) confirms the single crystal nature and hexagonal symmetry of the structures.

BLS is employed to measure the phonon dispersion relation of these structures. All measurements are done using the VV transmission scattering geometry, as described in section 2.3.2. A typical intensity profile consists of a very strong elastic Rayleigh peak at $f = 0 \text{ GHz}$ and a series of symmetric Brillouin doublets at $\pm f$ that correspond to Stokes and anti-Stokes scattering (fig. 4.2 (a)). The smallest detectable frequency shift is determined by the wings of the Rayleigh peak and by the intensity of the Brillouin doublet. In our case, it is roughly 1 GHz for the stronger glass substrate peaks and 1.5 GHz for the weaker epoxy film peaks.

To understand the effects of periodicity on the phonon propagation we first compare the spectrum of the s1 sample with that of the unpatterned photoresist film. Both spectra were taken at $k = 0.0051 \text{ nm}^{-1}$. Figures 4.2 (a) and 4.2 (b) show the VV scattered light intensity profiles $I = I(f)$ for the unpatterned film and s1, respectively. Two peaks are present in the spectrum of the unpatterned sample: a high intensity peak (1) at

$f = 4.74 \text{ GHz}$ coming from the glass substrate, and a less intense peak (2) at $f = 2.34 \text{ GHz}$ that corresponds to the longitudinal phonon of the polymer film.

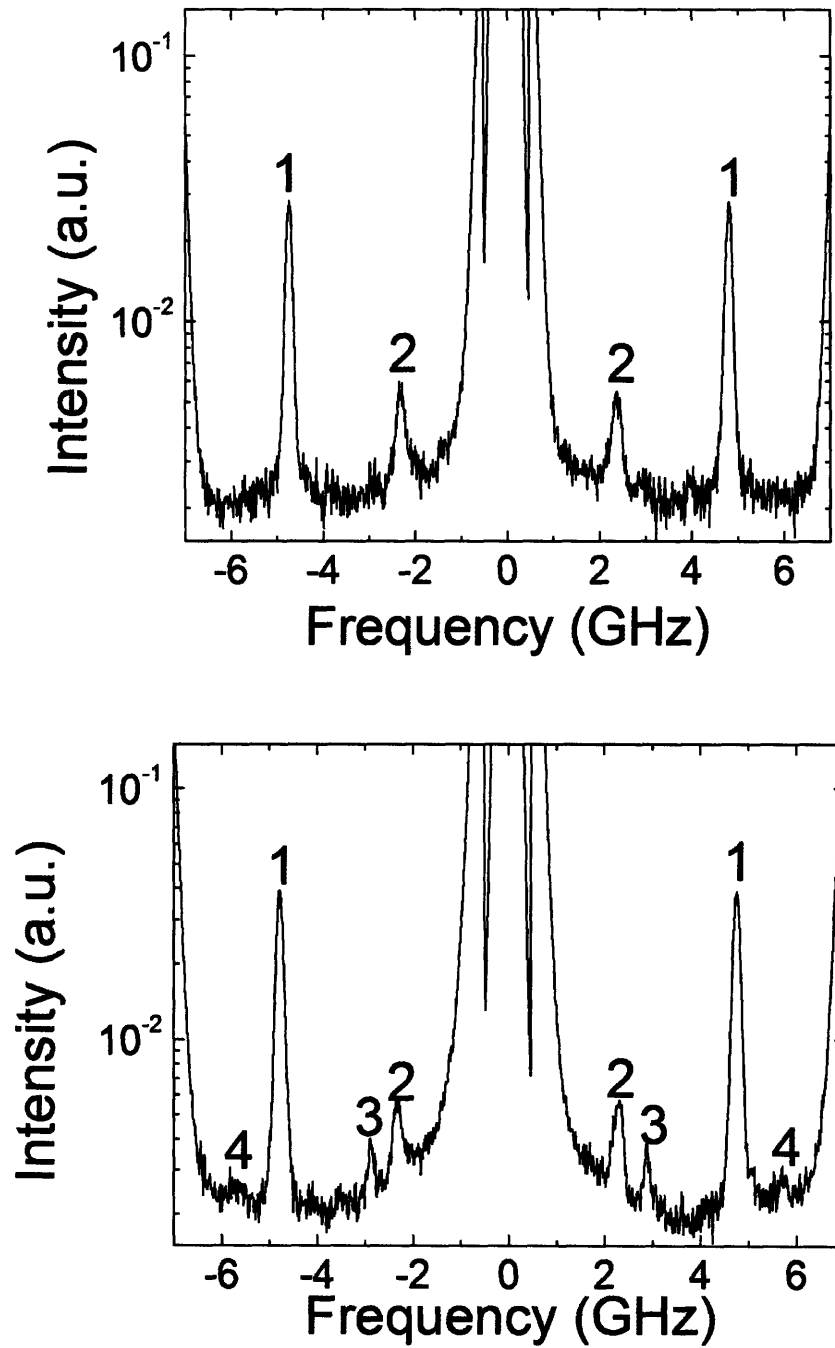


Figure 4.2. BLS spectrum of the samples at $k = 0.0051 \text{ nm}^{-1}$: (a) unpatterned epoxy film; (b) s1 pattern.

The spectrum of s1 is more complex. In addition to the most intense glass peak (1) at the same frequency, we see three less intense peaks, (2), (3), and (4), coming from various bands of the phononic crystal. The position of the lowest frequency longitudinal phonon peak (2) is shifted slightly from $f = 2.34 \text{ GHz}$ to $f = 2.29 \text{ GHz}$, in comparison with the corresponding peak (2) of the unpatterned film, due to the decrease of the effective sound velocity in the porous polymer structure of sample s1 (4% porosity). The two new peaks (3) and (4) correspond to propagation states in the higher bands of the phononic crystal. Repeating our measurements for k from 0.0005 nm^{-1} to 0.009 nm^{-1} , we obtain the complete phononic band diagrams for the $[110]$ propagation, as shown in figs. 4.3 (a) and 4.3 (b) for samples s1 and s2, respectively.

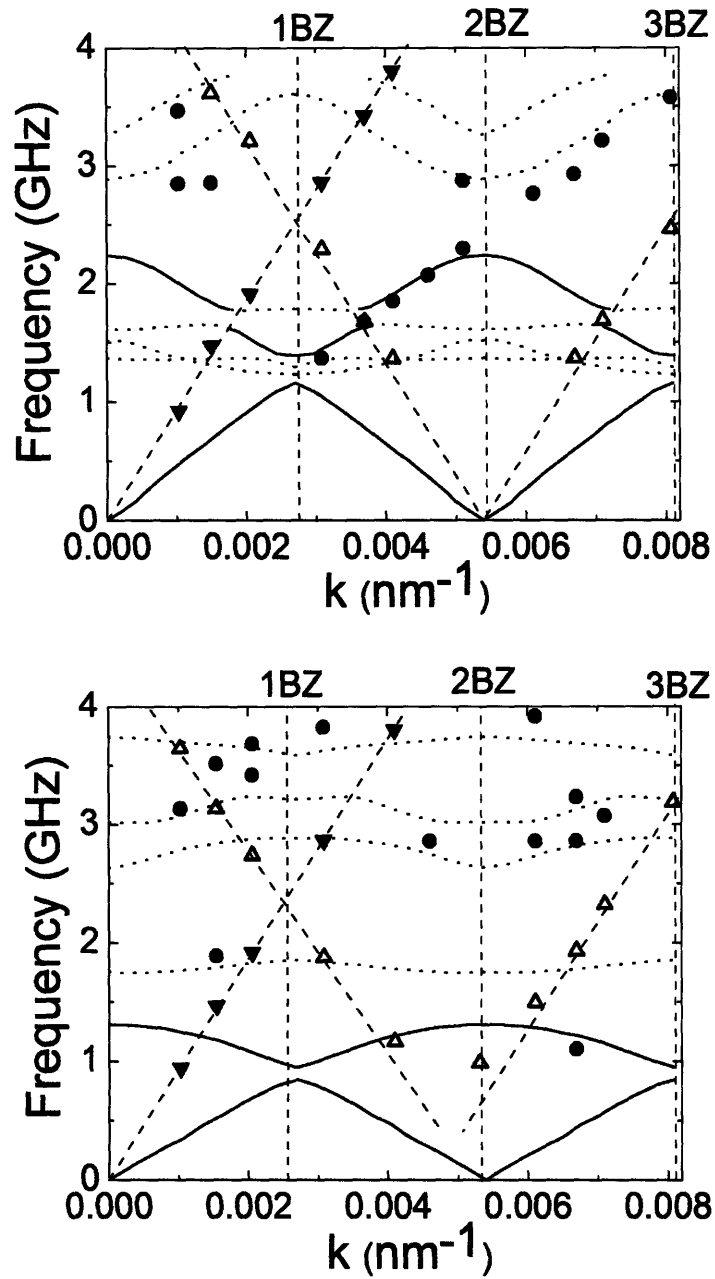


Figure 4.3. Experimental and selected theoretical phononic modes for s1 (top) and s2 (bottom) samples, respectively, for the phonon wave vector parallel to the $[100]$ direction. Solid triangles – glass mode; open triangles – Bragg mode; solid circles – phononic crystal modes; solid lines – theoretical quasilongitudinal modes; dotted lines – theoretical mixed modes.

To provide a basic for the interpretation for the observed modes, we calculate the theoretical band diagrams and compare them with the experimental data. Finite element analysis based on the weighted residual formulation [75] is employed to model the properties of the elastic structures. Because of the periodicity of the structure, the displacement field $\vec{u}(\vec{r})$ must satisfy Bloch's theorem. As a result, periodic Bloch conditions

$$\vec{u}(\vec{r} + \vec{a}) = \vec{u}(\vec{r}) \exp(i\vec{k} \cdot \vec{a}) \quad (4.1)$$

are used to relate the displacements at the boundaries. The interior air region is modeled using zero-traction boundary conditions at the air-material interface [76]. The background was taken to be epoxy with $\rho = 1.19 \text{ g/cm}^3$, $c_t = 1.8 \text{ km/s}$ and $c_L = 3.1 \text{ km/s}$.

Figures 4.4 (a) and 4.4 (b) show the calculated dispersion relationship for the in-plane propagation, where the displacement field \vec{u} is normal to the axis of the cylinders for samples s1 and s2, respectively. Solid lines are QL modes, dashed lines are QT modes and dotted lines are mixed modes.

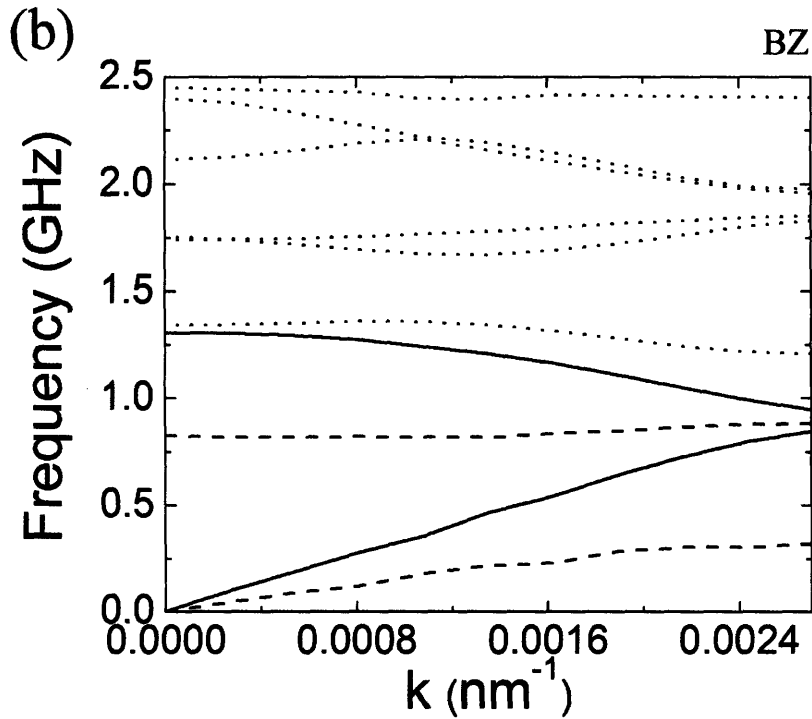
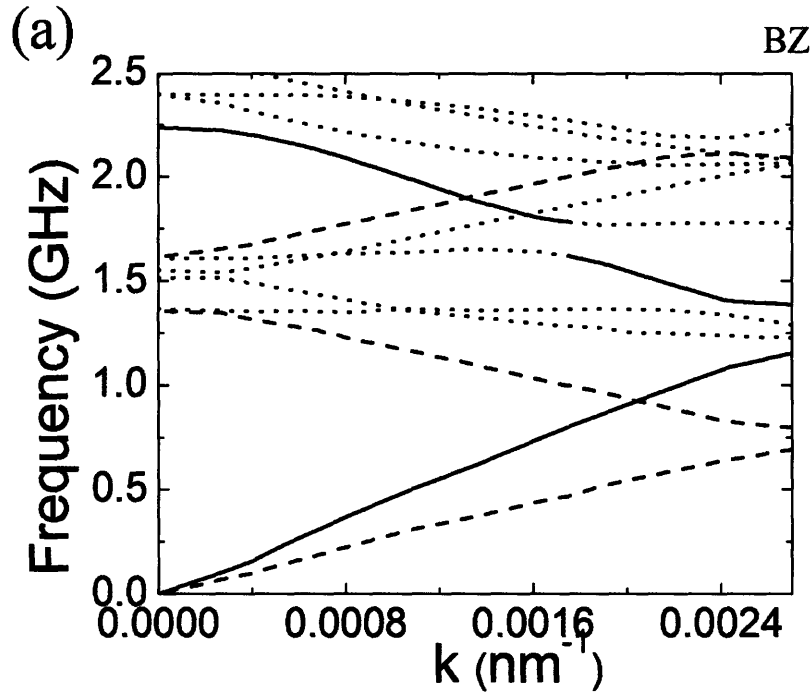


Figure 4.4. The theoretical band diagrams for s1 (a) and s2 (b) samples for the phonon wave vector parallel to the $[100]$ direction. Solid lines represent quasilongitudinal modes; dashed lines – quasitransverse modes; dotted lines – mixed modes. The Brillouin zone boundary along this direction is at $\frac{2\pi}{\sqrt{3}a} = 0.00267 \text{ nm}^{-1}$

To visualize the differences among various propagation modes, we compute and compare their displacement fields, see figure 4.5. For lower-lying modes, \vec{u} is essentially either perpendicular or parallel to \vec{k} . We therefore label these modes as the QL and QT waves, (figs. 4.5 (a) and 4.5 (b)). In contrast, the higher band propagation modes are typically strongly mixed and cannot be approximated as either longitudinal or transverse waves (fig. 4.5 (c)). We also find that the same mode can have predominantly longitudinal displacement field character for one range of k and strongly mixed displacement field character for another range of k (fig. 4.4). Scattering intensities of these modes are vastly different [40], as described in the section 2.2. QL phonons will scatter light significantly, while contributions from the QT modes will not be detected. The intensity of the mixed mode peaks will depend on their field distributions and must be evaluated separately for each mode. However, their strength will be less than that of the QL peaks. For this reason, the low frequency peak (2) in the s1 spectrum (fig. 4.2 (b)) is more intense than peaks (3) and, especially, (4).

Figures 4.3 (a) and 4.3 (b) superpose experimental data points and the theoretical lines on the same graphs. Only QL modes (solid lines) and strongly scattering mixed modes (dotted lines) are plotted. The spectrum of sample s1 has contributions from the second QL mode, while the first QL mode is at frequencies too low to be detected. In addition, we see the signature of the strongly scattering mixed modes at the higher frequencies.

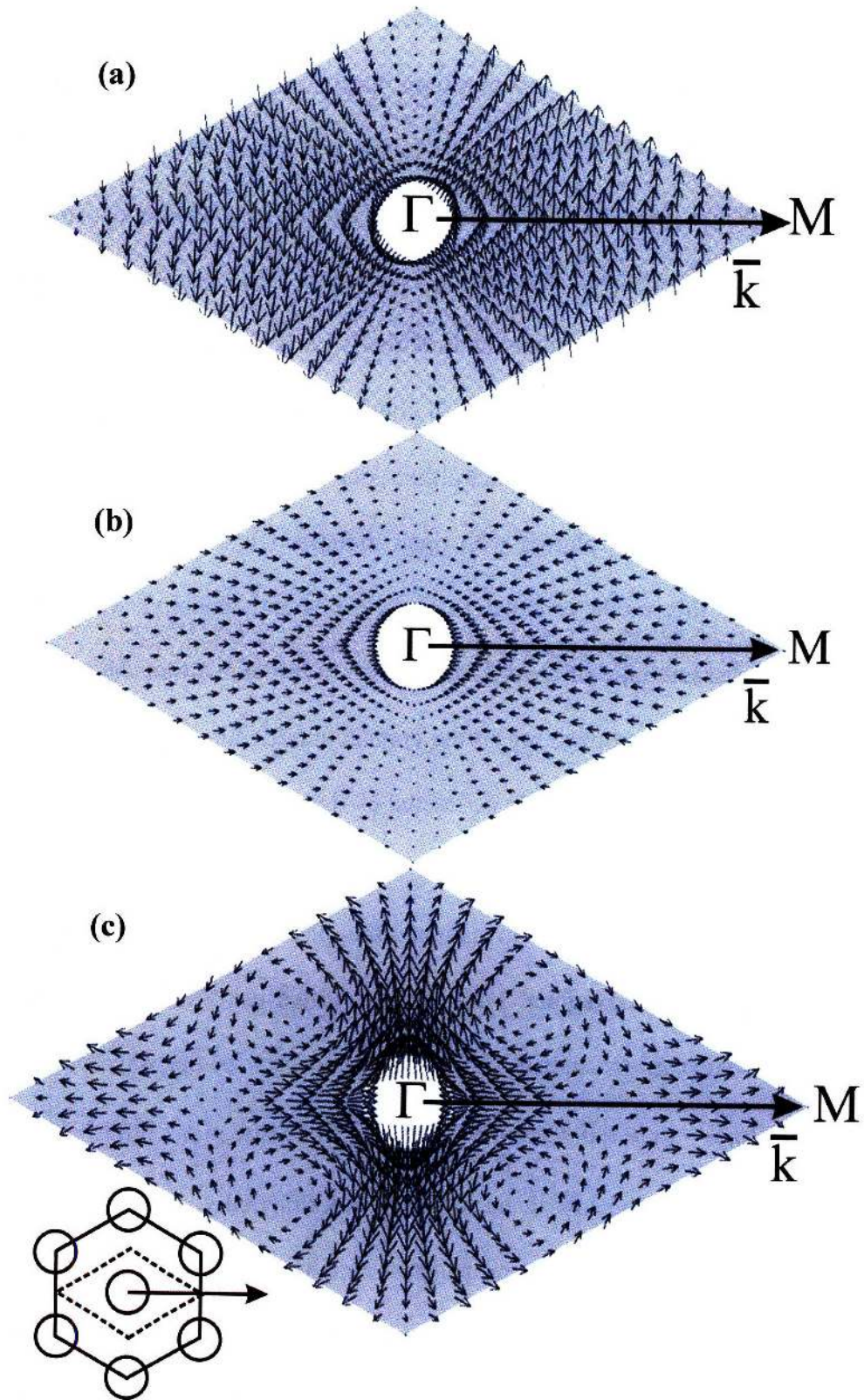


Figure 4.5. Displacement fields for quasitransverse (a), quasilongitudinal (b) and mixed (c) modes computed at $k = 0.0027 \text{ nm}^{-1}$ in s1 sample. The insert shows the measurement direction.

The spectrum from sample s2 is very different. Because of the higher porosity, the effective sound velocity decreases so that both the first and second QL modes are below the BLS detection threshold. All the higher modes are mixed. Experimental data points follow the calculated lines well, but in some places along the theoretical lines expected experimental data points appear missing. This behavior is not surprising. The scattering from the mixed modes is k -dependent and relatively weak. Therefore, for some values of k it may be impossible to detect peaks even after long accumulation times. Finally, there is one mode in both the s1 and s2 spectra that does not follow any theoretical line. It is labeled as Bragg mode and plotted with open triangles (figs. 4.3 (a) and 4.3 (b)). The sound velocity of this mode is equal to the glass sound velocity, while its negative dispersion is a characteristic of crystalline samples. We believe that this mode does not represent a new phonon propagating in the crystals mode, but rather it originates in the scattering of secondary optical beams diffracted by the patterned sample [69].

In summary, in this section we investigate the phonon dispersion relations of 2D hypersonic crystals with hexagonal symmetry fabricated using interference lithography. Brillouin light scattering is used to record phonon spectra for the wave vectors ranging from $k = 0.001 \text{ nm}^{-1}$ to $k = 0.008 \text{ nm}^{-1}$ along the $[100]$ direction. While phononic band gaps are at frequencies too low to be resolved experimentally, their dispersion relation reveals the presence of multiple propagation modes that belong to higher phonon propagation bands. Finite element analysis is used to compute the theoretical band diagrams and displacement fields. Its results are in excellent quantitative agreement with

experiments using no fitting parameters. This work provides the first experimental evidence for the complex multiband dispersion relation in 2D hypersonic crystals.

4.3 Direct observation of a phononic band gap in 2D square hypersonic crystals

Phononic band gaps have not been observed in the hexagonal crystals discussed in the previous section because their relatively large lattice constants ($a = 1360 \text{ nm}$) lead to the sub GHz values of the midgap frequencies, which are below the detection limit of the BLS apparatus. Thus, it is desirable to use samples with submicron lattice constants (preferably $a < 800 \text{ nm}$) to study the band gap formation in hypersonic crystals. However, Brillouin scattering experiments in samples with a feature size approaching the laser wavelength (532 nm) are extremely challenging due to strong optical diffraction and significant elastic scattering. This places severe requirements for the sample quality. In particular, the pattern thickness must be at least 5-10 microns to insure that sufficient amount of the inelastically scattered light is collected from the crystal. This implies that high-aspect ratio structures (with thickness-to-lattice-constant ratio of at least 10) must be fabricated, which is only possible if a high stiffness photoresist, such as SU8, is used. In addition, samples must be infiltrated with a refractive index matching fluid to minimize optical diffraction and elastic scattering. Ideally, the infiltration fluid should have refractive index equal to that of the sample material, wet the sample, but not dissolve or swell it, have a very low vapor pressure and does not decompose under intense laser radiation for extended periods of time. Generally, high molecular weight organic liquids are used for infiltration. Unfortunately their densities and sound velocities are similar to

those of the photoresist, which reduces the mechanical contrast and decreases the width of the band gap.

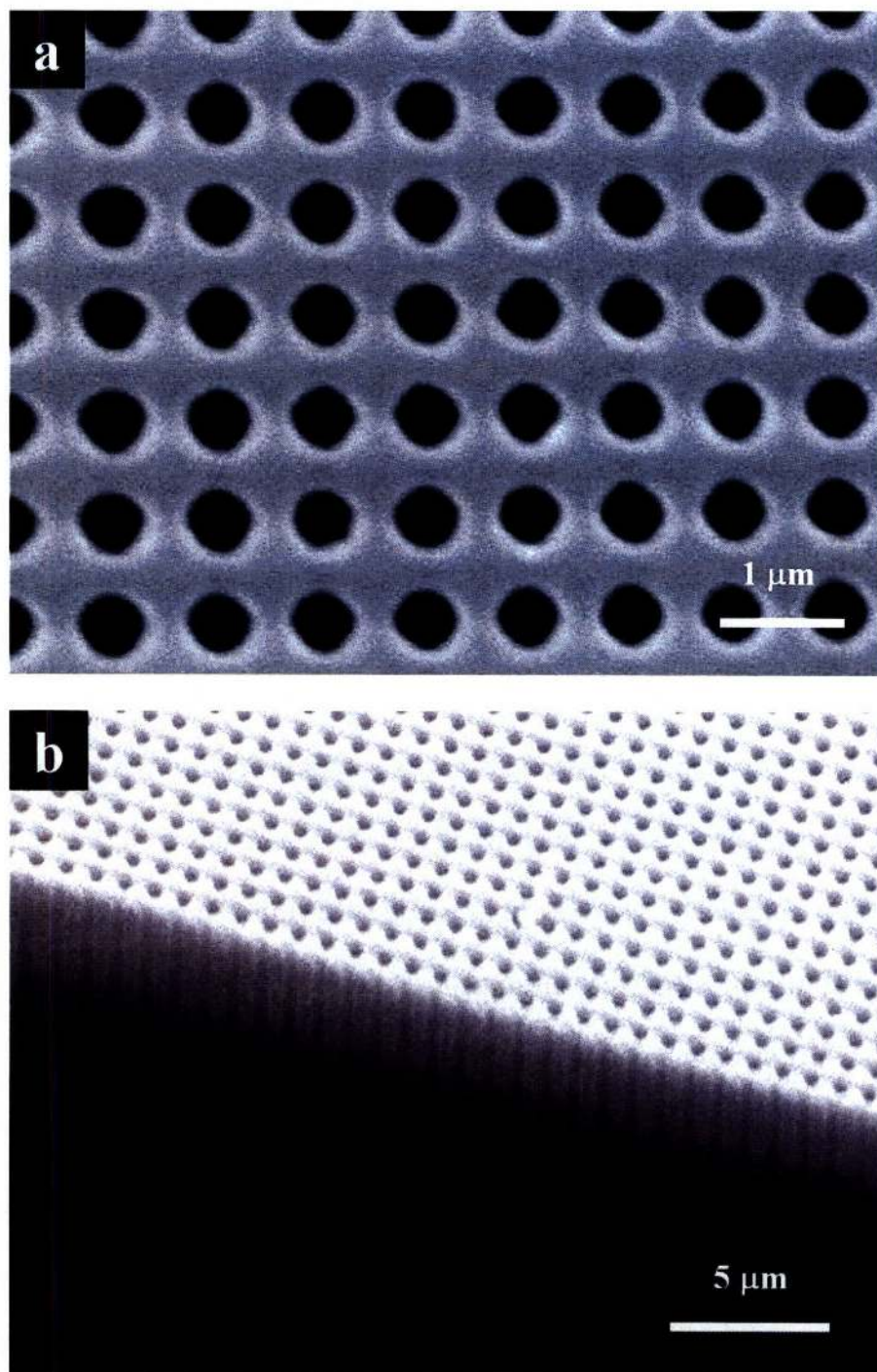


Figure 4.6. SEM images of the top view (a) and the cross section (b) of the 2D crystals demonstrating their single crystallinity, very good uniformity and low defect concentration. The lattice constant is 750 nm, the hole radius is 188 nm and the film thickness is 6 μm.

SEM images of the top view and the cross section of the film are shown in figures 4.6 (a) and (b), respectively. The images were taken using Field-Emission High-resolution SEM (JEOL 6320FV). They reveal excellent uniformity, single crystalline nature and very low defect concentration in the samples over a large area. The film thickness is approximately $d = 6 \mu\text{m}$, while the lattice constant is $a = 750 \text{ nm}$. The samples were fabricated using interference lithography on glass substrates coated with 500 nm thick unpatterned epoxy buffer layers used to improve adhesion. To minimize elastic scattering all samples were infiltrated with a phenylmethyl silicone fluid with $\rho = 1.097 \text{ g/cm}^3$, $n = 1.62$ (at 532 nm) and $c_L = 2.03 \text{ km/s}$. Note that the density, refractive index and sound velocities of epoxy are $\rho_{\text{epoxy}} = 1.19 \text{ g/cm}^3$, $n_{\text{epoxy}} = 1.62$ (at 532 nm), $c_{L_epoxy} = 3.1 \text{ km/s}$ and $c_{t_epoxy} = 1.8 \text{ km/s}$, respectively.

The BLS spectrum taken at $k = 0.0041 \text{ nm}^{-1}$ along the [100] direction, which corresponds to the magnitude of the wave vector at the edge of the first Brillouin zone along this direction, is shown in figure 4.7 (a). The central part of the spectrum at frequencies in the range of $\pm 0.9 \text{ GHz}$ comes from light scattered elastically by static inhomogeneities in the sample and does not provide any information about the phonon modes. Thus, it is masked with a grey rectangle to enhance the overall clarity of the graph. There are three phonon peaks present in the spectrum. The highest intensity peak (g) at 3.72 GHz comes from the glass substrate longitudinal phonons, while the weaker peaks (1) and (2) at 1.21 GHz and 1.57 GHz, respectively, represent phonons propagating in the first and second band of the crystal. The values of the peak frequencies were obtained by fitting the experimental spectrum with a superposition of multiple Lorentzian

shape lines. The overall fit is plotted in the lower part of the graph using a solid red line, while the two individual Lorentzian peaks representing phonon modes from the first and the second propagation band of the phononic crystal are plotted with dashed red lines. Note that the oscillators used to model the elastic background and the glass peak are not shown individually on the graph, even though their contribution is included in the overall fit. The positions of the experimental data and the fit lines are separated to enhance the overall clarity of the graph. The split in the frequencies between modes (1) and (2) $\Delta f = 1.57 - 1.21 = 0.36 \text{ GHz}$ defines the size of the phononic band gap along the [100] direction. The ratio of the gap width to its midgap frequency is

$$\xi = \frac{0.36}{0.5(1.21+1.57)} \cdot 100\% \approx 26\%.$$

To confirm that there are no phonon states in the band gap at other values k we perform the dispersion relation measurements for a range of phonon wave vectors from $k = 0.002 \text{ nm}^{-1}$ to $k = 0.010 \text{ nm}^{-1}$. The results are shown in figure 4.7 (b), where the modes of the periodic pattern are plotted with black circles and the modes of the glass substrate – with black triangles. Furthermore, at higher wave vectors we resolve an additional mode (plotted with black diamonds), which represents the contribution from longitudinal phonons propagating in the unpatterned buffer layer, as can be concluded from its linear dispersion, very weak intensity and sound velocity slightly higher than that of the pattern.

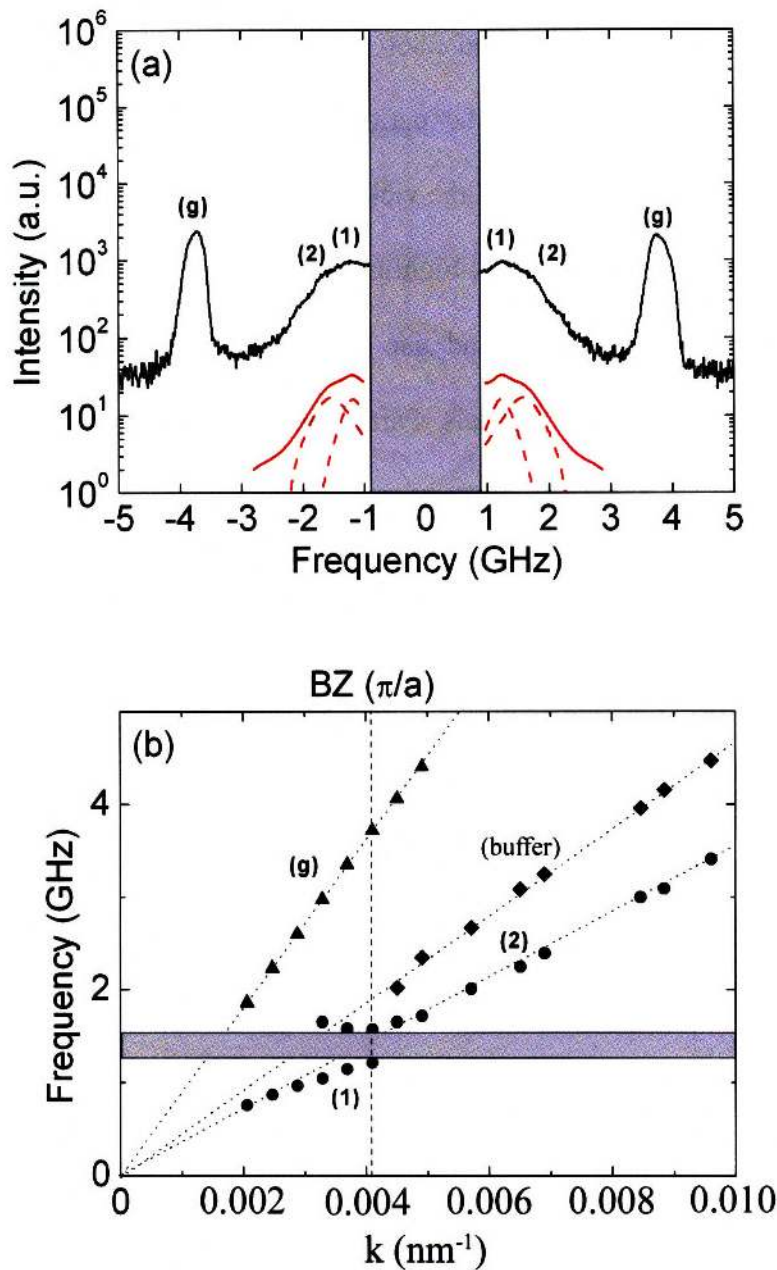


Figure 4.7(a) The BLS spectrum taken at $k = 0.0041 \text{ nm}^{-1}$ that corresponds to the edge of the first Brillouin zone along the $[100]$ direction ($\pi/a = 3.14/750 = 0.0041 \text{ nm}^{-1}$). Peaks (1) and (2) represent phonon modes from the first and the second propagation bands of the periodic pattern and the high intensity peak (g) comes from the longitudinal phonons of the glass substrate. To obtain frequencies of the phonon modes the experimental data were fitted with the multiple Lorentz oscillator model. The resultant fit is plotted in a solid red line, while the oscillators representing phononic crystal modes are plotted in dashed red lines. The oscillators representing elastic scattering and scattering from glass phonons are not shown. (b) The phononic dispersion relation along the $[100]$ direction showing a partial band gap between 1.21 and 1.57 GHz (in grey). Black circles represent the phononic modes of the pattern, black diamonds – the buffer layer, black triangles – glass substrate.

The phonon dispersion curves of the glass substrate and the epoxy buffer layer are linear with the sound velocities of 5708 and 2860 m/s for glass and epoxy, respectively. In contrast, the phonon dispersion of the periodic pattern is nonlinear with significant amount of band bending, especially in the vicinity of the first Brillouin zone edge, which leads to the formation of the band gap, highlighted in grey in fig. 4.7 (b). This is the first direct observation of a phononic band gap along a well defined direction in single crystalline hypersonic phononic crystals. Partial phononic band gaps in polycrystalline materials consisting of a 3D assembly of colloidal poly(styrene) particles have been reported recently by W. Cheng *et al.* [77].

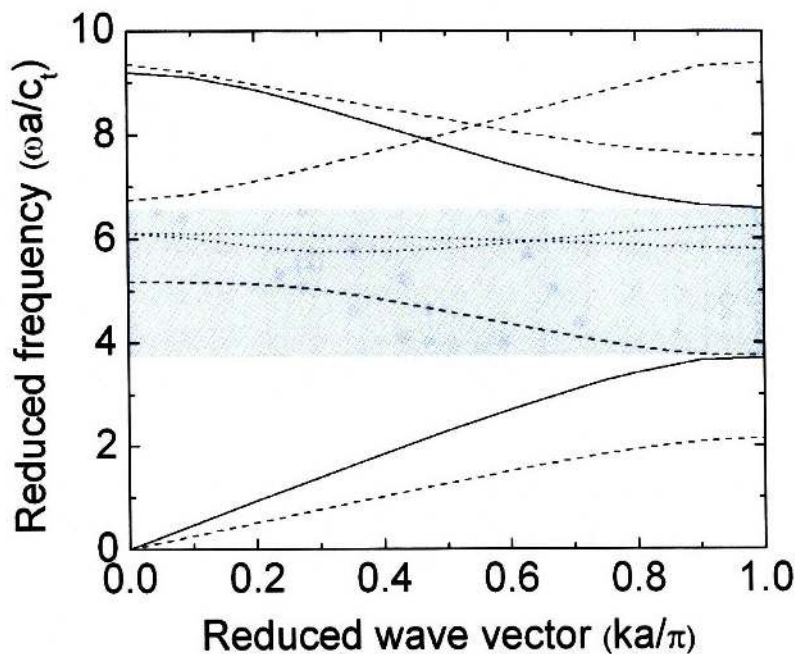


Figure 4.8. Theoretical band diagram for a 2D square epoxy/air phononic crystal with 30% porosity for the phonon wave vector along the $[100]$ direction. QL modes are plotted with solid lines, QT modes – with dashed lines and mixed modes – with dotted lines. The partial band gap for QL phonons is highlighted in grey.

The theoretical phononic band diagram for 2D epoxy/air square crystal with 30% porosity (that corresponds to the uninfiltreated specimen) for the propagation along the

[100] direction is shown in figure 4.8. QL modes are plotted with solid lines, QT modes – with dashed lines and mixed modes – with dotted lines. In VV BLS experiments only the QL modes are detected. Therefore, the experimentally observed partial phononic band gap (fig. 4.7 (b)) corresponds to the gap between the first and the second propagation band for the QL modes, which is highlighted in grey in fig. 4.8. Theory predicts that the ratio of the gap width to its midgap frequency for the QL gap should be $\xi = \frac{6.58 - 3.70}{0.5(6.58 + 3.70)} \cdot 100\% = 56\%$, which is more than twice higher than the experimental ratio. This is expected, since the contrast in density and sound velocities between epoxy and air is much larger than that between epoxy and the refractive index matching fluid.

The phase velocity of sound in the crystal c_{cr} can be obtained from the slope of the experimental dispersion relation in the low \vec{k} (large wavelength) regime, where it is essentially linear, and it is equal to $c_{cr}=2271$ m/s. It is interesting to compare this value with the expected sound velocity of a homogeneous medium consisting of 65% volume fraction of epoxy with $c_{L_epoxy}=2860$ m/s and 35% volume fraction of the refractive index fluid with $c_L=2030$ m/s. The density and the sound velocity of the effective medium is related to the densities and sound velocities of its components by Wood's law:

$(\rho c^2)_{eff}^{-1} = \phi(\rho_L c_L^2)^{-1} + (1 - \phi)(\rho_{epoxy} c_{L_epoxy}^2)^{-1}$. Substituting the numerical values into this equation we obtain $c_{eff}=2446$ m/s. This value is slightly higher than the experimental phase velocity of the pattern in the long range regime. The difference is likely caused by the higher cross linked density of the epoxy buffer layer, which was used to measure the

sound velocity of unpatterned epoxy. The higher cross link density in the buffer layer is expected since the buffer layer photoresist was exposed to higher dose of laser radiation during the polymerization step.

4.4 Conclusions

Two dimensional periodic epoxy-air patterns fabricated in photoresist using interference lithography are well suited for the practical realization of hypersonic phononic crystals. These structures are single crystalline enabling direction dependant measurements of their dispersion relation, while the mechanical contrast between epoxy matrix and air inclusions is very large leading to the appearance of phononic band gaps for a relatively wide range of air volume fractions. In particular, complete 2D band gaps are expected for both square and hexagonal crystals with the porosity higher than 0.4. In addition, a variety of structures with different symmetries and lattice constants can be easily fabricated.

This chapter reports on phononic properties of 2D crystals with hexagonal symmetry and the lattice constant of 1360 nm and 2D crystals with square symmetry and the lattice constant of 750 nm. The phononic dispersion of hexagonal crystals reveals the presence of several propagation modes in complete agreement with the FEA band diagram calculations. Since the lowest order midgap band frequencies of these crystals are at ~ 700 MHz, which is below the detection limit of the BLS apparatus, we were not able to record the formation of the band gaps experimentally. In contrast, the somewhat larger submicron lattice constants of the square crystals lead to higher values of the midgap

frequencies and allow direct observation of the bending of the first and second propagation bands in the vicinity of the first Brillouin zone and the formation of the band gap. This result is the first direct observation of a hypersonic band gap along a well defined direction in a single crystalline periodic structure. It suggests possibilities for experimental engineering of phonon dispersion relations at GHz frequencies and may lead to a number of practical phononic devices, such as high frequency acoustic mirrors and negative refraction based acoustic superlenses.

CHAPTER 5. TUNABILITY OF PHONON DISPERSION RELATION IN 3D ELASTOMERIC STRUCTURES [78]

5.1 Introduction

The ability to fabricate phononic structures that can repeatedly and reversibly change their properties during operation is crucial for a practical realization of phononic devices. Since the dispersion relation of a phononic crystal depends on its lattice geometry and mechanical properties, such a change can be achieved either by tuning its lattice constant and symmetry or by changing the densities and elastic constants (sound velocities) of the constitutive materials.

In this chapter I describe the fabrication of 3D single crystalline elastomeric network/air structures using interference lithography and demonstrate that their phonon dispersion relations can be tuned mechanically by subjecting their lattice to well controlled amount of deformation along a specified direction in the Brillouin zone. This work represents the first experimental demonstration of a mechanically tunable hypersonic phononic crystal.

5.2 Fabrication process

We employ an interference lithographic template (ILT) as a facile mold for fabricating three-dimensional bicontinuous poly(dimethylsiloxane) (PDMS)/air elastomeric structures. PDMS has proven to be an outstanding material for micro- and nanotechnology [79]. For example, PDMS has been employed to make two-dimensional (2D) and three-dimensional (3D) microfluidic devices such as pumps, valves, channels, and cell culture systems [80-81]. PDMS can be deformed reversibly and repeatedly

without residual distortion and is thermally stable, inexpensive, nontoxic, and commercially available. Although PDMS can potentially be cross-linked using light [82], it is not generally used as a photoresist due to the rather inconvenient processing conditions [83,84]. 2D periodic structures patterned by photolithography and then subsequently replicated in PDMS have been demonstrated as deformable optical and acoustic components such as lenses, waveguides, and couplers [85,86]. The relatively low modulus of PDMS ($E \approx 2 \text{ MPa}$) can lead to distortions such as feature-feature pairing and feature sagging in conventional microcontact printing of surface features with high-aspect ratio [87-89]. In structures fabricated by microcontact printing or replica molding, which can possess residual physical stresses from the molding procedure, collapse of structures begins to occur at an aspect ratio of ~ 2 [80,89].

The use of multibeam interference lithography provides a promising approach to the fabrication of large-area and periodic 3D templates on the submicron scale both rapidly and cheaply. Importantly, it affords control over geometrical elements of the structures such as symmetry and volume fraction, see section 2.3 for more detail.

Figure 5.1 shows the three steps of the fabrication process for the 3D elastomeric network/air materials. In the first step, a 3D ILT is fabricated in a positive resist by a single exposure to a periodic light intensity distribution, followed by development (Figure 5.1 (a) and (b)). Due to the high surface tension of water, which can potentially cause the pattern to collapse, supercritical drying has been suggested in the case of aqueous-based photoresist [92]. However, supercritical drying of our photoresist resulted

in the formation of cracks. Therefore we replaced water with pentane, which has a lower surface tension (73.05 mN/m for water and 13.72 mN/m for pentane at 20 °C [93]).

In the second step, the open 3D network structure is completely filled with PDMS prepolymer via vacuum assisted infiltration and the PDMS cured in the dark (fig. 5.1 (c)). Finally, in step three, a second flood exposure to UV light is done to make the template easily soluble in a dilute basic solution. PDMS is transparent in the UV-vis region and does not prevent the radiation from reaching the template. Upon the second exposure, the diazonaphthoquinone, which still remains in the initially unexposed regions, changes into carboxylic acid and renders the template soluble in basic solution.

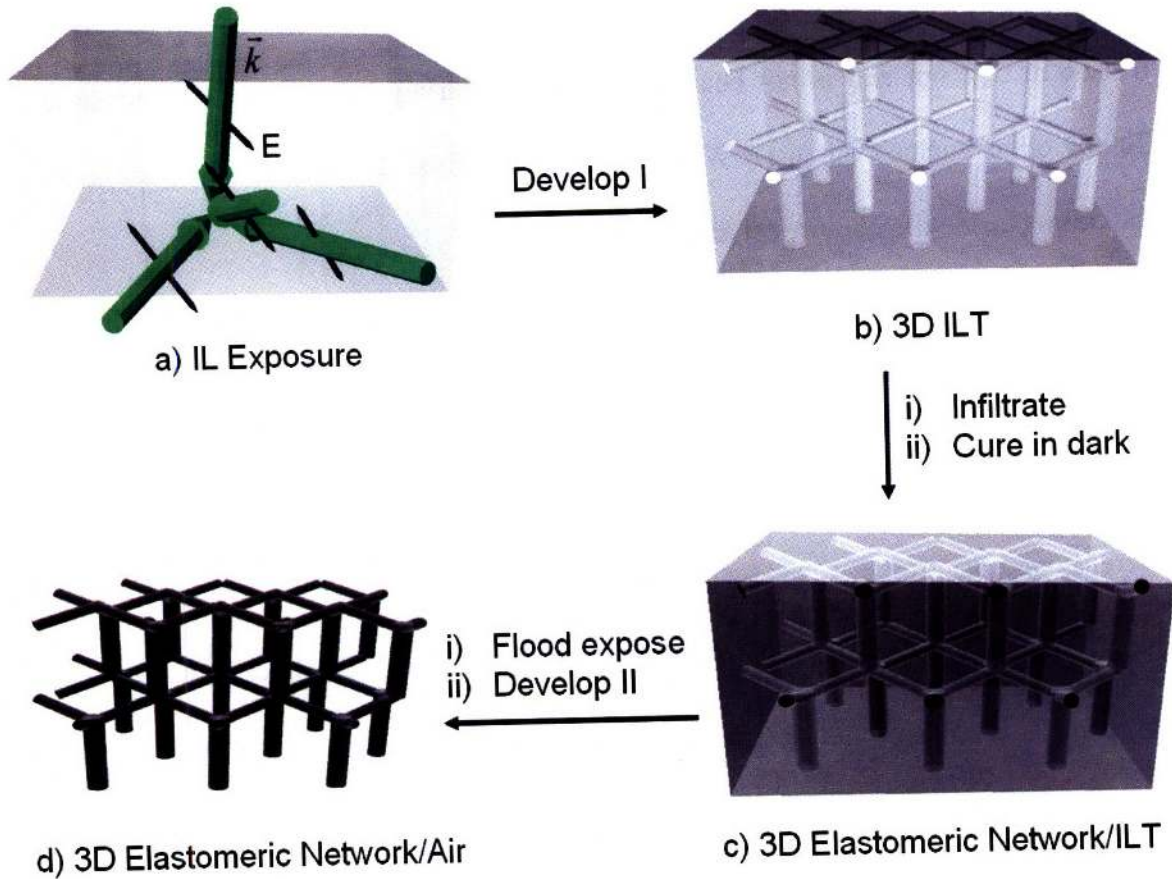


Figure 5.1. Schematic illustration showing the fabrication process for the 3D continuous elastomeric network/air structure. (a) Exposure by interference lithography (IL). Large arrows show the direction of the beam while small arrows show the direction of polarization of each beam. (b) 3D interference lithography template (ILT) fabricated in a positive resist. (c) 3D elastomeric network/ILT structure from the replication of the PDMS into the ILT. (d) 3D elastomeric network/air structure after flood exposure under UV lamp and subsequent removal of template in a water-based developing solution.

The periodic intensity pattern that will become the void space for templating the PDMS is formed by the interference of four laser beams from the output of a 532 nm continuous wave, frequency-doubled Nd:YVO4 laser. The Gaussian output from the laser was converted into a top hat function using a refractive beam shaper. The light intensity distribution depends on the relative directions and polarizations of the interfering beams. The overall film thickness is limited by absorption of the photoresist at 532 nm. The attenuation coefficient of AZ-5214-E is $k' = 0.0028$ (from ellipsometric measurements),

which readily permits pattern thicknesses of 3 μm . The refractive index of AZ5214-E is $n=1.66$ at 532 nm and is not changed detectably during exposure (measured on a M-2000D ellipsometer from J. A. Woollam Co.). The final directions and polarizations of the beams inside the photoresist are given by:

$$\begin{aligned}
\vec{k}_0 &= [0.0122, 0.0122, 0.0122] & \vec{E}_0 &= [0, -5.74, 5.74]; \\
\vec{k}_1 &= [0.0164, 0.0073, 0.0073] & \vec{E}_1 &= [0, -2.45, 2.45]; \\
\vec{k}_2 &= [0.0073, 0.0164, 0.0073] & \vec{E}_2 &= [0.97, -1.75, 2.97]; \\
\vec{k}_3 &= [0.0073, 0.0073, 0.0164] & \vec{E}_3 &= [-0.97, -2.45, 1.75].
\end{aligned} \tag{5.1}$$

Here \vec{k}_i and \vec{E}_i are the wave vector and polarization of the i -th beam respectively. The isosurface of the theoretical light intensity model is shown in figure 5.2 (a). The 3D structure is a four-functional network with symmetry corresponding to the $R\bar{3}m$ space group. The basic motif is comprised of a vertical post 1100 nm in length and 500 nm in diameter with three shorter struts directed outward from the post, as shown in the inset. Despite aspect ratios of about 2, our structures do not collapse which can be attributed to both the interconnected nature of our structure and a low residual stress.

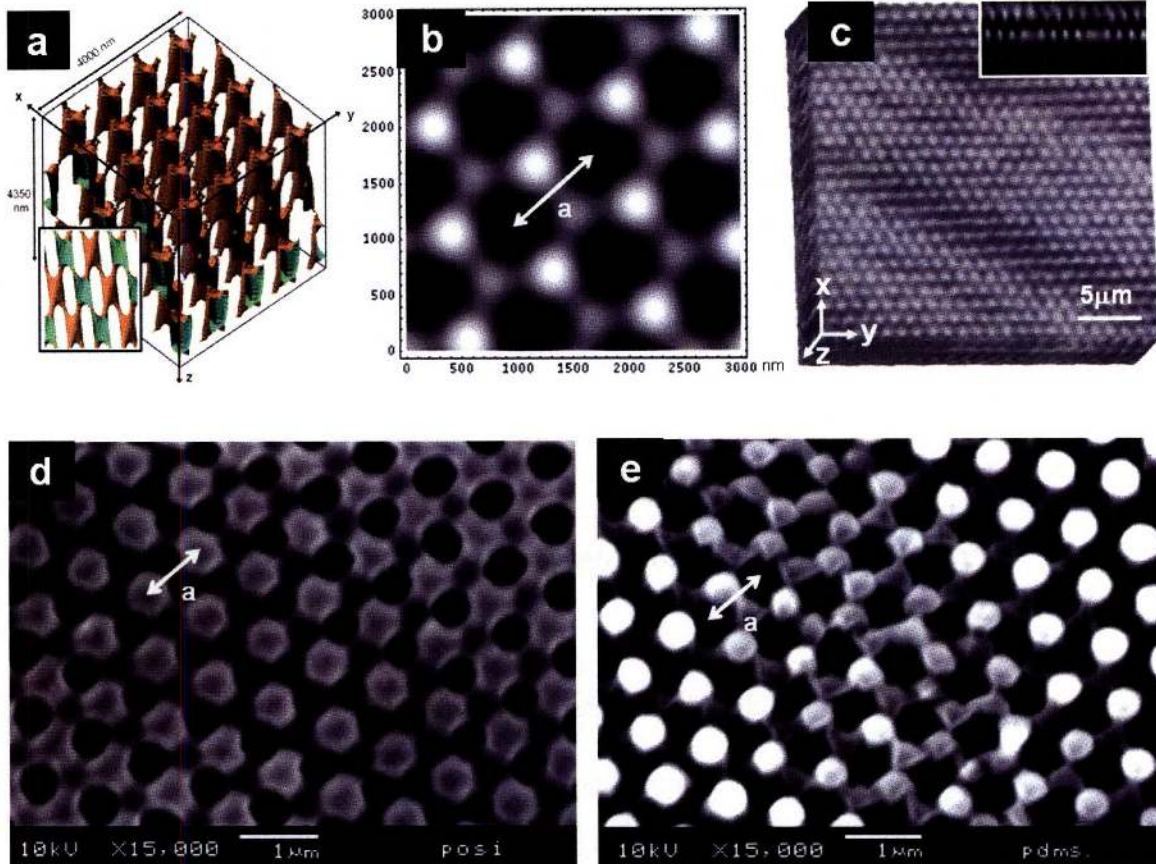


Figure 5.2. Comparison of theoretical and experimental structures. (a) Isosurface of theoretical light intensity model. The inset is view normal to the $(11\bar{2}0)$ planes of the structure. (b) Calculated 3D light intensity profile interference in the (0001) plane. (c) Reconstructed confocal image showing a perspective view of the PDMS elastomeric structure. The inset is the view of y-z cross-sectional plane of the structure corresponding to the schematic views in the inset of (a). (d) SEM image of ILT pattern fabricated in a positive photoresist (AZ5214-E) with a lattice spacing of 980 nm. (e) SEM image of 3D templated PDMS network/air structure having the complementary structure to (d).

Figure 5.2 (a) shows the isosurface of theoretical light intensity model. The inset is a view normal to the $(11\bar{2}0)$ planes of the structure. Figure 5.2 (c) is a confocal micrograph and the inset is the y-z cross-section image demonstrating good correspondence with the schematic view shown in the inset of figure 5.2 (a). The PDMS elastomeric structure is the complement of the positive resist template and very closely resembles the light intensity pattern displayed in fig. 5.2 (b) (compare parts (b) and (e) of fig. 5.2). The

expected periodicity (“a” in fig. 5.2 (b)) in the (0001) plane based on the ILT parameters is 980 nm, and this agrees with the SEM images of the (0001) plane of the experimental structure (figure 5.2 (d) and (e)), confirming that the transfer of the light intensity pattern into PDMS via ILT occurs with high fidelity. The larger scale periodicity in the confocal and SEM images is caused by the photoresist surface being at a slight angle to the (0001) plane of the interference pattern.

5.3 Tunability of the phonon dispersion relation in 3D periodic PDMS elastomeric structures

Mechanical tunability of the phonon dispersion relation of our elastomeric structures is demonstrated through BLS measurements of the samples with various degrees of deformation. In particular, the dispersion relations of the undeformed sample and the sample subjected to 30 % strain along the $[10\bar{1}0]$ direction were recorded. In situ monitoring of the PDMS under tensile in-plane deformation was conducted by securing the PDMS sample in a microstretcher mounted on an atomic force microscope stage (AFM). AFM images (figs. 5.3 (c) and (d)) show the details of the change in the sample lattice parameter and symmetry due to the 30% unidirectional strain applied along the $[10\bar{1}0]$ direction. As clear from this image, the unit cell size along the tensile strain direction increases by 30% accompanied by the reduction of spacing in transverse direction thus demonstrating affine deformation of PDMS structure.

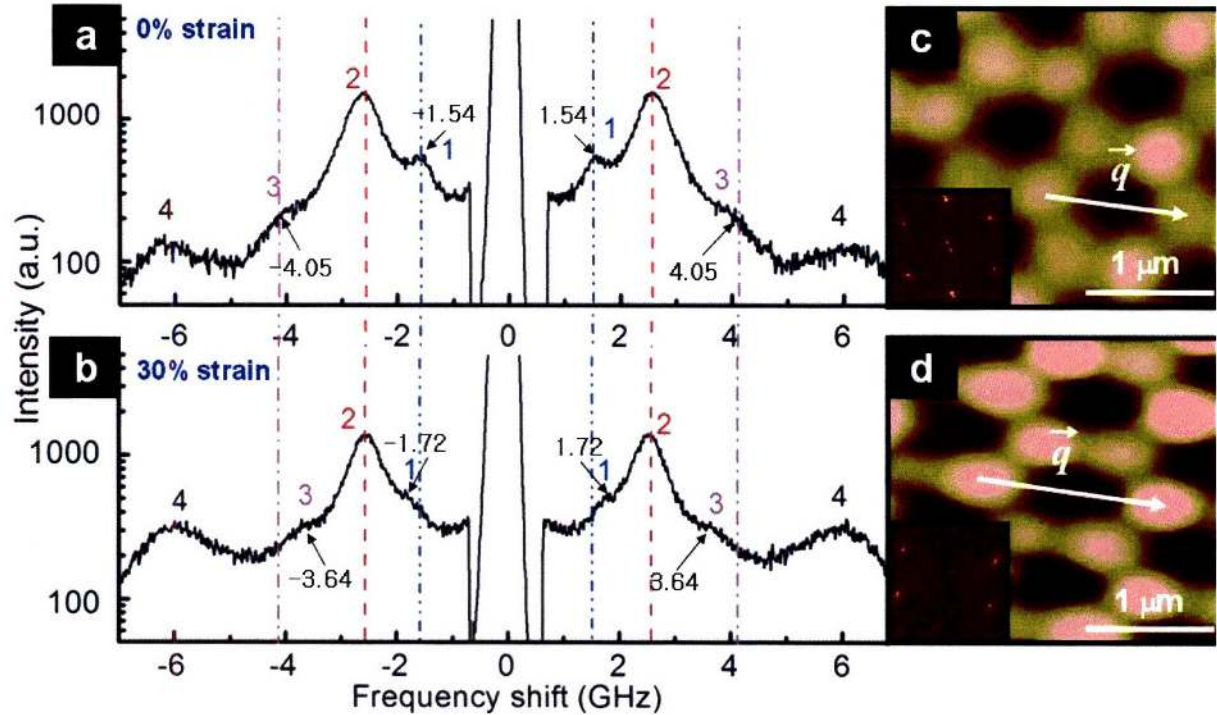


Figure 5.3. BLS spectra of PDMS elastomeric structures at $k = 0.0139 \text{ nm}^{-1}$ with 0% (a) and 30% tensile strain (b) along the $[10\bar{1}0]$ direction. Peaks (1) and (3) derive from the phonons propagating in the phononic crystal and are shifted by the deformation. Peak (2) arises from the longitudinal phonons of the unpatterned PDMS substrate and remains unchanged. Peak (4) is a result of backscattered light. The phonon wave vector is oriented along the $[10\bar{1}0]$ direction. AFM images with 0% (c) and 30% tensile strain (d) along the same direction clearly show the change in the lattice parameter and symmetry upon deformation. Insets are FFT of the AFM images.

BLS was employed to obtain information about the phononic dispersion relation of the PDMS elastomeric crystals. In Brillouin experiments light is scattered inelastically by thermal phonons. BLS allows for the simultaneous determination of phonon frequency and wave vector by measuring the frequency shift of the scattered light at a known scattering angle. The amplitude of the phonon wave vector can be selected by adjusting the scattering angle, while its orientation with respect to the crystal lattice can be chosen by rotating the sample in the plane perpendicular to the scattering plane (the scattering plane is defined by the incident and the scattered laser beams, see section 2.3). Both

incident and scattered light are polarized normal to the scattering plane (s-polarized). The frequencies of various phonon modes are obtained by numerical fitting of the experimental data with multiple Lorentzian peaks.

The corresponding BLS spectra exhibit four peaks, see figs. 5.3 (a) and (b) for the spectra of undeformed and deformed sample, respectively. Relatively weak peaks (1) and (3) come from the QL phonons propagating in the PDMS pattern, while a much stronger peak (2) results from the scattering by longitudinal phonons in the unpatterned PDMS substrate. The magnitude of the phonon wave vector for peak (4) is always twice that of the photon wave vector and does not depend on the scattering angle. This k -independent high-frequency peak (4) arises from the contribution of light backscattered by phonons (by 180°) that is then elastically reflected from the front surface of the sample. Note that the position of the substrate peak (2) is unchanged during deformation, while peaks arising from the PDMS/air structure shift from 1.54 to 1.72 GHz and from 4.05 to 3.64 GHz (peaks (1) and (3), respectively).

Repeating the BLS measurements for a range of wave vectors from 0.001 nm^{-1} to 0.012 nm^{-1} we obtain phononic band diagrams for both undeformed and strained samples, as shown in figure 5.4. The dispersions of the undeformed and strained sample are plotted in red and blue colors, respectively. Substrate phonons are plotted in black. The edge of the first Brillouin zone moves to the lower k values upon deformation causing corresponding shifts in the positions of the propagation bands of the pattern. In addition, one propagation mode that is present in the spectrum of the undeformed sample

completely disappears after the deformation. We believe that this behavior is related to the change in symmetry upon deformation. No phononic band gap can be resolved due to the interference of a very strong signal from the PDMS substrate at the same frequencies, see also figs. 5.3 (a) and (b).

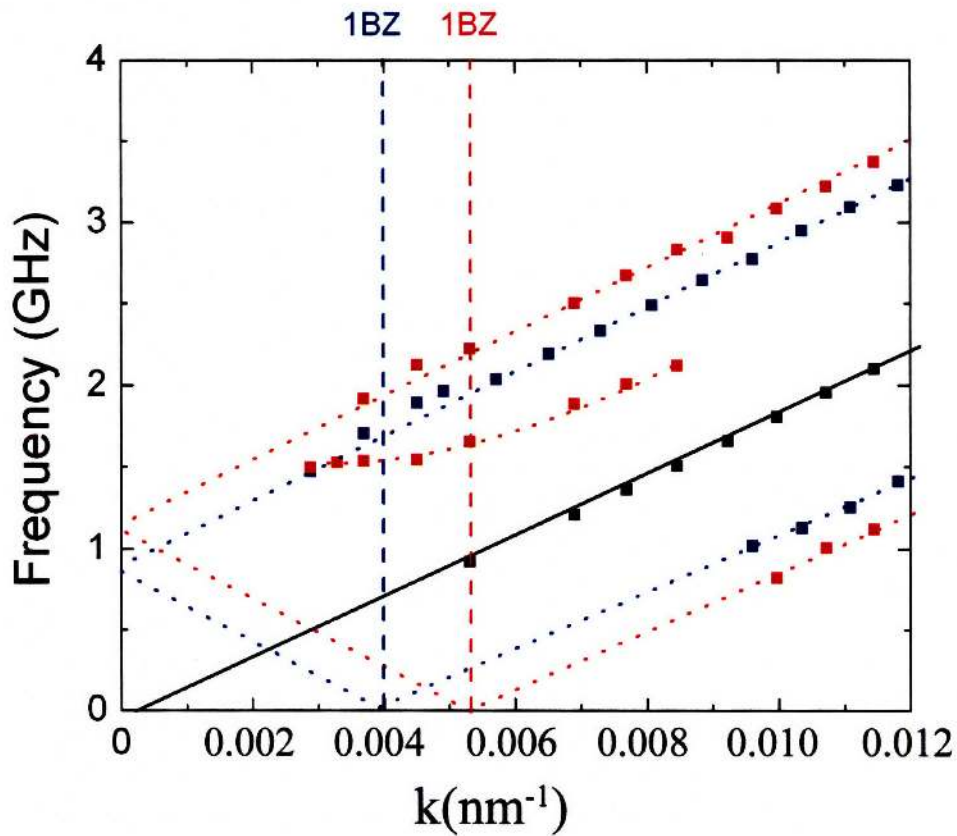


Figure 5.4. The phonon dispersion relation of the 3D PMDS/air structures measured along the $[10\bar{1}0]$ direction. Red dots – phonon modes of the undeformed pattern, blue dots – phonon modes of the strained pattern (30% along the $[10\bar{1}0]$ direction), black dots – substrate contribution.

5.4 Conclusions

The tunability of the phonon dispersion relation is very important for the practical realization of phononic devices. In this chapter we described fabrication of mechanically tunable hypersonic phononic crystals by creating 3D periodic patterns in PDMS using interference lithography. The fabrication approach employed avoids PDMS swelling or pattern collapse. In this approach a positive photoresist is used to make the interference lithography template and after infiltration with PDMS precursor and curing the resist is flood exposed and then removed in a water-based basic solution resulting in single crystalline periodic structures with submicron lattice parameters and 200 nm feature size.

To demonstrate the mechanical tunability our structures were subjected to 30% strain along the $[10\bar{1}0]$ direction and their phononic band diagrams were recorded using BLS for k parallel to the $[10\bar{1}0]$ direction. The deformation of the lattice leads to the change in size of the Brillouin zone and corresponding shifts in the positions of phonon propagation bands. In addition, one of the phonon modes present in the spectra of the unstrained sample disappears after deformation, likely due to the change in the symmetry. The results described in this chapter present the first experimental demonstration of tunable hypersonic phononic crystals.

CHAPTER 6. THESIS SUMMARY

Periodic materials with submicron lattice constants possess rich and complex phonon dispersion relations at hypersonic frequencies. The most exciting feature of their dispersion relation is the appearance of multiple propagation bands separated by band gaps, where no elastic waves are allowed to propagate. The physics of elastic wave propagation in periodic media is very complex due to a large number of structural and materials parameters involved, such as structural symmetry, component material densities, longitudinal and transverse sound velocities of the constitutive materials. Furthermore, the behavior of solid/solid phononic crystals is notably different from that of solid/fluid crystals, which is in turn different from that of fluid/fluid crystals. The rather large parameter space leads to higher complexity in analyzing phononic crystals as compared to better known photonic crystals, but at the same time it allows more flexibility in designing materials with desirable phononic properties.

This thesis explores the phononic dispersion relations of a variety of periodic submicron structures using an integral approach that combines experimental fabrication and characterization and theoretical numerical analysis. The objectives of this investigation are twofold. First, we seek to develop materials that can extend control over propagation modes and over the density of states of high frequency acoustic phonons. These materials may find applications in high resolution acoustic microscopy, nondestructive evaluation techniques, acousto-optics and heat management. Second, we employ phonon dispersion measurements as a tool to learn about mechanical properties of materials at the nanoscale. In particular, knowledge of the phonon dispersion relation can be used to compute elastic

constants of isotropic and anisotropic materials, while the temperature dependence of the speed of elastic waves in a material provides a way to study the glass transition in polymer nanolayers.

In the first part of this thesis, phononic properties of anisotropic PET/PMMA and isotropic PC/PMMA multilayer films are studied as a function of their lattice constant and composition. A gradual increase in complexity of the phonon dispersion relation is observed as the lattice constant a becomes comparable to or larger than the phonon wavelength λ . Films with $a \ll \lambda$ exhibit one longitudinal and one transverse mode in complete correspondence to the dispersion relation of an effective homogeneous medium. The temperature dependence of the sound velocities also reveals a single breaking in the c_L vs. T curve corresponding to the glass transition temperature of the average medium.

In contrast, films with $a > \lambda$ display several distinct propagation modes. FEA computations suggest that these modes represent layer-guided phonons with displacement fields localized almost entirely within individual polymer layers and not throughout the film as for a homogeneous medium. This suggestion is confirmed by the temperature dependence of sound velocities, which reveals several distinct breaking points in the c_L vs. T curve corresponding to the glass transition temperatures of PET and PMMA, and the glass transition temperatures of PC and PMMA for anisotropic PET/PMMA and isotropic PC/PMMA samples, respectively. In addition, fitting the theoretical dispersion relations to the experimental data allows determination of elastic constants for individual polymer nanolayers.

Next, properties of 2D hypersonic phononic epoxy/air crystals fabricated using interference lithography are investigated. These structures are single crystalline allowing direction-resolved measurements of their phononic band diagram. In addition, a variety of samples with both square and hexagonal lattice symmetry and various volume fractions were made available. Finally, the large mechanical contrast between the solid polymers (epoxy) and air assures the formation of phononic band gaps for a wide range of air volume fractions. We observe experimentally the presence of multiple propagation bands and the appearance of phononic band gaps at the edge of the first Brillouin zone in these samples. FEA computations are in very good agreement with the experimental dispersion relations using no fitting parameters. This work is the first experimental study of the phonon dispersion relation of single crystalline 2D submicron structures and it clearly demonstrates the existence of phononic band gaps at hypersonic frequencies.

The final part of this thesis is dedicated to the fabrication of phononic structures with a dispersion relation that can be tuned by the application of an external stimulus. In particular, we use PDMS to create mechanically tunable hypersonic crystals. A novel process to fabricate 3D periodic elastomeric structures is developed based on PDMS infiltration of an interference lithography patterned positive resist template with subsequent removal of the template in a water-based basic solution. No swelling or pattern collapse occurs during this process.

The PDMS/air phononic crystals were subjected to various degrees of deformation along the $[10\bar{1}0]$ direction and their dispersion relations were recorded and analyzed. The deformation is reversible and can be executed repeatedly without causing any damage to the crystals. We find that the change in the size of Brillouin zone leads to the shift in frequencies of phonon propagation bands, while the change in the structural symmetry causes some phonon modes to disappear. This work is the first experimental demonstration of mechanically tunable hypersonic crystals and it opens a pathway towards practical realization of tunable phononic devices.

CHAPTER 7. DIRECTIONS FOR FUTURE INVESTIGATIONS

The main result of this thesis is the development of techniques to fabricate and analyze hypersonic phononic crystals and the experimental demonstration of phononic band gaps in the GHz frequency range. It lays the foundations for *phonon dispersion engineering* in periodic nanostructures and opens a number of exciting directions for the future investigations.

From the theoretical viewpoint, we still need to identify the champion phononic structure, i.e. the structure with the largest phononic band gap for a given contrast in mechanical properties of materials. Moreover, the champion structure does not need to be the same for solid/solid, solid/fluid and fluid/fluid crystals or for 2D vs. 3D and the differences among these classes of phononic crystals should be carefully addressed. Finally, it is important to consider practical issues related to the fabrication of the champion structures. Interference lithography is a superior technique for the fabrication of phononic crystals, but it has limitations in what kinds of structures can be accessed due to a finite number of laser beams that can be used to create the interference pattern. It is desirable not only to identify the champion structures, but also to assure that they can be fabricated using interference lithography or other techniques, such as self-assembly or phase mask lithography. If the fabrication is not feasible, then there is significant practical interest in identifying approximate champion structures, which would still have good phononic properties and can be more easily fabricated.

There is also a wide range of exciting topics for experimental studies of hypersonic phononic crystals. Clear and convincing demonstration of a *complete* phononic band gap in 3D hypersonic structures would be a natural extension of the study of 2D crystals described in this thesis. However, currently all 3D structures fabricated using interference lithography include only a limited number of unit cells in the direction normal to the sample plane (usually less than 10 unit cells) and cannot be approximated as infinitely periodic in this direction. It is possible to obtain bulk-like 3D structures with self-assembly, but these structures tend to be polycrystalline and do not allow direction-resolved measurements. Thus, fabrication methods must be improved to create significantly thicker structures, while preserving low defect concentration and single crystallinity of the lattice.

Phonon localization on defects has tremendous practical importance. Until now there have been very few experimental investigations of localization of high frequency acoustic phonons and a vast majority of the studies explored defect cavities in 1D superlattices. Yet, localization in 2D and 3D crystals exhibits several novel features, such as phonon guiding along linear defects, which are not observable in 1D phononic crystals. Therefore, experimental investigation of phonon localization in 2D and 3D hypersonic crystals is a very promising direction for further advancement of phononics.

Finally, it is important to explore potential applications of hypersonic phononic crystals, many of which have been discussed in the first chapter of this thesis. Two areas seem to be particularly promising – creating acousto-optical devices using simultaneous

photonic/phononic band gap materials; and improving the efficiency of thermoelectric materials by engineering the phononic density of states in periodic nanostructures.

The main advantage of simultaneous photonic/phononic band gap materials lies in their ability to localize both photons and phonons in the same spatial region thereby dramatically increasing the intensity of acousto-optical interactions. Such materials exhibit strongly nonlinear optical and acoustic properties and can be used in many exciting applications, such as optical frequency conversion devices, optical cooling and generation of coherent phonon beams. At the same time, fabrication of these structures is not straightforward and requires selecting constitutive materials with desirable mechanical (significant densities and sound velocities contrast), optical (large refractive index contrast, low absorption) and acousto-optical (high acousto-optical coefficients) properties. Moreover, the structural symmetry must allow the formation of simultaneous photonic and phononic gaps for the same volume fraction of constitutive materials. These challenges need to be addressed in future investigations.

The efficiency of thermoelectric energy conversion is proportional to electrical conductivity and inversely proportional to heat conductivity of a thermoelectric material. Unfortunately, in traditional thermoelectric materials, electrical and heat conductivities are linked to each other, such that it is impossible to change one without modifying the other. In contrast, phononic crystals may be able to reduce thermal conductivity by blocking propagation of the dominant thermal phonons without any significant alteration of electrical conductivity. However, the lattice constant of the crystal must be on the

order of the dominant thermal phonons wavelength at a given temperature, which for room temperature operation is at a periodicity of about 1-10 nm. As a result, one needs to reduce the lattice constant of an IL defined phononic crystals by two orders of magnitude in order to start influencing thermal properties of materials. This can be potentially done using e-beam lithography, self-assembly or other nanofabrication techniques. Alternatively, it is interesting to explore applications of phononic crystals as low temperature thermoelectric materials. In this case the wavelength of dominant thermal phonons is much larger and there is no need for such dramatic reduction in the lattice constant.

BIBLIOGRAPHY

1. T. Gorishnyy, M. Maldovan, C. K. Ullal, E. L. Thomas, "Sound ideas", *Phys. World*, **18**, 24, 2005.
2. G. Chen, A. Narayanaswamy, C. Dames, "Engineering nanoscale phonon and photon transport for direct energy conversion", *Superlattices and Microstructures*, **35**, 161, 2004
3. R. Venkatasubramanian, E. Siivola, T. Colpitts, B. O'Quinn, "Thin-film thermoelectric devices with high room-temperature figures of merit", *Nature*, **413**, 597, 2001
4. M. Maldovan, E. L. Thomas, "Diamond-structured photonic crystals", *Nature Materials*, **3**, 593, 2004
5. L. Brillouin, "Wave propagation in periodic structures", New York: McGraw-Hill, 1946
6. V. K. Kinra, E. L. Ker, "An experimental investigation of pass bands and stop bands in 2 periodic particulate composites", *Int. J. of Solids and Structures*, **19**, 393, 1983
7. E. H. Lee, W. H. Yang, "Waves in composite-materials with periodic structure", *SIAM J. Appl. Math.*, **25**, 492, 1973
8. J. P. Dowling, "Sonic band-structure in fluids with periodic density variations", *J. Acous. Soc. America*, **91**, 2539, 1992
9. M. M. Sigalas, E. N. Economou, "Elastic and acoustic-wave band-structure", *J. Sound and Vibration*, **158**, 377, 1992
10. M. M. Sigalas, E. N. Economou, "Band-structure of elastic waves in 2-dimensional systems", *Solid State Commun.* **86**, 141, 1993
11. M. S. Kushwaha, P. Halevi, L. Dobrzynski, B. Djafari-Rouhani, "Acoustic band-structure of periodic elastic composites", *Phys. Rev. Lett.*, **71**, 2022, 1993
12. M. Kafesaki, M. M. Sigalas, E. N. Economou, "Elastic-wave band-gaps in 3-D periodic polymer matrix composites", *Solid State Comm.*, **96**, 285, 1995
13. M. Kafesaki, E. N. Economou, "Multiple-scattering theory for three-dimensional periodic acoustic composites", *Phys. Rev. B*, **60**, 11993, 1999

14. C. Goffaux, J. Sanchez-Dehesa, "Two-dimensional phononic crystals studied using a variational method: Application to lattices of locally resonant materials", *Phys. Rev. B*, **67**, 144301, 2003
15. M. S. Kushwaha, B. Djafari-Rouhani, "Complete acoustic stop bands for cubic arrays of spherical liquid balloons", *J. Appl. Phys.*, **80**, 3191, 1996
16. M. S. Kushwaha, B. Djafari-Rouhani, "Giant sonic stop bands in two-dimensional periodic system of fluids", *J. Appl. Phys.*, **84**, 4677, 1998
17. Caballero, J. Sanchez-Dehesa, C. Rubio, R. Martinez-Sala, J. V. Sanchez-Perez, F. Meseguer, J. Llinares, "Large two-dimensional sonic band gaps", *Phys. Rev. E*, **60**, R6316, 1999
18. J. O. Vasseur, B. Djafari-Rouhani, L. Dobrzynski, P. A. Deymier, "Acoustic band gaps in fibre composite materials of boron nitride structure", *J. Phys. Condens. Matter*, **9**, 7327, 1997
19. Y. Lai, X. Zhang, Z.-Q. Zhang, "sonic band gaps in 12-fold quasicrystals", *J. Appl. Phys.*, **91**, 6191, 2002
20. Y. Lai, X. Zhang, Z.-Q. Zhang, "Engineering acoustic band gaps", *Appl. Phys. Lett.*, **79**, 3224, 2001
21. O. Sigmund, J. S. Jensen, "Systematic design of phononic band-gap materials and structures by topology optimization", *Phil. Trans. R. Soc. Lond. A*, **361**, 1001, 2003
22. R. Martinez-Sala, J. Sancho, J. V. Sanchez, V. Gomez, J. Llinares, "Sound attenuation by sculpture", *Nature*, **378**, 6554, 1995
23. Z. Liu, X. Zhang, Y. Mao, Y. Y. Zhu, Z. Yang, C. T. Chan, P. Sheng, "Locally resonant sonic materials", *Science*, **289**, 1734, 2000
24. J. B. Pendry, "Negative refraction makes a perfect lens", *Phys. Rev. Lett.*, **85**, 3966, 2000
25. C. Luo, S. G. Johnson, J. D. Joannopoulos, "All-angle negative refraction in a three-dimensionally periodic photonic crystal", *Appl. Phys. Lett.*, **81**, 2352, 2002
26. A. Berrier, M. Mulot, M. Swillo, M. Qiu, L. Thylen, A. Talneau, and S. Anand, "Negative refraction at infrared wavelengths in a two-dimensional photonic crystal," *Phys. Rev. Lett.*, **93**, 073902, 2004

27. X. Zhang, Z. Liu, "Negative refraction of acoustic waves in two-dimensional phononic crystals", *Appl. Phys. Lett.*, **85**, 341, 2004
28. S. Yang, J. H. Page, Z. Liu, M. L. Cowan, C. T. Chan, P. Sheng, "Focusing of sound in a 3D phononic crystal", *Phys. Rev. Lett.*, **93**, 024301, 2004
29. A. Håkansson, F. Cervera, J. Sánchez-Dehesaa, "Sound focusing by flat acoustic lenses without negative refraction", *Appl. Phys. Lett.*, **86**, 054102, 2005
30. X. Hu, Y. Shen, X. Liu, R. Fu, J. Zi, "Superlensing effect in liquid surface waves", *Phys. Rev. E*, **69**, 030201, 2004
31. M. Maldovan, E. L. Thomas, "Simultaneous complete elastic and electromagnetic band gaps in periodic structures", *Appl. Phys. B*, **83**, 595, 2006
32. M. Maldovan, E. L. Thomas, "Simultaneous localization of photons and phonons in two-dimensional periodic structures", *Appl. Phys. Lett.*, **88**, 251907, 2006
33. M. Trigo, A. Bruchhausen, A. Fainstein, B. Jusserand, V. Thierry-Mieg, "Confinement of acoustical vibrations in a semiconductor planar phonon cavity", *Phys. Rev. Lett.*, **89**, 227402, 2002
34. P. A. Fokker, J. I. Dijkhuis, H. W. de Wijn, "Stimulated emission of phonons in an acoustical cavity", *Phys. Rev. B*, **55**, 2925, 1997
35. A. Urbas, "Block copolymer photonic crystals", Ph.D. Thesis, Massachusetts Institute of Technology, 2003
36. K. J. Ahn, F. Milde, A. Knorr, "Phonon-wave-induced resonance fluorescence in semiconductor nanostructures: Acoustoluminescence in the terahertz range", *Phys. Rev. Lett.*, **98**, 027401, 2007
37. S. G. Cloutier, C. H. Hsu, P. A. Kossyrev, J. Xu, "Enhancement of radiative recombination in silicon via phonon localization and selection-rule breaking", *Adv. Mat.*, **18**, 841, 2006
38. L. D. Landau, E. M. Lifshitz, "Theory of elasticity", New York: Pergamon Press, 1986
39. C. C. Mey, "Wave propagation", Lecture notes, MIT, 2004
40. L. D. Landau, and E. M. Lifshitz, "Electrodynamics of continuous media", Pergamon Press, New York, 1984

41. J. K. Krüger, "Brillouin spectroscopy and its application to polymers", in "Optical techniques to characterize polymer systems", *Studies in Polymer Science*, vol. 5, H. Bässler, ed., Elsevier Science, 429, 1989
42. J. R. Sandercock, "Trends in Brillouin-scattering – studies of opaque materials, supported films, and central modes", *Topics in Applied Physics*, **51**, 173, Springer Verlag, 1982
43. S. M. Lindsay, M. W. Anderson, J. R. Sandercock, "Construction and alignment of a high-performance multipass Vernier tandem Fabry-Perot interferometer", *Rev. Sci. Instrum.*, **52**, 1478, 1981
44. J. R. Sandercock, "Tandem Fabry-Perot interferometer TFP-1 operator manual", JRS Scientific Instruments, 2001
45. J.-H. Jang, C. K. Ullal, M. Maldovan, T. Gorishnyy, S. Kooi, C. Y. Koh, E. L. Thomas, "Three dimensional micro and nanostructures via interference lithography", *Adv. Func. Mat.*, in press, 2007
46. M. Campbell, D. N. Sharp, M. T. Harrison, R. G. Denning, A. J. Turberfield, "Fabrication of photonic crystals for the visible spectrum by holographic lithography", *Nature*, **404**, 53, 2000
47. J. H. Moon, S. Yang, "Creating three-dimensional polymeric microstructures by multi-beam interference lithography", *J. Macromol. Sci.-Polym. Rev*, C45, 351, 2005
48. J. H. Moon, J. Ford, S. Yang, "Fabricating three-dimensional polymeric photonic structures by multi-beam interference lithography", *Polym. Adv. Technol.*, **17**, 83, 2006
49. A. J. Turberfield, "Photonic crystals made by holographic lithography", *MRS Bulletin*, **26**, 632, 2001
50. C. K. Ullal, M. Maldovan, M. Wohlgemuth, E. L. Thomas, "Triply periodic bicontinuous structures through interference lithography: a level-set approach", *J. Opt. Soc. Am. A Opt. Image Sci. Vis.*, **20**, 948, 2003
51. M. Maldovan, C. K. Ullal, W. C. Carter, E. L. Thomas, "Exploring for 3D photonic bandgap structures in the 11 f.c.c. space groups", *Nature Mater.*, **2**, 664, 2003

52. H. Lorenz, M. Despont, N. Fahrni, J. Brugger, P. Vettiger, P. Renaud, "High-aspect-ratio, ultrathick, negative-tone near-UV photoresist and its applications for MEMS", *Sens. Actuator A-Phys.*, **64**, 33, 1998
53. K. Y. Lee, N. LaBianca, S. A. Rishton, S. Zolgharnain, J. D. Gelorme, J. Shaw, T. H. P. Chang, "Micromachining applications of a high resolution ultrathick photoresist", *J. Vac. Sci. Technol. B*, **13**, 3012, 1995
54. G. Hong, A. S. Holmes, M. E. Heaton, "SU8 resist plasma etching and its optimisation", *Microsyst. Technol.*, **10**, 357, 2004
55. M. Chatzichristidi, I. Raptis, P. Argitis, J. Everett, "Partially hydrogenated poly(vinyl phenol) based photoresist for near UV, high aspect ratio micromachining", *J. Vac. Sci. Technol. B*, **20**, 2968, 2002
56. L. F. Thompson, C. G. Willson, M. J. Bowden, "Resist processing", *ACS Symposium Series*, **219**, American Chemical Society, Washington, DC, 10, 1983
57. W. Cheng, T. Gorishnyy, V. Krikorian, G. Fytas, E. L. Thomas, "In-plane elastic excitations in 1D polymeric photonic structures", *Macromolecules*, **39**, 9614, 2006
58. M. F. Weber, C. A. Stover, L. R. Gilbert, T. J. Nevitt, A. J. Ouderkirk, "Giant birefringent optics in multilayer polymer mirrors", *Science*, **287**, 2451, 2000
59. F. D'Orazio, G. Gubbiotti, F. Lucari, E. J. Tassoni, "Magnetic and structural properties of Fe/Al multilayers", *J. Magn. Magn. Mater.*, **242**, 535, 2002
60. L. Giovannini, O. Donzelli, J. M. V. Ngaboyisonga, F. Nizzoli, G. Carlotti, G. Gubbiotti, G. Socino, L. Pareti, G. J. Turilli, "Light scattering characterization of metallic single films and multilayers", *J. Magn. Magn. Mater.*, **199**, 366, 1999
61. J. A. Forrest, A. C. Rowat, K. Kalnoki-Veress, J. R. Stevens, J. R. Dutcher, "Brillouin light scattering studies of the mechanical properties of polystyrene/polyisoprene multilayered thin films", *J. Polym. Sci., Part B: Polym. Phys.*, **34**, 3009, 1996
62. G. W. Farnell, E. L. Adler, in *Physical Acoustics, Principles and Methods*, W. P. Mason, R. N. Thurston, Eds.; Academic Press: New York, 1972; Vol. 9.
63. J. Kerns, A. Hsieh, A. Hiltner, E. Baer, "Comparison of irreversible deformation and yielding in microlayers of polycarbonate with poly(methylmethacrylate) and poly(styrene-co-acrylonitrile)", *J. App. Pol. Sci.*, **77**, 1545, 2000

64. J. Kerns, A. Hsieh, A. Hiltner, E. Baer, "Mechanical behavior of polymer microlayers", *Macromolecular Symposia*, **147**, 15, 1999
65. T. Gorishnyy, C. K. Ullal, M. Maldovan, G. Fytas, E. L. Thomas, "Hypersonic phononic crystals", *Phys. Rev. Lett.*, **94**, 115501, 2005
66. O. K. Chan, F. C. Chen, C. L. Choy, I. M. Ward, "Elastic-constants of extruded polypropylene terephthalate", *J. Phys. D: Appl. Phys.*, **11**, 617, 1978
67. R. Feng, R. J. Farris, "Linear thermoelastic characterization of anisotropic poly(ethylene terephthalate) films", *J. Appl. Polym. Sci.*, **86**, 2937, 2002
68. S. H. Anders, R. Eberle, L. Peetz, J. K. Krüger, U. Göschel, M. Pietralla, "Anisotropic properties of poly(ethylene terephthalate) by Brillouin spectroscopy: Anisotropic properties of oriented bulk and nanostructured poly(ethylene terephthalate) determined by Brillouin spectroscopy and birefringence experiments", *J. Polym. Sci., Part B: Polym. Phys.*, **40**, 1201, 2002
69. W. Cheng, G. Fytas, A. V. Kiyanova, M. Efremov, P. F. Nealey, "Submicron polymer gratings: Optical diffraction and spontaneous Brillouin scattering", *Macromol. Rapid Commun.*, **27**, 702, 2006
70. W. Cheng, T. Gorishnyy, N. Gomopoulos, J. Walish, A. Hiltner, E. Baer, G. Fytas, E. L. Thomas, "Probing the acoustics of periodic soft nanolayers", *submitted to Phys. Rev. Lett.*
71. A. Urbas, E. L. Thomas, H. Kriegs, G. Fytas, R. Penciu, E. N. Economou, "Acoustic excitations in a self-assembled block copolymer photonic crystal", *Phys. Rev. Lett.*, **90**, 108302, 2003
72. Z. Hou, X. Fu, Y. Liu, "Singularity of the Bloch theorem in the fluid/solid phononic crystal", *Phys. Rev. B*, **73**, 024304, 2006
73. Y. Tanaka, Y. Tomoyasu, S.-I. Tamura, "Band structure of acoustic waves in phononic lattices: Two-dimensional composites with large acoustic mismatch", *Phys. Rev. B*, **62**, 7387, 2002
74. C. Goffaux, J. P. Vigneron, "Theoretical study of a tunable phononic band gap system", *Phys. Rev. B*, **64**, 075118, 2001

75. C. Mias, J. P. Webb, R. L. Ferrari, "Finite element modelling of electromagnetic waves in doubly and triply periodic structures", *IEE Proc.-Optoelectron.*, **146**, 111, 1999
76. S. Guenneau, A. B. Movchan, "Analysis of elastic band structures for oblique incidence", *Arch. Ration. Mech. Anal.*, **171**, 129, 2004
77. W. Cheng, J. Wang, U. Jonas, G. Fytas, N. Stefanou, "Observation and tuning of hypersonic bandgaps in colloidal crystals", *Nature Mat.*, **5**, 830, 2006
78. J.-H. Jang, C. K. Ullal, T. Gorishnyy, V. V. Tsukruk, E. L. Thomas, "Mechanically tunable three-dimensional elastomeric network/air structures via interference lithography", *Nanoletters*, **6**, 740, 2006
79. Y. Xia, G. M. Whitesides, "Soft lithography", *Angew. Chem., Int. Ed.*, **37**, 550 1998
80. D. T. Chiu, N. L. Jeon, S. Huang, R. S. Kene, C. J. Wargo, I. S. Choi, D. E. Ingber, G. M. Whitesides, "Patterned deposition of cells and proteins onto surfaces by using three-dimensional microfluidic systems", *Proc. Natl. Acad. Sci. U.S.A.*, **97**, 2408, 2000
81. J. C. McDonald, G. M. Whitesides, "Poly(dimethylsiloxane) as a material for fabricating microfluidic devices", *Acc. Chem. Res.*, **35**, 491, 2002
82. K. M. Choi, J. A. Rogers, "A photocurable poly(dimethylsiloxane) chemistry designed for soft lithographic molding and printing in the nanometer regime", *J. Am. Chem. Soc.*, **125**, 4060, 2003
83. K. S. Ryu, X. Wang, K. Shaikh, C. Liu, "A method for precision patterning of silicone elastomer and its applications", *IEEE, J. Microelectromech. Syst.*, **13**, 568, 2004
84. W.-Y. Chiang, W.-J. Shu, "Preparation and properties of UV-curable poly(dimethylsiloxane) urethane acrylate .2. property-structure molecular-weight relationships", *J. Appl. Polym. Sci.*, **36**, 1889, 1988
85. J. A. Rogers, O. J. A. Schueller, C. Marzolin, G. M. Whitesides, "Wave-front engineering by use of transparent elastomeric optical elements", *Appl. Opt.*, **36**, 5792, 1997
86. J. L. Wilbur, R. J. Jackman, G. M. Whitesides, E. L. Cheung, L. K. Lee, M. G. Prentiss, "Elastomeric optics", *Chem. Mater.*, **8**, 1380, 1996

87. T. Tanaka, M. Morigami, N. Atoda, "Mechanism of resist pattern collapse", *J. Electrochem. Soc.*, **140**, L115, 1993
88. E. Delamarche, H. Schmid, H. A. Biebuyck, B. Michel, "Stability of molded polydimethylsiloxane microstructures", *Adv. Mater.*, **9**, 741, 1997
89. T. W. Lee, O. Mitrofanov, L. W. P. Hsu, "Pattern-transfer fidelity in soft lithography: The role of pattern density and aspect ratio", *Adv. Funct. Mater.*, **15**, 1683, 2005
90. W. Deforest, *Photoresist: Materials and Processes*; McGraw-Hill Book Co., Inc.: New York, p 132, 1975
91. *Introduction to Microlithography*; L. F. Thompson, C. G. Willson, M. J. Bowden, Eds.; ACS Symposium Series, No. 219; American Chemical Society: Washington, DC, p 139, 1994
92. D. L. Goldfarb, J. J. de Pablo, P. F. Nealey, J. P. Simons, W. M. Moreau, M. Angelopoulos, "Aqueous-based photoresist drying using supercritical carbon dioxide to prevent pattern collapse", *J. Vac. Sci. Technol. B*, **18**, 3313, 2000
93. O. Raccurt, F. Tardif, F. Arnaud d'Avitaya, T. Vareine, "Influence of liquid surface tension on stiction of SOI MEMS", *J. Micromech. Microeng.*, **14**, 1083, 2004